

NORWEGIAN UNIVERSITY OF LIFE SCIENCES





## **Preface and Acknowledgement**

This master thesis is written as part of a master degree in Environment and Natural Resources (Miljø- og naturressurser) at Norwegian University of Life Sciences (UMB). It is part of the SoilCAM project (Soil Contamination; Advanced integrated characterisation and time-lapse Monitoring, [www.soilcam.eu](http://www.soilcam.eu)) financed by the European Commission's 7th Framework Programme, Grant Agreement 212663.

My supervisors contributing to completing this thesis are Helen French (UMB) and Esther Bloem (Bioforsk). Many thanks for helpful advice and guidance throughout this project! Their effort and time is greatly appreciated.

I would also like to thank everyone who has been helping out at Moreppen during field work, and following laboratory work. Thanks to Kyle Elkin for his support to the field work. Further, I would like to thank Robert Barneveld, Andrew Binley, Gro Eggen and Nicolas Forquet for their kind contributions.

Thanks go to my fellow students for creating a rewarding and social environment to study in. Also thanks to friends and family!

Astri Søyland, 13.05.2010

Department of Plant and Environmental Sciences

Norwegian University of Life Sciences (UMB)

30 credits



## Abstract

This master thesis focuses on the use of cross-borehole electrical resistivity tomography (ERT) surveys as a monitoring method of the infiltration of snowmelt containing de-icing chemicals. Oslo Airport Gardermoen (OSL) is located on Norway's largest rain fed aquifer. The winter conditions require the use of de-icing chemicals (propylene glycol, PG, and potassium formate, KFo) due to safe air traffic. The groundwater is protected by law against contamination and as the de-icing chemicals are spread to the side of the runways, OSL is dependent on the transport rate and degradation capacity of the unsaturated zone. ERT is currently being tested in field as a monitoring method for the infiltration of de-icing chemicals and their degradation in the unsaturated zone.

A tracer experiment was carried out at Moreppen which is a research station located outside the area of OSL. PG and KFo were applied on the snow cover prior to the snowmelt in 2010 at two separate walls (north and south wall) of a lysimeter trench together with an inactive tracer ( $\text{Br}^-$ ). The infiltration of chemicals and snowmelt at these two walls were monitored by cross-borehole ERT. Time-lapse inversions showing the difference in resistivity between the time of interest and a background dataset were compared, and the south wall infiltration monitored by the ERT was compared to extraction of soil water by the use of suction cups (Prenart Super Quartz) installed in the soil profile. Looking at time-lapse inversions, infiltration of melt water and conductive chemicals is clearly seen. The north wall showed greater depth of infiltration with higher reduction in resistivity compared to the south wall. This can be due to coarse layers of sediment at different depth in the two profiles slowing down the infiltration. PG applied to the south wall is not conductive and KFo is, explaining differences in reduction of resistivity. The infiltration depth suggested by the suction cups was shallower than shown by the ERT for the south wall indicating that either infiltrating water was transported deeper than  $\text{Br}^-$  or that old water was pushed deeper by piston flow. Time-lapse inversions are shown here to be a good qualitative method to monitor infiltration of water and conductive chemicals at a scale of a few meters, such as in field experiments.

Individual inversions for the south and north wall of the separate datasets were temperature corrected. Electrical resistivity is temperature dependent and to be able to view changes due to solute and water content needs to be removed. ERT gives mainly qualitative inversion results and to obtain quantitative information in form of water content and saturation the inversions for the south wall were converted using petro-physical relationships and fitting parameters from soil at Moreppen. Yeh et al. (2002)'s formula for water content gave values within the expected range when comparing the values to previous water content measurements. Saturation calculated from Archie's law seems to be limited by the uncertainty of estimated porosity as the porosity is likely changing through the profile and might give better results when looking at change in saturation when porosity can be assumed fixed. As translating ERT inversions to water content using the fitting parameters for the Moreppen soil has been shown here to be within a realistic range, the conversion has the potential to calculate the solute resistivity and change in solute over time if water content is known. Combining ERT with a method to measure water content (e.g. TDR) would allow the inversions, using these

formulas, to be converted to solute which is of interest when monitoring contamination in the subsurface. Joint inversions with cross-borehole ground-penetrating radar (GPR) surveys will provide superior inversions.

# Contents

<b>List of figures</b> .....	i
<b>List of tables</b> .....	iii
<b>1. Introduction</b> .....	1
1.1 SoilCAM.....	2
1.2 Objectives .....	2
<b>2. Area description</b> .....	4
2.1 Oslo Airport Gardermoen (OSL).....	4
2.1.1 Geology and hydrogeology of the area .....	5
2.1.2 Climate.....	6
2.2 The research station Moreppen at OSL .....	6
2.3 De-icing chemicals .....	7
2.3.1: Propyleneglycol (PG) .....	7
2.3.2 Potassium Formate (KFo).....	8
2.3.3 The environmental risk of de-icing chemicals.....	9
2.3.4 Discharge permit for de-icing chemicals .....	10
<b>3. Theory</b> .....	11
3.1 Flow in the unsaturated zone .....	11
3.1.1 Basic soil theory.....	11
3.1.2 Movement of water in the unsaturated zone .....	11
3.1.3 Infiltration .....	13
3.1.4 Movement of solutes.....	13
3.2 The resistivity method .....	14
3.2.1 The basic principle of the resistivity method.....	14
3.2.2 Cross-borehole ERT surveys .....	17
3.2.3 Modelling and data inversion.....	18
3.2.4 Temperature correction.....	20
3.2.5 Time-lapse resistivity modelling.....	21
3.2.6 Interpretation of resistivity data .....	21
<b>4. Method</b> .....	23
4.1 Field work at Moreppen and field setup.....	23
4.1.1 Cross-borehole resistivity data gathering.....	24
4.1.2 Pore water EC data from suction cups.....	25

4.1.3 Air and soil temperature data .....	27
4.1.4 TDR measurements.....	28
4.1.5 Groundwater level.....	28
4.1.6 Cumulative snowmelt .....	28
4.2 Resistivity data processing .....	29
4.2.1 Individual inversion models.....	30
4.2.2 Time-lapse models .....	31
4.2.3 Temperature correction.....	32
4.2.4 Saturation and water content images .....	33
<b>5. Results and Discussion .....</b>	<b>35</b>
5.1 Groundwater level and snowmelt infiltration.....	35
5.2 Soil and Air Temperature .....	37
5.3 Interpretation of resistivity data.....	39
5.3.1 Sensitivity plots of the ERT measurements .....	39
5.3.2 Comparing ERT measurements to lithology.....	41
5.3.3 Temperature correction.....	44
5.3.4 ERT ratio.....	46
5.3.5 Infiltration patterns seen from ERT inversions.....	48
5.3.5.1 Comparing south wall and north wall time-lapse inversions.....	53
5.3.5.2 Comparing ERT time-lapse inversions with pore water EC measurements.....	56
5.3.6 Quantitative interpretation of the ERT measurements for the south wall .....	57
5.3.7 Change in saturation images .....	62
<b>6. Conclusion.....</b>	<b>64</b>
<b>7. Future work .....</b>	<b>66</b>
<b>8. References .....</b>	<b>69</b>
<b>9. Appendix .....</b>	<b>73</b>



## List of figures

<b>Figure 1:</b> A) Quaternary geological map showing the subsurface properties of the Gardermoen delta (Tuttle 1997, modified by Aagaard and Breedveld 2008). Location of Gardermoen airport (OSL) and Moreppen are marked on the map. B) Map of Norway showing location of Oslo and the Gardermoen aquifer (Kitterød 2008).....	5
<b>Figure 2:</b> Picture of sediments within the OSL area illustrating the heterogeneity in the sedimentary structures in the area. (Picture taken by French, printed with permission) .....	6
<b>Figure 3:</b> Sketch of the simple definition of resistivity across a homogeneous block of side length (L) with an applied current (I) and a potential drop between opposite faces (V). (Adapted from Reynolds (1997)). .....	15
<b>Figure 4:</b> Current and equipotential lines produced by a pair of current electrodes (A and B) and the drop in voltage measured by the pair of potential electrodes (M and N) in homogeneous earth with Wenner configuration (Bloem 2002). .....	17
<b>Figure 5:</b> Sketch showing the locations of the ERT boreholes compared to the lysimeter trench, the GPR boreholes and the suction cups where the length indicated is the length of the suction cups furthest from the trench wall (Elkin 2011). The boreholes at the west wall are not shown. ....	23
<b>Figure 6:</b> Syscal Pro Switch (Geo 2011) .....	25
<b>Figure 7:</b> Diagram showing the distribution of suction cups in the south (a) and north (b) walls of the lysimeter trench at Moreppen. One number represents one suction cup in the soil profile. The X and Y coordinates for the location of suction cups in the south wall are given in appendix 1 (French 1999). ....	26
<b>Figure 8:</b> A) Picture inside the lysimeter trench (French 1999). B) Sketch showing the principle behind the suction cups extracting water at the lysimeter trench at Moreppen. Suction is created by the vacuum pump in the Prenart soil water sampler (location of the samples shown in figure 7 and water is extracted from the soil profile and collected in the Prenart collecting bottle. ....	27
<b>Figure 9:</b> Graph showing the calculated cumulative snowmelt from Moreppen and the measured daily averages groundwater level at Moreppen during the time of interest 2010....	36
<b>Figure 10:</b> Graph showing the measured hourly groundwater depth at Moreppen during 2008, 2009 and most of 2010. Some data is missing. The two red lines indicate the snowmelt period 2010 in focus here. ....	36
<b>Figure 11:</b> Graph showing the average daily soil temperature with depth measured at Moreppen for some chosen dates during the snowmelt period in 2010, as well as 6 <sup>th</sup> of October 2010. ....	38
<b>Figure 12:</b> Graph showing the average change in measured soil temperature at Moreppen during the snowmelt period in 2010. Average has been calculated for measurements done at all depth from 0.05 to 2.4 m, where the red line is daily averages and the blue line is hourly averages. ....	38
<b>Figure 13:</b> Graph showing the measured hourly and daily average air temperature and hourly measured soil temperature at 10 cm depth at Moreppen in the period 13 <sup>th</sup> of March to 21 <sup>st</sup> of May.....	39

<b>Figure 14:</b> Images showing the sensitivity maps for the soil profile between the boreholes for a) the south wall and b) the north wall for the ERT time lapse inversions for the dataset 26 <sup>th</sup> of March 2010 where 22 <sup>nd</sup> of March was used as background dataset. The scale is in log sensitivity. ....	40
<b>Figure 15:</b> Sensitivity maps of individual inversions for the soil profile between the boreholes for a) 22 <sup>nd</sup> of March 2010 south wall b) 22 <sup>nd</sup> of March 2010 north wall c) 6 <sup>th</sup> of October 2010 south wall and d) 6 <sup>th</sup> October 2010 north wall. The scale is in log sensitivity.....	41
<b>Figure 16:</b> Sketch of the sedimentary layers at Moreppen from the lysimeter trench walls (walls folded out) (French 1999).....	42
<b>Figure 17:</b> Image showing the a) grain size distribution of soil sample K-20 modified from Pedersen (1994) and b) section from sketch in figure 16 compared to the ERT images from the south wall of the lysimeter trench on the c) 6 <sup>th</sup> of October 2010 and d) 22 <sup>nd</sup> of March 2010 where the images are the soil profile between the boreholes. In the grain size scale, F= fine, M= medium, C= coarse sand and gravel. After this follows cobble. Location of soil sample is seen in the map in appendix II. Measured groundwater level is indicated on the ERT inversions. ....	42
<b>Figure 18:</b> Image showing the a) grain size distribution of soil sample K-20 modified from Pedersen (1994) and b) section from sketch in figure 16 compared to the ERT images from the north wall of the lysimeter trench on the c) 6 <sup>th</sup> of October 2010 and d) 22 <sup>nd</sup> of March 2010 where the images are the soil profile between the boreholes. In the grain size scale, F= fine, M= medium, C= coarse sand and gravel. After this follows cobble. Location of soil sample is seen in the map in appendix II. Measured groundwater level is indicated on the ERT inversions. ....	43
<b>Figure 19:</b> Images illustrating the temperature correction applied to the ERT inversions. Each image shows the profile between the two boreholes where a) is the standard inversion profile from 29 <sup>th</sup> of March 2010 b) is the temperature corrected inversion profile from 29 <sup>th</sup> of March 2010 and c) is the suction cup data automatically temperature corrected from 29 <sup>th</sup> of March d) is the raw ERT dataset from 21 <sup>st</sup> of May 2010 e) is the temperature corrected dataset from 21 <sup>st</sup> of May 2010 and f) is the suction cup data automatically temperature corrected from 21 <sup>st</sup> of May 2010. The images c) and f) are in the log scale 2 to 3. ....	45
<b>Figure 20:</b> Graph showing the progression of ERT ratio for the south and north wall, together with cumulative snowmelt at Moreppen. 26 <sup>th</sup> of March 2010 is used as background date, both for cumulative snowmelt and ERT ratios.....	46
<b>Figure 21:</b> Graph showing change in average ERT measurements (bulk resistivity) and change in suction cup measurements (pore water resistivity). The background dataset used is 29 <sup>th</sup> of March 2010. ....	48
<b>Figure 22:</b> Images of time-lapse inversions for a) the south wall and b) the north wall. The background dataset is the 22 <sup>nd</sup> of March, prior to tracer applications. C) is the pore water resistivity interpolated from suction cups from the south wall. The images illustrate the soil profile between the boreholes. The pore water resistivity images have a square indicating the region containing 37 of the 38 suction cups.....	53
<b>Figure 23:</b> Images illustrating the interpretation of the ERT inversions for the 29th of March 2010 where a) is the ERT inversion in log resistivity scale b) is estimated saturation from 0 to 1 and c) is the water content in percentage. ....	57

**Figure 24:** Graph showing a) the estimated water content (%) using Yeh et al. (2002)'s formula (equation 39) b) estimated water content from Archie's law (equation 40), where both a and b are calculated from ERT and pore water EC data with depth (m) of soil profile between boreholes for the snowmelt period 2010. Average pixel values are calculated for intervals of 0.5 m. c) is the measured moisture content by Langsholt et al. (1996) using a neutron moisture probe at Moreppen during the snowmelt period 1994. The location of the neutron moisture probe (N12) can see seen on the map in appendix II. .... 59

**Figure 25:** Graph showing calculated cumulative snowmelt (mm), change in saturation and water content estimated from ERT data and pore water EC for the soil profile between the boreholes (0-5 m depth) and change in water content measured by TDR at 30 cm for the south wall. Cumulative snowmelt has start date 26<sup>th</sup> of March 2010 and the changes are compared to 29<sup>th</sup> of March 2010. .... 61

**Figure 26:** Graph showing change in water content measured with TDR at 30 cm, and estimated change in water content using ERT and pore water EC data from pixel values in the depth 30cm. Changes are compared to 29<sup>th</sup> of March 2010 as background. .... 62

**Figure 27:** Images showing calculated change in saturation in the soil profile between the boreholes. It is calculated using 22<sup>nd</sup> of March 2010 as background ERT and 17<sup>th</sup> of September 2010 as background for pore water conductivity. Dates are given above figure. The scale is change hence green implies no change, blue is decrease and red is increase in saturation. Notice the inverse colours compared to figure 22. .... 63

**List of tables**

**Table 1:** Specifications for boreholes..... 24



## 1. Introduction

Oslo Airport Gardermoen AS (OSL) is Norway's main airport and was opened in 1998. It is located 47 km north of Oslo and covers 1/10 of the Gardermoen aquifer which is the largest rain fed unconfined aquifer in Norway. Currently the aquifer is not used as drinking water, but is considered a valuable resource due to its potential as a drinking water source in the future. Some areas surrounding the airport are protected by law, such as kettle hole lakes and ravine landscape and this includes the groundwater. The decision to locate OSL at Gardermoen was thus controversial but accepted based on the condition that activities associated with running the airport should not affect the quality or quantity of the groundwater or the surrounding nature. Due to this, OSL is challenged with the balance between running the airport safely and efficiently and at the same time following the strict regulations set up to prevent contamination of the groundwater and surface water (OSL 1999; Øvstedal & Wejden 2007; French et al. 2009a).

The greatest risk of polluting the groundwater in the Gardermoen aquifer is the use of de-icing chemicals during the winter at OSL. The use of de-icing chemicals is vital to ensure safe air-traffic during the cold winter season. Although these chemicals are organic molecules that easily degrade in the highly permeable subsurface, the threat to the groundwater is the potential of overloading the soil system, especially during snowmelt. This can be a period where velocities in the unsaturated zone far exceeds the degradation rate of these chemicals (French et al. 2009a). De-icing chemicals which either drips of airplanes or are mechanically removed with snow from runways are stored in snow packs during winter and infiltrates into the soil together with the first melt water in spring. OSL is therefore dependent on the degradation capacity of the local unsaturated zone by the population of microorganisms to prevent de-icing chemicals from reaching the groundwater. Monitoring of the infiltration of melt water together with de-icing chemicals is therefore of importance.

Methods to monitor the unsaturated zone at OSL are therefore needed. Field experiments are important to clarify aspects of unsaturated flow under natural conditions; some of which cannot be obtained under laboratory experiments. Geophysical methods could be an inexpensive and easy method for this purpose. Direct current (DC) electrical resistivity tomography (referred to here as resistivity or ERT) is a geophysical method which allows for the determination of the spatial distribution of the low-frequency resistive characteristics of the subsurface. This property is affected by lithology, pore fluid chemistry, and water content; and hence this method is used for hydrogeophysical applications, as in this project. The surveys are easy to carry out, inexpensive, data processing tools are widely available, and the relationships between resistivity and hydrological properties are reasonably well established. This has made resistivity methods widely used sets of geophysical techniques (Binley & Kemna 2005).

There are many benefits with using resistivity method. It is a non-invasive method, in contrast to many conventional methods. Resistivity and more generally geophysical methods, provides extensive spatial information of underground structures and soil properties without the need of digging a multitude of boreholes or wells and the method can be carried out on the surface.

However, the challenges with electrical methods are that despite their long history, these methods are still developing. A common constraint is lack of appropriate hardware or software tools for data collection and processing. The speed of data collection is improving, but time still remains a serious restriction for three-dimensional investigations. Many inversion models are based on smoothness constraint and this might not be appropriate in all cases (such as sharp lithological boundaries or at the edge of a contaminant or tracer plume); however, this problem is being worked on. Another challenge is that there is limited quantitative information available to a hydrologist from a resistivity image as the inversions are mainly qualitative (Binley & Kemna 2005). The accuracy of ERT surveys has been under debate because of its non-unique inverse solution and spatial variability of the constitutive relationship between resistivity and moisture content (Liu & Yeh 2004). The method still requires some improvement and testing in field, and this is one of the areas this master thesis and the SoilCAM project is working on.

## **1.1 SoilCAM**

This master thesis is part of a four year project called the SoilCAM project: Soil contamination: advanced integrated characterisation and time-lapse monitoring. The aim of the SoilCAM project is to improve the current methods for monitoring contaminant distribution and biodegradation in the subsurface by testing and optimising invasive and non-invasive methods to use for this purpose in the field. Traditional monitoring of contamination in soil include methods such as lysimeters, soil sampling and monitoring of the groundwater below a contaminated site. These methods neither capture the contaminated distribution nor their removal rates. The unsaturated zone forms a natural barrier for contamination to the groundwater and it is therefore of importance to develop methods to assess this risk of pollution to the groundwater, as well as monitoring this zone. Geophysical methods, such as resistivity, gives the possibility for improved resolution of data in time and space compared to conventional methods but still needs testing in field to be able to quantify the results (French et al. 2009b). OSL is one of two field sites which is used.

## **1.2 Objectives**

Oslo airport Gardermoen (OSL) depends on the unsaturated zone to protect the groundwater from de-icing chemicals used during the winter season. To ensure sufficient control of processes in the unsaturated zone, methods for monitoring infiltration of melt water containing de-icing chemicals and their degradation are needed. Many conventional methods are lacking adequate resolution thus evaluation of degradation progress is flawed by uncertainty. Geophysical methods, such as resistivity, can potentially give the possibility to determine contamination levels and degradation with better spatiotemporal coverage for lower costs than conventional methods (such as soil water sampling). Field testing is still needed to investigate the relationship between geophysical measureable parameters and soil physical and degradation activity parameters.

This master thesis examines the potential of cross-borehole resistivity to interpret flow and transport processes. Data were collected in the north and south wall of a lysimeter trench at Moreppen research station during the snowmelt 2010. As Moreppen is located outside the

airport, it is thought to have the same soil as in the airport area and allows for controlled small-scale experiments. The aim of this thesis is to examine different inversions techniques of resistivity data collected during the snowmelt period 2010, techniques include time-lapse models and individual inversions; where individual inversions present the modelled resistivity data measured in field at a specific date and time-lapse inversions show the change in resistivity between a specific date and a measured background resistivity (e.g before infiltration). The effect of including other datasets such as soil temperature and pore water electrical conductivity (EC) measured in suction cups is also examined. Optimization of the models is based on data error and final data misfit. To remove the effect of changing soil temperature on resistivity, temperature corrections are carried out. Electrical resistivity profiles are compared to images of contaminant plume distribution obtained from suction cup measurements. The hypothesis is that resistivity inversions can provide an alternative method for observing flow and contaminant transport in the unsaturated zone. It is also expected that the resistivity method will capture heterogeneous snow melt and preferential flow through the unsaturated zone, since this was observed in previous studies at Moreppen.

An attempt to translate the individual resistivity inversions to water content and saturation to view the flow of water through the unsaturated zone is carried out by using petro-physical relationships and fitting parameters found for the soil at Moreppen. To validate the conversions, the results will be compared to measurements of water content made at Moreppen. Having the fitting parameters from the Moreppen soil, the hypothesis is that it will be possible to estimate the water content accurately from these conversions. The benefit of this conversion is that, if reliable, the resistivity method can be used to measure the movement of water, and ideally the contamination level, without or only to a limited extent having to carry out other measurements than resistivity.

## 2. Area description

### 2.1 Oslo Airport Gardermoen (OSL)

OSL is located in the southeast of Norway, at a mean elevation of 200 m.a.s.l (Jørgensen & Østmo 1990) (Figure 1). Before the airport was opened in 1998, the area was used for military activities for more than 200 years and also as a military airport. The first plane landed here already in 1912. More recently, the location was used as a charter flight airport (French et al. 2009a). OSL covers today an area of 13 km<sup>3</sup> and yearly handles about 18 million passengers. There are plans to increase the existing airport with another terminal to meet future traffic loads (OSL 2009b) and it is expected that the airport will expand with a third runway in the future (Jartun 2011).

The Romerike area, located northeast of the airport, has since 1985 been protected by law by the Norwegian Ministry of the Environment as Romerike Landscape reserve, due to the ravine landscape with its characteristic ecology. The ravine landscape is a result of the natural erosion processes in the spring horizons due to groundwater flow. The protection also includes the river Vikka (Figure 1 a), which flows east of the airport, as a scientific reference area (Miljøverndepartementet 1985). The quaternary geology and limnology of the area is seen to have international protection value and has since 1999 been protected by law as the Eldstad Landscape reserve by the Norwegian Ministry of the Environment. This includes the kettle hole lakes on the surface of the delta, where some of the lakes communicate with the groundwater while some are separated from the groundwater by an impermeable layer. The purpose of the protection is to conserve the geological elements, such as the kettle hole lakes, kames and eskers, as well as limnological occurrences, in a landscape where zoological, botanical and historic elements contribute to giving this area its distinctive value (Miljøverndepartementet 1999).



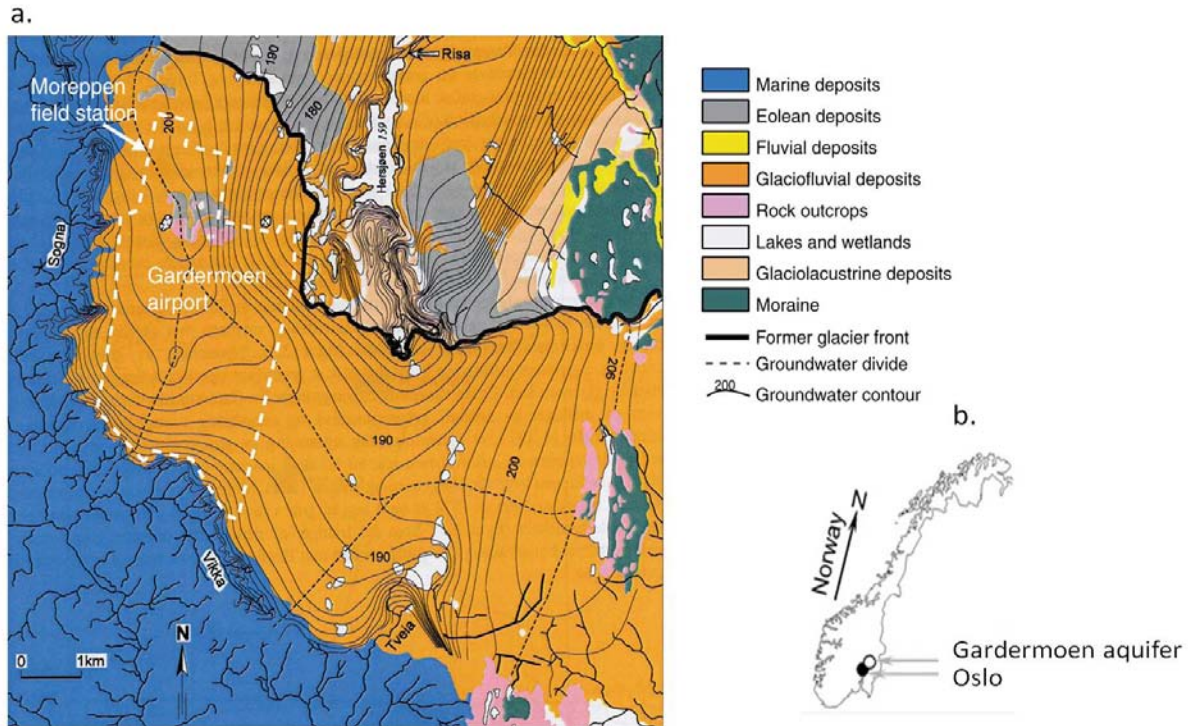


Figure 1: A) Quaternary geological map showing the subsurface properties of the Gardermoen delta (Tuttle 1997, modified by Aagaard and Breedveld 2008). Location of Gardermoen airport (OSL) and Moreppen are marked on the map. B) Map of Norway showing location of Oslo and the Gardermoen aquifer (Kitterød 2008).

### 2.1.1 Geology and hydrogeology of the area

OSL is situated on a ice-contact depositional paleosystem called the Gardermoen Delta (previously called the Hauerseier Delat) (Tuttle et al. 1997). The map of the quaternary geology of the area (Figure 1a) shows formations composed of sand and gravel underlain by silty glacio-marine deposits (Jørgensen & Østmo 1990). This corresponds with the understanding that the delta developed in a marine mud dominated fjord basin (Tuttle 1997). The Gardermoen Delta was formed during the deglaciation of Scandinavia after the Pleistocene period, about 9500 years B.C (Sørensen 1979). It comprises approximately  $8 \text{ km}^3$  of sediments, (Tuttle 1997) and the delta covers today an area of  $79 \text{ km}^2$ . The ice cap reached into a narrow fjord, called the Romerike fjord, were sediment settled out to from the delta during periods of stagnation. There are three subunits of the delta formation where the bottom unit is composed of submarine fine grained material, the fore set unit consists of sandy material deposited in diagonal layers and the top set unit mainly is fluvial gravel and coarse sand deposited in horizontal layers. The fore set unit is more homogeneous than the top set unit and consists of laminas of fine sand that dip with an angle of  $15\text{-}30^\circ$  to the horizontal plane (Pedersen, 1994; Tuttle, 1997; Søvik & Aagard, 2003; Kitterød, 2008). The heterogeneity of sedimentary structures are seen in the area (Figure 2). Podzol profiles have developed on these sandy soils and the area is mainly covered by coniferous forests (French 1999).

The groundwater level varies between 1 to 30 m (French et al. 2009a). The groundwater divide is located under the airport and the flow below the airport is separated in two main directions (Figure 1 a). Most of the water, 70%, flows eastward and feeds the lake Hersjøen and the river Risa. The remaining water flows out of the aquifer as springs in the west

(Erikstad & Halvorsen 1992) (Figure 1 a). The hydraulic conductivities ( $K_s$ ) range in the area from  $10^{-3}$  to  $10^{-5}$  m/s. Due to the flat topography, there is no surface runoff, not even during snowmelt and soil frost. The soil has a very high infiltration capacity, with infiltration rates of 4 – 5 cm/min under saturated conditions (Jørgensen & Østmo 1990). Water flow has been found by French (1999) to have a velocity through the unsaturated zone of 0.2 m/d under unsaturated conditions.



Figure 2: Picture of sediments within the OSL area illustrating the heterogeneity in the sedimentary structures in the area. (Picture taken by French, printed with permission)

### 2.1.2 Climate

The climate in the area is a moderately continental climate. The mean annual precipitation and evapo-transpiration are approximately 800 mm and 400 mm, respectively. About 64% of the precipitation is received as rain, while 31% is snow and the remainder being a mix of snow and rain. The winter months are relatively cold with a constant snow cover for the whole duration of the winter season. More than half of the groundwater recharge occurs during the 3-5 weeks of the snow melting period (Jørgensen & Østmo 1990).

## 2.2 The research station Moreppen at OSL

Moreppen is a research station, built in 1992, in order to investigate and monitor the hydrogeological properties of the Gardermoen delta and to identify risks of groundwater contaminations. It is located 800 m northwest of OSL, (figure 1 a). The elevation is 205 m.a.s.l. and the topography is flat (Pedersen 1994). It is placed on the groundwater divide, with no surface run-off (French et al. 1994). The groundwater level is about 4 m. It is a station heavily equipped with: two lysimeter trenches (only one of them in use now with more than 120 suction cups), groundwater wells, piezometers, data loggers for registration and storage of climatic data, six boreholes for cross-borehole resistivity measurements (details given in method section), four boreholes for cross-borehole ground-penetrating radar (GPR) measurements and a multi-compartment sampler. The boreholes were installed winter 08/09.

The lysimeter trench is constructed as an underground basement (7m long, 3 m wide and 2.4 m deep) with walls of waterproof plywood (French et al. 1994).

The unsaturated zone at Moreppen is highly heterogeneous with alternating and tilted layers of varying texture. The sediments are seen to be mainly coarse and medium sand with a high content of gravel, similar to that seen in (Figure 2). The soil at Moreppen is assumed to be undisturbed as this area was not affected by the construction of the airport, thus Moreppen has been used as a reference area for research on activities associated with the airport. This includes research on flow and transport in the soil profile, both of de-icing chemical and petroleum products to assess the risk of airport activities on the groundwater contamination (French et al. 1994).

## 2.3 De-icing chemicals

In this thesis, the flow of tracer and de-icing chemicals are monitored by the use of cross-borehole resistivity surveys. In this section, some background on the de-icing chemicals used at OSL is presented. The use of de-icing chemicals is essential at airports in cold climates, such as OSL, to provide safe air-traffic. The chemicals are used to de-ice airplanes, taxiways and runways by lowering the freezing point of water, causing snow and ice on the surface to melt and prevent the formation of new ice and snow layers. At OSL, propylene glycol (PG) is used to de-ice airplanes and to de-ice taxiways and runways potassium formate (KFo) is used (Øvstedal & Weiden 2007). The usage of de-icing chemicals has increased the last winter seasons, both PG and KFo due to tougher winter conditions the past few years and increased area of taxiways that needed de-icing. The challenge concerning de-icing chemicals facing OSL now, is handling more surface water from the possible expansion of another terminal building (OSL 2009a). The environmental effect of using de-icing chemicals the winter season 2008/09 was calculated by OSL (2009b) to be 164 COD, the highest it has been since the airport opened. About 80% of the used PG at OSL is collected at the de-icing platforms, where based on concentration, some is reused and some is used as carbon-source at a local wastewater treatment plant (French et al. 2000b). The PG not collected either follows the airplanes after takeoff or drips from the planes along the runway systems. KFo and PG that ends up on the sides of the runway systems, infiltrates the sides of the runway system and are degraded through natural biological processes in the soil. Due to mechanical removal of snow from the runways, most of the chemicals end up being spread to a distance of 30 – 50 m from the runway (French et al. 2009a).

### 2.3.1: Propyleneglycol (PG)

The de-icer used on airplanes at OSL is "Kilfrost" type I and II which are products based on the chemical PG (C<sub>3</sub>H<sub>8</sub>O<sub>2</sub>) (French et al. 2001). PG is a relatively small organic molecule with a log K<sub>ow</sub> coefficient of -1.41, accordingly low adsorption (K<sub>ow</sub> is explained further in section 3.1.5). The compound is completely degraded under aerobic conditions, via several organic acids such as lactic and pyruvic acid which are also easily degraded under aerobic conditions (French et al. 2000a):



The chemical oxygen demand (COD) of the complete degradation of PG (1 ml/l) is 1.68 mg/l. Under anaerobic conditions, intermediate degradation products may be formed, such as propanol, acetate, mercaptane and methane. Mercaptane is a chemical of environmental concern as it is a toxic gas with an unpleasant smell of rotten onion (French et al. 2000a). PG has been shown in field experiments (French 1999) not to have any retardation and this means that the transport velocity of the compound will in theory be the same as the water front (Appello & Postma 1993).

Both field and lab experiments suggest that microbial degradation of PG follows first order kinetics and the coefficient of degradation is temperature dependant where rate of degradation increases with soil temperatures (French et al. 2001). The coefficient of degradation of PG at 8°C is 0.06 day<sup>-1</sup> (French et al. 2000b). This value, however, assumes that the only limiting factor for degradation is the amount of available substrate. Rates of degradation of both KFo and PG have been shown to increase if the soil is fertilized with phosphorus and nitrogen, hence the soil at OSL is fertilized during the summer months (French et al. 2000a).

### **2.3.2 Potassium Formate (KFo)**

When OSL opened, Clearway 1 was used as runway de-icer. This is a compound based on Potassium acetate ( $CH_3COOK$ ) as the main component (French et al. 2001). Now, only potassium formate (KFo) ( $CHKO_2$ ) is used and the commercial chemical is called Aviform. The reason for this change was that it was thought that KFo consumes less oxygen than KAc when degraded (French et al. 2009a). OSL was therefore given an expansion in their discharge permit when changing to KFo. However, research has shown that KFo consume as much oxygen when degraded as KAc does (French et al. 2000a). The use of KFo is also thought to have greater risks concerning long term effects as iron and manganese will slowly be removed from the soil profile.

KFo is a small organic molecule which is easily degraded under aerobic conditions with low toxicity. Many of the experiments carried out at OSL and Moreppen previously have used KAc, but as both KAc and KFo have many of the same chemical properties, it has been assumed that they behave similarly. Both are soluble in water and in contrast to PG which has been shown in field experiments not to be absorbed by soil particles, shows some signs of adsorption (French et al. 2001). As KFo is a salt, it dissolves to formate and potassium in water:



Both the resulting ions may take part in the ion exchange processes in soil. As soil particles are negatively charged, formate is expected to show little sorption, while adsorption of potassium is expected over time. This could potentially affect the water chemistry in groundwater (French et al. 2000a). However, it is thought that the adsorption of potassium due to infiltration of de-icing chemicals will not affect the water quality at Gardermoen due to the low background concentration of potassium in the groundwater. The recommended level for potassium in drinking water is far higher than what can be expected from the addition of infiltrating de-icing chemicals. KFo is thought to not be bioaccumulating (French et al. 2000a). Fo is in equilibrium with formic acid when dissolved:



Under aerobic conditions, formic acid will fully degrade:



The COD for complete degradation of KFo (1 ml/l) has been found to be 0.35 mg/l (French 1999; French et al. 2000a). The degradation of KFo has also been found to follow first order kinetics, where lab experiments suggests that the degradation coefficient at 8°C is 0.02 day<sup>-1</sup> (French et al. 2000b). KFo represent a low COD load to the soil and is currently the most environmentally friendly runway de-icer on the market (Øvstedal & Weiden 2007).

### 2.3.3 The environmental risk of de-icing chemicals

The greatest problem with release of de-icing chemicals to the environment is that they require high concentrations of oxygen for full degradation and this can lead to reduced amounts of dissolved oxygen. Periods of water saturation or during heavy loads of chemicals, the soil may be oxygen depleted and other electron acceptors will be used by the microbial organisms in the degradation process, such as nitrate, manganese, iron, sulphate and carbonate in this order. As a result, zones composted of different chemicals in the groundwater might occur, from the source of de-icing chemicals and following the flow of the groundwater. Close to the source, there will be methane production, followed by zones first of sulphate reduction, then iron reduction, manganese reduction, nitrate reduction and aerobe degradation where oxygen is still available. Anaerobic degradation of organic chemicals is slower than under aerobic conditions and there is a lag time after pollution of de-icing chemical before anaerobe degradation takes place. Under anaerobic conditions, the pollution plume can therefore spread to a greater area (French et al. 2000a). Research has shown that high concentrations in KAc and PG are linked to high concentrations of manganese (French 1999; Jaesche et al. 2006). Released manganese in soil particles is a result of anaerobic oxygen. This is usually not a problem in the unsaturated zone; however, anaerobic conditions can occur locally, for example in stagnant water. It could result in increased concentrations of manganese in the groundwater (French et al. 2000a). In periods where the concentration of de-icing chemicals are low, manganese will dissolve (Jaesche et al. 2006). There has not yet been shown that pollution of de-icing chemicals leads to dissolution of heavy metals from the soil profile. Carbon from humus horizon may dissolve under anaerobe conditions and transported to the groundwater. This was early documented in field experiments (French et al. 2000a) and this could lead to manganese and carbon being replaced in the soil profile under anaerobe conditions and result in chemical change of the groundwater. At OSL, high concentrations of iron in the groundwater has been found suggesting that organic compounds have lead to anaerobic conditions in the groundwater (OSL 1999).

At high concentrations, PG and KFo can be toxic to aquatic organisms. Corsi et al. (2006) found that organisms were more sensitive to type IV fluids than type I. The acute toxicity endpoint for type I fluids varies from 1550 mg/l to 45 100 mg/l, while type IV fluids all had their endpoints below 2000 mg/l. Hartwell et al. (1995) found that de-icing chemicals have the potential to damage ecosystems, especially due to the possible lowering of the concentration of dissolved oxygen. Evans and David (1974) showed that PG can have

negative effect on kidneys and the nervous system in mammals. In drinking water, the concentration should not exceed 1 mg/l. Glycol-based de-icing chemicals have higher toxicity than pure glycol-compounds (Pillard & DuFresne 1999). The half life, the time it take to degrade half the original concentration of a compound, for PG and KFo is 2.6 to 54 days, and 2.6 to 61 days, respectively. The variations are due to temperature differences and the available nutrients in soil. It has been shown in field infiltration experiments that concentrations of KFo and PG after 128 days are 0.04 and 8% respectively (French et al. 2000b). The environmental concern is higher for PG than KFo due to the slower degradation under aerobic conditions and a higher COD.

De-icing chemicals often contain additives and these have been shown to be toxic to aquatic organisms (Corsi et al. 2006). Additives are treated as industrial secrets and producers of de-icing fluids do not have to identify the chemicals or their risk to the environment. These additives have various properties, such as pH-adjusters, flame retardants, grease removers, polishing agents, emulsifiers, biocides and colouring agents. OSL have their own specification requirements to producers where additives have to be identified with environmental risk and toxicity to aquatic systems (Weideborg 2008). High concentrations of additives in soil slows down the microbial degradation of PG and FKo (Corsi et al. 2006). Triazoles and sodium petroleum sulfonates, which are the additives with greatest environmental concern (Corsi et al. 2006) have now been forbidden by OSL (Weideborg 2008).

### **2.3.4 Discharge permit for de-icing chemicals**

Both Norwegian Water Resources and Energy Directorate (Norges vassdrag- og energidirektorat, NVE) and Norwegian Climate and Pollution Agency (Klima- og forurensningsdirektoratet, Klif) have under the Pollution Act and the Water Resource Act given strict regulations to OSL concerning the use and discharge of de-icing chemicals. These were the strictest international regulations to an airport when OSL was opened (French et al. 2009a). Runoff from the airport, both to groundwater and surface runoff in the area around the airport has to be protected, quality and quantity. Due to the protected area around the airport, activities at the airport are regulated through law not to affect the erosion processes in the ravine landscape. Runoff from OSL cannot cause oxygen depletion in the rivers close to the airport due to runoff and no influence on the kettle hole lakes in the area (OSL 1999). NVE has given permission to OSL for the use of de-icing chemicals and for their infiltration into the soil profile along the runways. The requirement is that the soil has to have the capacity to degrade the chemicals and that no traces of the chemicals are found in the groundwater. Although the groundwater is not used as drinking water today, Klif requires that the groundwater is not to be polluted so it can be a potential drinking water source in the future (French et al. 2009a). The regulations through the discharge permit of de-icing chemicals which OSL has received from Klif is 168 ton PG and 635 ton KFo and a fine of 2 mill NOK is given OSL if de-icing chemicals are found in the groundwater (Klif 2001).



### 3. Theory

#### 3.1 Flow in the unsaturated zone

The focus here is to study the flow, both of water and de-icing chemicals, through the unsaturated zone due to its importance as a barrier against contaminants reaching the groundwater.

##### 3.1.1 Basic soil theory

The unsaturated zone is the volume of sediments below the surface and above the groundwater. The unsaturated zone is a three phase system: the solid phase is made up of mineral matter and organic matter, the liquid phase which consists of soil water containing dissolved solutes and the gaseous phase consisting of air (Hillel 1982). The transport of water and gas takes place through void spaces. The porosity,  $\phi$  ( $\text{m}^3/\text{m}^3$ ), of a medium is defined as:

$$\phi = \frac{V_V}{V_T} \quad \text{Equation 5}$$

where  $V_V$  is the volume of voids ( $\text{m}^3$ ) and  $V_T$  is the total volume ( $\text{m}^3$ ) (Domenico & Schwartz 1998). Not all pores in a medium are available for fluid flow; some may be too small and others isolated. The pores which take part in fluid flow are referred to as effective porosity and is the sum of all interconnected pores. Groundwater is the saturated zone where the ratio of water volume compared to void spaces in soil or rock is 1 (or 100%). This is the water saturation (further referred to as saturation),  $S$  ( $\text{m}^3/\text{m}^3$ ), can be expressed as a ratio between water volume,  $V_W$  ( $\text{m}^3$ ), and volume of void spaces,  $V_V$  ( $\text{m}^3$ ):

$$S = \frac{V_W}{V_V} \quad \text{Equation 6}$$

The value for  $S$  varies between 1 and 0. It is less than 1 in the unsaturated zone, indicating that air occupies some of the void spaces (Domenico & Schwartz 1998). The water content can be expressed in percentage where full saturation is equal to the porosity. The volume of water and gas in the pores varies spatially and temporally due to climatic conditions, such as evaporation and rain, and with different forces acting upon water trying to achieve a state of equilibrium between the two phases.

As water content of soil decreases, generally the pressure head becomes more negative causing the capillary pressure to increase. The reason for the increase in capillary rise is due to the remaining water finding itself in smaller and smaller voids as the soil dries (Domenico & Schwartz 1998). This relationship between pressure head and water content is described by a water retention curve. Water retention characteristics describe the ability of the soil matrix to bind water.

##### 3.1.2 Movement of water in the unsaturated zone

In general, water movement is driven by difference in energy which can be described in terms of potential energy and kinetic energy. Because the velocity of the water movement is low, the kinetic energy can be neglected compared to water potential energy. The flow in the

unsaturated zone is more complex than in the saturated zone. In the saturated zone, the driving force for groundwater is the hydraulic head,  $h$  (m),

$$h = z + \psi \quad \text{Equation 7}$$

where  $z$  is the elevation head (m) and  $\psi$  is the pressure head (m) (Domenico & Schwartz 1998). The hydraulic head is the water's potential energy in weight basis. Darcy's Law:

$$q = -K \frac{\Delta H}{x} - K i \quad \text{Equation 8}$$

describes this flow, where  $q$  is the volumetric flow rate per unit surface area with units of velocity (m/s) or the specific discharge,  $K$  is the constant of proportionality with units of velocity (m/s),  $\Delta H$  is the change in hydraulic head (m) along a distance  $x$  (m) and  $i$  is the dimensionless hydraulic gradient. The specific discharge can be divided by the effective porosity to get a more "realistic" velocity (Domenico & Schwartz 1998).  $K$  from Darcy's Law expresses how easily a fluid is transported through a porous medium. Darcy's Law is a general equation that describes flux of water in one dimension,  $x$ , through a homogeneous porous medium. It can also be used to describe flow in three dimensions where  $q_{xyz}$  (m/day) is the hydraulic gradient with respect to the Cartesian coordinates,  $x, y$  and  $z$  (Appello & Postma 1993):

$$q_{xyz} = \left(-K \frac{\partial h}{\partial x}\right) + \left(-K \frac{\partial h}{\partial y}\right) + \left(-K \frac{\partial h}{\partial z}\right) \quad \text{Equation 9}$$

The same concepts apply to water movement in the unsaturated zone, but with complications which has to be considered. The flow processes in unsaturated zone often entails changes in the state and content of soil water during flow and involves complex relations between the soil variables: soil wetness, suction, and conductivity which again can be complicated by hysteresis (Hillel 1982). The pressure head in the unsaturated zone is less than the atmospheric ( $\psi < 0$ ), in the saturated zone the pressure is greater than atmospheric ( $\psi < 0$ ) and at the groundwater surface the pressure is equal to the atmospheric pressure ( $\psi = 0$ ). The negative pressure head in the unsaturated zone (also referred to as either tension head or suction head) is due to matrix forces which are acting between the soil water and the soil matrix. These forces consist of capillary forces and adsorption of soil water or ions in the water to the negative surface of soil particles (Domenico & Schwartz 1998). Flow of water is in the direction of decreasing potential and the rate of flow (flux) is proportional to the potential gradient and is affected by the geometric properties of the pore channels. Flow in unsaturated zone is expressed by Richard's equation:

$$q = -K(\psi) \nabla H \quad \text{Equation 10}$$

where the conductivity,  $K$ (m/s), now is a function of the matrix suction head  $K = K(\psi)$  (m/s), and  $\Delta H$  is the hydraulic gradient (m) which may include both suction and gravitational components (Hillel 1982).

Water in the unsaturated zone percolates generally vertically downwards, towards the groundwater, along the maximal gradient of soil moisture potential, where relief is moderate.



A simple mass balance can give the rate of percolation at steady state, where  $v$  (m/yr) is the velocity in the unsaturated zone,  $P$  (m/yr) is the precipitation surplus and  $\phi_w$  ( $m^3/m^3$ ) is the water filled porosity:

$$v = \frac{P}{\phi_w} \quad \text{Equation 11}$$

A water flow velocity that is simply determined by the mass balance described by equation 11, means that newly infiltrating water pushes the old water ahead, down vertically through the unsaturated zone. This type of flow is known as a piston flow (Appello & Postma 1993).

### 3.1.3 Infiltration

In natural systems, the infiltration in the unsaturated zone is not a steady state flow. Small scale heterogeneity such as uneven distribution of macro and micro pores and aggregate formation can lead to focused infiltration. The infiltration rate is complicated to quantify but is of importance when studying the risk of contaminating the groundwater as preferential flow can reduce the residence time of infiltration water in the unsaturated zone (Hillel 1982). Transport studies of inactive tracer in a natural soil profile at OSL revealed that the flow through the unsaturated zone is mainly gravity-dominated. The displacement has been seen to be highly dependent on cumulative infiltration during snowmelt and autumn rains (French 1999).

Frost in the ground complicates quantifying the infiltration rate further, especially as the formation and distribution of frost fluctuates in time and space. Some years, the cycle of repeated melting and freezing can give rise to a solid layer of ice below the snow cover and this reduces the infiltration capacity as well as creating heterogeneous infiltration. Infiltration of melt water from snow occur mainly in macro pores. The pressure gradient due to the phase transition from liquid to solid water transporting water to the frozen soil is another factor which reduces the infiltration capacity. The phase transition causes a significant suction gradient which makes the soil below the freezing front extremely dry. The infiltration capacity of this dry soil found below the freezing front is very low as the unsaturated permeability of soil is a function of the water content. Frozen soil can also inhibit the infiltration of melt water and this will lead to ponding in topographical depressions on the soil surface. The recharge is likely to be focused as a result of ponding and reduced permeability due to ground frost and thin ice layers. This creates risk of contaminating the groundwater, in cases such as OSL, as focused infiltration of thawing soil at the end of the snow melting period from the pond will occur. After ponding, frost fissures can result due to desiccation of fluid water, leading to high infiltration capacity (Kitterød 2008; French, 1999).

### 3.1.4 Movement of solutes

Dissolved chemicals in soil water are transported through the soil by advective flow of water, described by Darcy's Law in three dimensions as seen in equation 9. Biological, physical and chemical processes will affect the concentration of dissolved chemicals in the soil profile. Sorption of chemicals to the soil particles reduces the velocity of the chemicals compared to the velocity of water. This is a result of adsorption sites on the soil particles which must first be "filled" by the chemical to conform to the required distribution, before further transport is

possible. Many organic pollutants are hydrophobic which means they prefer solution in apolar liquids, hence these pollutants are readily taken up in organic matter in sediments. The tendency of an organic pollutant to be adsorbed is related to the distribution coefficient,  $K_{ow}$ , of the chemical between water and an apolar liquid, such as octanol. Hydrodynamic dispersion causes scattering of the solute molecules by diffusion and dispersion. Diffusion is the physical spreading of molecules due to a concentration gradient in stagnant water while dispersion is the spread of molecules due to water flow. Chemical and biological degradation and precipitation, as well as other forms of dissolution, affects the total concentration of the solute. Combining these processes in one equation to describe the change in concentration due to transport, dispersion and sorption can be done, where  $C$  is solute concentration (mol/l),  $t$  is time (s),  $v$  is porewater flow velocity (m/s),  $D_L$  is the hydrodynamic dispersion coefficient ( $m^2/s$ ),  $x$  is a distance (m),  $q$  is the concentration on solid (mol/ l of porewater) (Appello & Postma 1993):

$$\left(\frac{\partial C}{\partial t}\right)_x = -v \left(\frac{\partial C}{\partial x}\right)_t + D_L \left(\frac{\partial^2 C}{\partial x^2}\right)_t - \left(\frac{\partial q}{\partial t}\right)_x \quad \text{Equation 12}$$

Most recharge to aquifers takes place by infiltration of surface water through the unsaturated zone. Infiltrating water transports the solutes down towards the groundwater and during this passage; the contaminants are diluted and dispersed while being transported through the pore matrix. The velocity of the contaminant flow through the unsaturated zone is affected by pore structure, hydraulic conductivities and the saturation level in the region.

The solutes in focus here are de-icing chemicals, and they are easily degraded. Degradation in soil is determined by several factors, such as; soil temperature, initial biomass, water content, available carbon substrate, oxygen and nutrients (nitrogen and phosphorus) (Kieft et al. 1993). Limiting factors for growth such as carbon source, nitrogen and phosphorus are spread in the heterogeneous environment and so is the distribution of microorganisms. It is normal to find the highest densities of microorganism populations close to the surface where the carbon source supply usually is (French 1999).

## 3.2 The resistivity method

### 3.2.1 The basic principle of the resistivity method

The direct current (DC) resistivity method (further referred to as resistivity method) measures the apparent resistivity of the ground. It is the measure of the resistivity of a material, which is a diagnostic and fundamental property of all geological materials. Resistivity is the inverse of electrical conductivity (EC). The basic definition of resistivity is explained by figure 3, where a current,  $I$  (A), passes through an electrically uniform cube of side length  $L$  (m). The material within the cube resists the conduction of electricity passing through it and this results in a potential drop,  $V$  (V), between the opposite sides of the cube (Reynolds 1997).

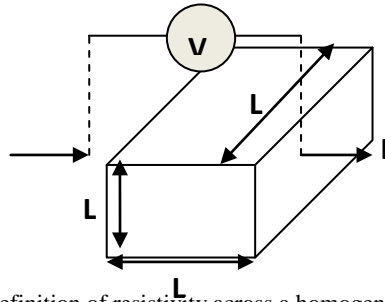


Figure 3: Sketch of the simple definition of resistivity across a homogeneous block of side length ( $L$ ) with an applied current ( $I$ ) and a potential drop between opposite faces ( $V$ ). (Adapted from Reynolds (1997)).

The resistance of the cube,  $R$  ( $\Omega$ ), is proportional to the length,  $L$  (m), and inversely proportional to the cross-sectional area,  $A$  ( $m^2$ ). Resistivity,  $\rho$  ( $\Omega m$ ), is the constant of proportionality:

$$R = \rho \frac{L}{A} \quad \text{Equation 13}$$

Ohm's Law:

$$R = \frac{V}{I} \quad \text{Equation 14}$$

states that the ratio of the potential drop,  $V$ , (V) to the applied current,  $I$ , (A) also defines the resistance,  $R$  ( $\Omega$ ), of the cube and combining these two expressions gives the product of resistance,  $R$ , ( $\Omega$ ) and a distance,  $L$ , (m). Hence, resistivity has the units ohm-metres ( $\Omega m$ ) (Reynolds 1997):

$$\rho = \frac{VA}{IL} \quad \text{Equation 15}$$

The resistivity of geological materials exhibits one of the largest ranges of all physical properties. In sedimentary rocks, the resistivity of the interstitial fluid is more important than that of the rock. This is due to conduction in rocks occurs by pore fluids acting as electrolytes with the actual mineral grains contributing very little to the overall EC of the rock. Resistivity is influenced by factors such as soil type, porosity, connectivity of the pores and their tortuosity, the saturation level and temperature (Reynolds 1997). The three phases present in soil are air, fluid and solids and they affect the resistivity differently: air is an insulator, the water solution resistivity is a function of the ionic concentration and the resistivity of the solid grains is related to the electrical charges density at the surface of the constituents. The geometry of the pores (void distribution and form) determines the proportion of air and fluid present in the sediment. Clay particles conduct electricity not only through free pore-water but also through adsorbed water at the surface of the clay particles; hence, the resistivity of the solid matrix cannot be neglected in fine-textured soils. The soil at Moreppen does not contain clay and adsorbed water is therefore not an issue. Different ions, at the same concentration, in the soil solution do not affect the conductivity in the same way due to variations in ion mobility (Samouëlian et al. 2005).

The purpose of carrying out a geo-electrical survey, such as electrical resistivity tomography (ERT), is to determine the subsurface resistivity distribution by performing measurements at

the earth surface, either along the surface or using boreholes. Most ERT methods still adopt the four-electrode measurement approach which was traditionally used in exploration geophysics (Binley & Kemna 2005). The basic principle behind this involves a known current which is injected into the ground by the means of two current electrodes (A and B) and two potential electrodes (M and N) are used to measure the resulting voltage difference (Reynolds 1997). Referring to equation 14,  $V$  will be the measured primary (peak) voltage between the potential electrodes and  $I$  is the known injected current. The sub-surface is not a homogenous medium and the measured resistivity is thus not the “true” resistivity but the apparent resistivity,  $\rho_a$  ( $\Omega$  m). The apparent resistivity, unlike the true resistivity, is not a physical property of the subsurface; it is an average value for the ground taken as a homogeneous half-space (Reynolds 1997).

In the field an electrical current,  $I$  (A), is injected using a pair of current electrodes and the electrical potential,  $\Delta\phi$ , is measured between a pair of potential electrodes (Müller et al. 2010), together they produce the transfer resistance  $R$  ( $\Omega$ ).

$$R = \frac{\Delta\phi}{I} \quad \text{Equation 16}$$

For  $n$  electrodes there are  $\frac{n(n-3)}{2}$  independent transfer resistances. A transfer resistance is therefore the ratio of a voltage at one pair of terminals to the current causing it (Dailey & Owen 1991). The apparent resistivity is a product of this measured transfer resistance and a geometric factor,  $K$  (m), for a given electrode array:

$$\rho_a = RK \quad \text{Equation 17}$$

The geometric factor takes into account geometric spreading of the electrodes which varies for different configurations of electrodes. It gives a term with unit of length (m), where A and B are current electrodes and M and N are potential electrodes and the terms AM, MB, AN, and NB represent the geometrical distance (m) between the different electrodes:

$$K = 2\pi \left( \frac{1}{AM} - \frac{1}{MB} - \frac{1}{AN} + \frac{1}{NB} \right)^{-1} \quad \text{Equation 18}$$

The four main configurations are Schlumberger, Wenner, Dipole-Dipole and Square (Reynolds 1997). These can all be used for surveys with multi-channel system. In this project a dipole-dipole configuration was used. In this configuration, current is applied to two adjacent electrodes and the resulting voltage between all the remaining electrodes with the same distance between the pairs is measured (French et al. 2002).

Figure 4 illustrates the basic principle of resistivity method for a homogeneous sub-surface where voltage is generated by two current electrodes (A and B) injecting a known current, and two potential electrodes (M and N) which measures the potential drop.

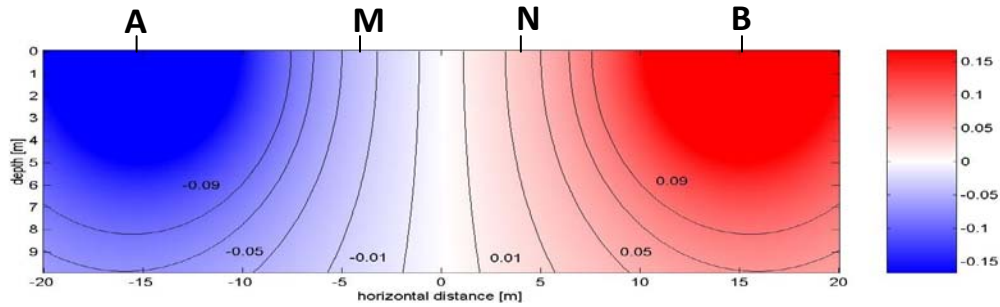


Figure 4: Current and equipotential lines produced by a pair of current electrodes (A and B) and the drop in voltage measured by the pair of potential electrodes (M and N) in homogeneous earth with Wenner configuration (Bloem 2002).

The lines shown are equipotential lines of equal voltage and current flow perpendicular to these lines in a homogeneous earth. In a homogeneous and isotropic half-space, electrical equipotential lines are hemispherical when the current electrodes are located at the soil surface. To increase the depth of the signal through the ground, the spacing between the electrodes can be increased. However, a small distance between the potential electrodes gives better signal-to-noise ratio (Reynolds 1997).

### 3.2.2 Cross-borehole ERT surveys

In this thesis, cross-borehole ERT surveys were carried out. Cross-borehole ERT surveying is an extension of the conventional surface resistivity imaging. By using measurements from electrodes in two or more boreholes, an image of the resistivity in the soil profile between the boreholes is obtained. The same arrays of electrodes in boreholes can be used to obtain a resistivity profile as with surface surveys. This method offers improved sensitivity to variations in electrical properties with depth compared to surface-applied surveys (Binley & Kemna 2005). There are various examples of this method and one of the first to demonstrate how this technique can be applied in hydrogeophysics is Dailey, et al. (1992). A wide range of applications for the use of cross-borehole resistivity in hydrogeophysical problems has developed, some include: vadose zone studies (e.g. Binley et al. (2002)), characterizing the transport of tracer in the subsurface (e.g. Kemna et al. (2002)), and monitoring leakage from underground storage tanks (Ramirez et al. 1996).

The main advantages of using cross-borehole compared to surface imaging are that this method offers higher resolution with depth and investigation can be made without the need for access to the surface (e.g. surveys under building). In comparison with surface surveys, cross-borehole method has been shown to provide high-resolution images of hydrogeological structures and, in some cases detailed assessment of dynamic processes in the subsurface environment (Binley et al. 2002). There are also some disadvantages and these include the fact that boreholes are required, data sensitivity is constrained to the region between the boreholes, more sophisticated instrumentation might be required for data acquisition, the noise level may be much higher for surveys in the vadose zone than using surface electrodes due to weaker electrical contact, and data processing is more complex (Binley & Kemna 2005). The conditions for cross-borehole imaging are extremely variable and the acquisition geometry should be considered on a case-by-case basis. The contrast in electrode contact and influence of backfill or any borehole water column will vary, and so will the separation

between boreholes and the instrumentation resolution and measurement rates (Binley & Kemna 2005).

### 3.2.3 Modelling and data inversion

The goal of resistivity surveys is to derive the distribution of low-frequency electrical properties inside an object. Generally the object of interest is the subsurface, from a set of measurements connected on the boundary of the object. The theoretical outcome of such a measurement can be determined mathematically (modelled) for given electrical properties of Poission's equation and subject to given boundary conditions. The Poission's equation defines the relationship of a three-dimensional isotropic electrical-conductivity distribution,  $\sigma(\mathbf{r})$  (S/m), the three-dimensional electric potential,  $V(\mathbf{r})$  (V), at a point,  $\mathbf{r}$ , due to a single current electrode, idealized as a point source at the origin with strength  $I$ :

$$\nabla (\sigma \nabla V) = -I \delta(\mathbf{r}) \quad \text{Equation 19}$$

The conditions set in this case are:

$$\frac{\delta V}{\delta \mathbf{n}} = \mathbf{0} \quad \text{Equation 20}$$

at the ground surface at the other infinite boundaries:

$$V = \mathbf{0} \quad \text{Equation 21}$$

This is the solution to the “forward” problem which is the determination of the outcome of the measurements based on the mathematical resolution of the governing physical equation for a given distribution of low-frequency electrical properties. However, for the purpose of subsurface investigations, the distribution of electrical properties (model) is used to explain the field measurements to an acceptable degree (Binley & Kemna 2005). Inversion theory is applied in order to determine an image of the measured resistivity. The “inverse” problem is the determination of the distribution of low-frequency electrical properties based on a given set of measurements. By dividing the domain of interest into parameter cells ( $j = 1$  to  $M$ ) the inversion solution is a resistivity distribution of block values that would theoretically compute the “best” set of resistivity values, which satisfies both the measured dataset and any prior constraint (Binley et al. 2002). There is therefore more than one inversion that can be the “solution”. The defined size of the parameter cells becomes the resolution limits of the model; although it is reduced somewhat by the implicit smoothing of the algorithm (French et al. 2002). The final model resolution is a complicated function of numerous factors such as electrode layout, measurement scheme, signal-to-noise ratio, resistivity distribution and the parameterization and regularization used in the inversion. First, electrical properties are discretized into a set of defining a model vector,  $\mathbf{m}$ :

$$\mathbf{m}_j = \ln \sigma_j \quad \text{Equation 22}$$

The logarithm accounts for the large possible range in earth conductivities. The given set of measured transfer resistances,  $\mathbf{R}$ , is defined by a data vector,  $\mathbf{d}$ :

$$\mathbf{d}_j = -\ln R_j \quad \text{Equation 23}$$

The minus sign accounts for physical dimensions. The aim of the inversion is to find a model,  $\mathbf{m}$ , which using the forward mapping according to equation 19, reproduces  $\mathbf{d}$  to the specified level of uncertainty. The inverse problem is solved as a regularized optimization problem:

$$\psi(\mathbf{m}) = \psi_d(\mathbf{m}) + \alpha\psi_m(\mathbf{m}) \quad \text{Equation 24}$$

The linear system of equations is as follows for each iteration,  $k$ :

$$(J_k^T W_d^T W_d J_k + \alpha W_m^T W_m) \Delta \mathbf{m}_k = J_k^T W_d^T W_d [\mathbf{d} - f(\mathbf{m}_k)] - \alpha W_m^T W_m (\mathbf{m}_k - \mathbf{m}_{ref}) \quad \text{Equation 25}$$

where  $W_d$  is a data weighting matrix associated with individual errors,  $W_m$  is a model weighting matrix,  $J_k$  is the Jacobian (sensitivity) matrix evaluated for the current model  $\mathbf{m}_k$ ,  $\alpha$  is the regularization parameter and controls the tradeoff between influence of data misfit and model objective function in the inversion,  $f$  is the forward mapping operator.  $\mathbf{m}_{ref}$  is a reference model which contains expected parameter values as well as results of a previous inversion or is just assigned to a homogenous half-space or the null vector if no additional information is available (Binley & Kemna 2005). The iteration process  $\Delta \mathbf{m}_{k+1} = \mathbf{m}_k + \Delta \mathbf{m}_k$  starts at  $\mathbf{m}_0$  (or  $\mathbf{m}_{ref}$  if available) according to equation 25 for a continued optimum choice of  $\alpha$  (deGroot-Hedlin & Constable 1990) until  $\psi_d(\mathbf{m}_k)$  matches the desired target value for the root-mean-square error,  $\epsilon_{RMS}$ , which is given by:

$$\epsilon_{RMS} = \frac{1}{j} \sqrt{\sum_{i=1}^j W_{\epsilon,i} (d_i - f_i(\mathbf{m}))^2} \quad \text{Equation 26}$$

where  $W_i$  is a diagonal matrix based on measurement error assuming that the measurement errors are uncorrelated (Koestel et al. 2008). In this case the target value for  $\epsilon_{RMS}$  is one. The challenge with the resistivity method is that there is no unique solution to the problem. This means that there typically exists a variety of different models that effectively produce the same response. And due to that fact that data are neither complete nor perfectly accurate, there is, with a given number of uncertainty, in principle an infinite number of models that fit the data. This can, however, be optimized. The resulting inversion models are approximations and can therefore act as a source of error. To ensure that a solution is reached, many inversion methods employ smoothing of some sort and this smoothing may be inappropriate (Binley & Kemna 2005).

Having this priori value controls the final solution in this form of inversion (Occam inversion) by finding the optimal solution within a range of solutions that provide the adequate data misfit and avoids continuous smoothing (Labrecque et al. 1996). An underestimation of data error leads to artefacts in the resulting inversion, but on the other hand overestimation results in overly smooth inversions (Koestel et al. 2008).

A map of accumulated sensitivity,  $s$ , of the inversion is a simple and effective way to look at the final model resolution. The sensitivity in ERT surveys states how a local change in electrical conductivity affects a single transfer resistance measurement. A poorly covered region is unlikely to be well resolved (Kemna et al. 2002). An accumulated sensitivity map of the spatial pattern is calculated for all individual measurements (Binley & Kemna 2005):

$$s_j = (J_k^T W_d^T W_d J_k)_{jj} \quad \text{Equation 27}$$

The program which is used in this thesis to calculate the resistivity models is R2, created by Andrew Binley. The R2 program is a forward/inverse solution for three-dimensional and two-dimensional current flow in a quadrilateral or triangular mesh. The solutions are performed using a finite element based algorithm, which accounts for three-dimensional current flow in a two-dimensional resistivity field. The inversion solution is an ‘‘Occam’’ type solutions (Binley & Kemna 2005), and is based on the series of equations explained in this section. The benefit of using this approach is that the misfit between measured and theoretical resistances for a particular resistivity distribution is minimised whilst maintaining a smooth resistivity (Labrecque et al. 1996).

### 3.2.4 Temperature correction

Temperature has a strong influence on the EC of the subsurface. EC of pore water increases with temperature due to increase in ion agitation as a result of decreasing viscosity of the fluid while the change in the surface EC of rocks and sediments due to temperature variations are caused by changes in the surface ionic mobility. These two mechanisms have different dependence on temperature (Hayley et al. 2007). A study carried out by Rein et al. (2004) showed that even diurnal temperature variations can have a relatively large effect on the EC. Campbell et al. (1948) found that the EC of alkaline and saline soils increased exponentially by about 2.02% per °C between 15 and 35 °C. It was suggested by Aaltonen (2001) that coarse-grained material presents a wider range in seasonal resistivity variations due to temperature than fine-grained material.

There are two proposed types of temperature dependence relationships concerning EC variations in sediments: one linear and one exponential. Campbell (1948) suggested a linear relationship explaining the dependence of temperature on EC, where  $\sigma_T$  (S/m) is the recorded EC at temperature  $T$  (°C) and  $\sigma_{T_{25}}$  (S/m) is the EC at the conventional reference temperature of 25°C, and  $m$  (°C) is the fractional change in EC per °C and varies for different materials and fluids:

$$\sigma_T = \sigma_{T_{25}} [1 + m (T - T_{25})] \quad \text{Equation 28}$$

Sen & Goode (1992) found supporting evidence to this relationship in shaly sands containing varying amounts of clays.

Llera et al (1990) proposed an exponential relationship between EC and temperature where  $A$  (J/mol) is the activation energy of conduction,  $R$  (J/kg K) is the universal gas constant,  $T$  (K) is temperature and  $\sigma_T$  (S/m) and  $\sigma_{T_{25}}$  (S/m) are the EC recorded at temperature  $T$  and at the reference temperature 25°C, respectively:

$$\sigma_T = \sigma_{T_{25}} e^{\frac{-A}{R} \left( \frac{1}{T} - \frac{1}{298} \right)} \quad \text{Equation 29}$$

Hayley et al. (2007) tested these two theoretical models. Their first observation was that equation 29, suggesting an exponential temperature relationship provides better results over a larger temperature range. Using equation 28, they found that linear relationships for the



temperature range 0-25 °C for approximating temperature dependence of surface and fluid conductivity have similar slopes, and their data is consistent with the theoretical models. For the temperature range 0-25 °C, also the one of interest in this study, the temperature dependence is not well described with petro-physical models calibrated to the range 25 – 200 °C. They suggest to use the linear approximation which is specific to the temperature range of interest, equation 28.

### 3.2.5 Time-lapse resistivity modelling

ERT provides an estimate of soil bulk electrical conductivity distribution. Soil bulk electrical conductivity is itself a function of soil structure, water content, pore water electrical conductivity and temperature. During infiltration events, most of these parameters remain constant while water content, pore water EC and/or temperature changes. In some cases, temperature is assumed constant while other studies include temperature as a seasonal variability (e.g Jayawickreme et al. (2008)) Changes in resistivity over time for a soil profile can therefore be used to observe these expected changes. This approach is called time-lapse imaging (Binley & Kemna 2005). The time-lapse inversion method used here is based on inverting the ratio of initial and subsequent datasets to obtain a combined dataset from:

$$C_{rat} = \frac{C_t}{C_{std}} C_F \quad \text{Equation 30}$$

where  $C_{rat}$  (S/m) is the conductance ratio to be inverted,  $C_{std}$  (S/m) and  $C_t$  (S/m) are the initial conductance measurements set as the standard and the measured conductance at time  $t$ , and  $C_F$  (S/m) represents the theoretical conductance that would be observed over a homogeneous half-space (Dailey & Owen 1991). The combined datasets are inverted like the individual inversions.

### 3.2.6 Interpretation of resistivity data

Quantifying ERT measurements can be carried out using petro-physical relationships. Establishing these relationships has been a topic of intense work (Day-Lewis et al. 2005). Forquet (2009) explored different empirical ways to relate water content to bulk EC and estimated fitting parameters for soil samples from Moreppen. He recommended using an approach published by Yeh et al. (2002) for predicting water content due to the fact that they studied relative changes rather than absolute ones. They used a simple model to relate water content to soil bulk resistivity, where  $\rho_b$  ( $\Omega$  m) is the bulk resistivity of the soil,  $\theta$  is the water content ( $m^3/m^3$ ),  $\rho_0$  ( $\Omega$  m) and  $m$  are a fitting parameter:

$$\rho_b = \rho_0 \theta^{-m} \quad \text{Equation 31}$$

Looking at the difference in natural log resistivity before and after infiltration, the equation becomes linear:

$$\Delta \ln \rho_b = -m \Delta \ln \theta \quad \text{Equation 32}$$

Another relationship was found by Archie who suggested that bulk soil resistivity and saturation followed a power law, called Archie's Law and can be expressed as:

$$\rho = a \phi^{-m} S^{-n} \rho_w \quad \text{Equation 33}$$

It is an empirical formula for the effective resistivity of a rock formation,  $\rho$  ( $\Omega$  m), which takes into account the porosity,  $\emptyset$  ( $m^3/m^3$ ), the saturation level,  $s$ , and the resistivity of the water,  $\rho_w$  ( $\Omega$  m), where  $a$ ,  $m$  and  $n$  are fitting parameters. Sedimentary rocks have a variable composition; the resistivity will reflect the varying proportions of the constituent materials (Reynolds 1997).

Change in saturation can be calculated where  $S_{t_{std}}$ ,  $\rho_{s,t_{std}}$  ( $\Omega$  m) and  $\rho_{w,t_{std}}$  ( $\Omega$  m) are the saturation, bulk resistivity and pore water resistivity at a reference date and  $S_t$ ,  $\rho_{s,t}$  ( $\Omega$  m) and  $\rho_{w,t}$  ( $\Omega$  m) are the saturation, measured soil resistivity and measured water resistivity at the date of interest, and  $n$  is the fitting parameter (French & Binley 2004):

$$\frac{S_t}{S_{t_{std}}} = \left[ \frac{\rho_{w,t_{std}}}{\rho_{w,t}} \frac{\rho_{s,t}}{\rho_{s,t_{std}}} \right]^{-\frac{1}{n}} \quad \text{Equation 34}$$

The benefit of looking at the change in saturation is that porosity can be assumed not to change, hence the uncertainty of the estimated porosity is removed.

Estimating hydrologic parameters from geophysical data, although insightful, suffers from limitations arising from imperfect and variable tomographic resolution. Day-Lewis et al. (2005) refers to this loss of information through variable resolution as ‘‘correlation loss’’. The resolution depends on the measurement physics, the survey geometry, the parameterization and regularization used for the inversion and the measurement errors (Day-Lewis et al. 2005).

## 4. Method

### 4.1 Field work at Moreppen and field setup

As mentioned in section 2.2, Moreppen is heavily equipped and various experiments are carried out here. For this thesis, the focus is on the ERT data collected from the north and south wall during the snow melting 2010 and EC data from the suction cups from the south wall (Figure 5). Measurements were made at regular intervals by various participants of the SoilCAM project, including the author. A tracer experiment was carried out where on the 26<sup>th</sup> March 2010 inactive tracer (bromide, Br<sup>-</sup>) and de-icing chemicals (potassium formate (KFo) and propylene glycol (PG)) were applied with similar load to the amount applied close to the runway (Table 1). Bromide is an inactive tracer which is not adsorbed in the soil and does not degrade. Application of the chemicals was carried out by the use of KillaSpray (4612), which is a manual apparatus for spraying e.g. pesticides on vegetation, for the most even distribution of the chemicals on the snow. The commercial de-icing chemicals applied were Kilfrost type II which is PG based and Aviform which is KFo based. French (1999) showed that there was no difference in chemical leaking patterns from snow, between spraying chemicals on the surface and adding them as ice cores below the snow cover. The chemicals were applied on top of the undisturbed snow on either side of the trench. The area which de-icing chemicals were applied is seen in Figure 5.

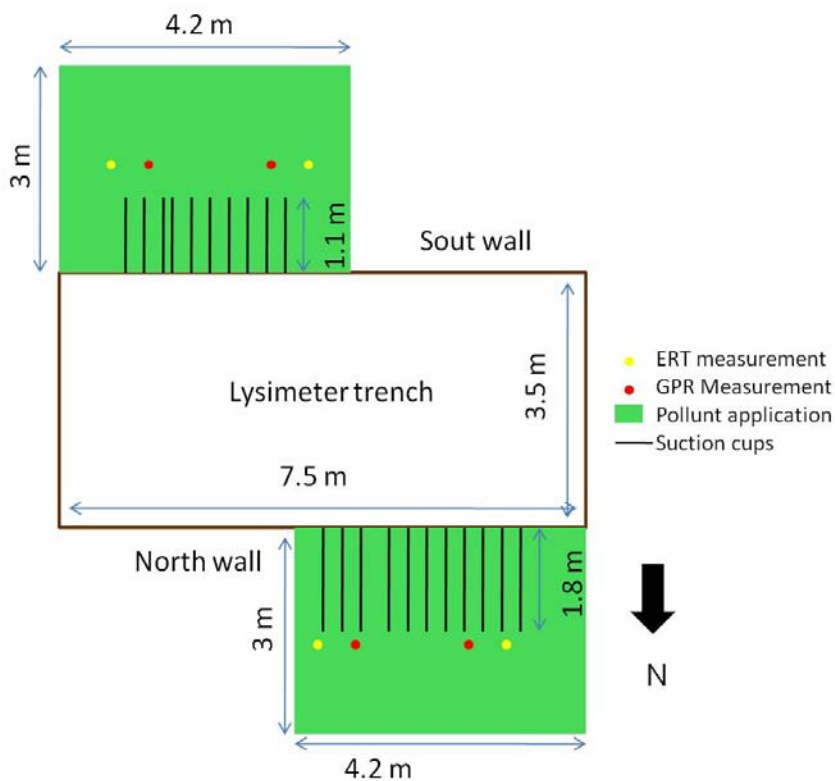


Figure 5: Sketch showing the locations of the ERT boreholes compared to the lysimeter trench, the GPR boreholes and the suction cups where the length indicated is the length of the suction cups furthest from the trench wall (Elkin 2011). The boreholes at the west wall are not shown.

### 4.1.1 Cross-borehole resistivity data gathering

ERT surveys were carried out for the whole period from mid March to July, for a representative amount of days. The set-up of the boreholes is seen in table 2. The boreholes were installed winter 08/09 due to practical reasons. The electrodes used were stainless steel mesh electrodes, mounted at 0.15 m intervals on a 4 cm diameter PVC pipe for each borehole. The top electrode is situated near the surface and the bottom electrode is located at a depth of 4.95 m. The boreholes were back-filled with sorted sand. This was not ideal and might have cause poor electrode contact, especially at the surface (French 2011).

Table 1: Specifications for boreholes

	North wall	South wall
Number of electrodes per borehole	34	34
Distance between electrodes	0.15 m	0.15 m
Depth of borehole	4.95 m	4.95 m
Distance from trench	1.8 m	1.4 m
Distance between boreholes	3.2 m	3.2 m
Amount of applied de-icing chemicals	500 g KFo/m <sup>2</sup>	1000 g PG/m <sup>2</sup>
Commercial name of de-icing chemical applied	Aviform	Kilfrost type II
Applied inactive tracer	10 g Br/m <sup>2</sup>	10 g Br/m <sup>2</sup>
Area which de-icing chemicals were applied	4.2 * 3 m = 12.6 m <sup>2</sup>	4.2 * 3 m = 12.6 m <sup>2</sup>

A Syscal Pro Switch (Iris instrument) (Figure 6) was used to obtain the ERT measurements. This is a versatile electrical resistivity meter, supplied by a 12 V battery, and combines a transmitter, a receiver and a switching unit in one single casing. The measurements are carried out automatically and stored in the internal memory (quality factor, output voltage, stacking number) after operator has selected limit values. The output specifications are 800 V (power switch), 1 000 V (manual mode) for the voltage, 2.5 A for the current and 250 W for the power using the internal DC/DC converter and battery (Bastani et al. 2010).



Figure 6: Syscal Pro Switch (Geo 2011)

A dipole-dipole configuration was used with a fixed spacing of 45 cm (three electrode-pair spacings) between both the current electrode pairs and the potential electrode pairs. One great advantage of using dipole-dipole configuration is that the acquisition time is reduced due to the possibility of multi-measurements. Data collection of one dataset took approximately 1.5 hrs. It is argued by Winship et al. (2006) that since the data capture time is critical it is recommended to be short as each image should reflect a “snapshot” of the infiltration through the subsurface. The reason for using a spacing of 45 cm is that the resolution towards the centre of the profile improves. In previous experiments, the boreholes were closer and therefore a resolution in the centre of the profile was sufficient with 30 cm electrode-pair spacing. With this electrode spacing, if current is applied between electrode 1 and 4, the potential difference is measured between electrodes 2 and 5 then 3 and 6, then 5 and 8 and so on until every possible combination of electrode pairs with this spacing has been measured. Current is then applied to electrode pair 2 and 5 and the procedure continues.

For each set of two boreholes, 2074 measurements were programmed. The normal and the reciprocal dipole-dipole measurement were measured, hence the total of 4148 measurements were recorded. Rather than repeating a measurement to ensure data quality, reciprocal measurements are measured and this is part of the program run. This is done by swapping the potential and current electrodes. The reason to use reciprocal measurements to estimate errors is that the repeatability of resistivity measurements does not provide an adequate error estimate. Anomalies, such as poor electrode contact will give the same reading if a measurement was repeated; hence the error would not show. The theory behind using reciprocal measurements is that the resistance measured should be the same even when swapping current and potential electrodes. This permits removal of outliers prior to data inversion and also allows characterization of data weights for the inversion process.

#### **4.1.2 Pore water EC data from suction cups**

The aim of using a lysimeter trench is to monitor water flow and pollutant transport by extracting soil water from the different depths of the soil profile. The location of the lysimeter trench at Moreppen is shown in Appendix II.

In the south, north and west wall of the trench suction cups, made of Teflon (Teflon avoids ion sorption compared to using ceramics) were installed in the period 1993-4. In this thesis, only water samples from the south wall are used. The Teflon suction cups have a pore size of  $2\ \mu\text{m}$  and a porous area of  $33\ \text{cm}^2$  (Prenart) The suction cups are placed in the whole profile and to ensure that the soil remained undisturbed above the suction cups, the distance from the wall increases with 10 cm for each deeper layer of suction cups. A vacuum pump ensures the designated constant suction of the set up (French et al. 1994). As seen in Figure 5 above, the area monitored between the boreholes both for GPR measurements and ERT are the same as that monitored by the suction cups, hence the same infiltration of snow and chemicals (Table 1). A diagram showing the distribution of the suction cups in the south and north wall is seen in figure 7 and this illustrates the resolution limits of the pore water EC data in the profiles. The suction cup placed at 4.5 m depth, both in the south and north wall is to allow groundwater to be sampled (French 1999). The coordinates of the location of the suction cups in the south wall are given in appendix 1.

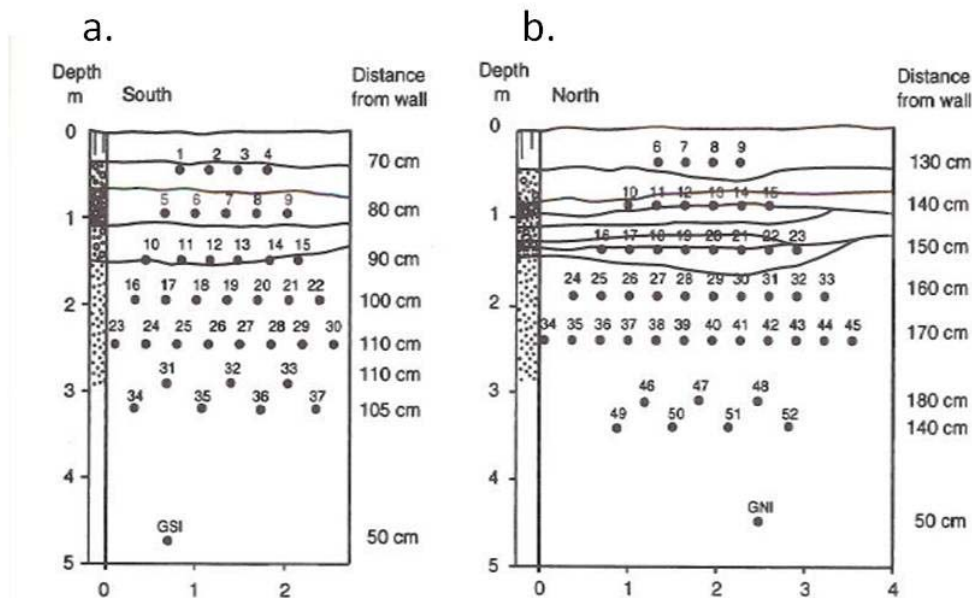


Figure 7: Diagram showing the distribution of suction cups in the south (a) and north (b) walls of the lysimeter trench at Moreppen. One number represents one suction cup in the soil profile. The X and Y coordinates for the location of suction cups in the south wall are given in appendix 1 (French 1999).

A closed system of PVC pipes connects each suction cup in the soil profile to its respective Prenart collecting bottle inside the lysimeter trench (Figure 8). The sampling system is divided into two parts, through a net of PVC pipes from the bottles; system 1 including the upper three layers of suction cups, and system 2 including the two lower layers of suction cups. Each system is connected with PVC pipes to its respective Prenart vacuum pump. The applied suction should be as small as possible to limit the influence on the natural flow patterns of water in the soil profile. Suction is needed due to the low potential head in the unsaturated zone; it is required to collect water from the soil. The vacuum pump was set to a constant suction 0.15 bar from December 2009. Before this the vacuum pump was coupled up to tension meters in the profile so that the suction applied varied with the natural variations, with a minimum suction of 0.03 bars. However, it was found that not all tension meters

worked properly a fixed suction was applied (Elkin 2011). Soil water first runs into a test tube before running into the collecting bottle. The water sample in the test tubes were collected when filled with water and frozen for later measurements in the laboratory using a conductivity meter. Conductivity measurements in the laboratory were carried out by Kyle Elkin, Gro Eggen and Kari Horgen Skjønberg.

a.



b.

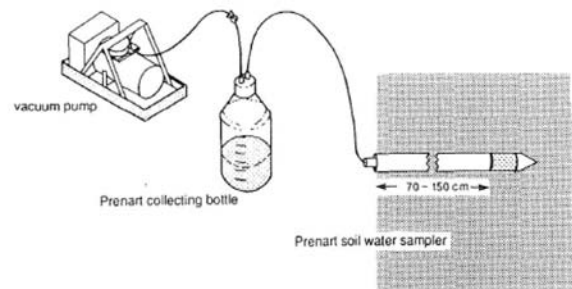


Figure 8: A) Picture inside the lysimeter trench (French 1999). B) Sketch showing the principle behind the suction cups extracting water at the lysimeter trench at Moreppen. Suction is created by the vacuum pump in the Prenart soil water sampler (location of the samples shown in figure 7 and water is extracted from the soil profile and collected in the Prenart collecting bottle.

Since the suction cups have been installed in the profile for a long period, some are not working as well as they did initially. As a consequence not all test tubes filled up each day, and the data was therefore interpolated by Robert Barneveld. He wrote a program which goes through the data and extracts a value for suction cups without readings for that particular day. It looks at the three nearest neighbour values collected the same date and applies inverse distance weighting to come up with an average value. The weighing factor was catered for higher weights for neighbour values higher up in the profile (Barneveld 2011). The pore water EC from suction cups data was extrapolated using kriging in surfer to fit the same profile size and grid resolution as the ERT inversions. Kriging is a geostatistical approach to interpolate a value at an unobserved location from observations of its value at nearby locations. Surfer uses the measured points from the suction cup locations and extrapolates this for the whole profile. As few data points were available from suction cups, kriging was found to be the most appropriate method of interpolation.

#### 4.1.3 Air and soil temperature data

Temperature of the soil profile at Moreppen was constantly measured with a thermistor every hour at depths; 0.05, 0.1, 0.15, 0.2, 0.3, 0.4, 0.9, 1.4, 1.9, and 2.4 m and logged on a Campbell-logger (French 2011). The thermistors are placed 100 cm into the north wall of the lysimeter trench. The temperature values used in the temperature correction of the ERT data were averaged for the two hours in which the ERT measurements were carried out.

Air temperatures are also measured on hourly basis at Moreppen and logged using a Campbell logger which is located in the lysimeter trench. The location of where temperature is measured is shown on the map in Appendix II.

#### 4.1.4 TDR measurements

Soil moisture is measured continuously every hour using three Time Domain Reflectometry (TDR) units. The three TDRs are in quite close location of one another at Moreppen and the readings have been averaged to give one mean value per day during the snowmelt period. The units are placed southwest of the lysimeter trench so that they are not affected by the tracer experiment. The probes are 30 cm long and placed vertically down into the subsurface (French et al. 2006). The TDRs used here are of the type Campbell scientific TDR sensor and consists of 30 cm long probes (French 2011). Microwaves are emitted and received between the probes and relates the signal to water content using Topp's equations. (Davie 2003). Soils with different dielectric properties show an error that appears as a constant offset; to avoid this and a possible drift in the instruments, the change in TDR measurements are considered here rather than the averaged measured values. TDR do not measure frozen water, only liquid water.

#### 4.1.5 Groundwater level

Groundwater is measured continuously at Moreppen by a pressure sensor installed in a well, and logged every hour with a Campbell CR10-based-logger (French et al. 2002). The groundwater level values measured were averaged for each day. Daily averages were chosen over the two hours in which ERT measurements were carried out due to the fact that the groundwater does not show diurnal changes as temperature does and daily averages can be compared to cumulative snowmelt data which is calculated on daily basis. There was an apparent drift in the measurements which was corrected by considering the preceding trend. Data with obvious error were removed. The location of the well is marked on the map in Appendix II.

#### 4.1.6 Cumulative snowmelt

The cumulative snowmelt has been calculated for every day by Esther Bloem. This was done by placing a cylinder with a diameter of 50 mm into the snow cover at three different locations every day at Moreppen and weighing the snow which filled the cylinder at each place. Assuming 1 g snow = 1 ml water, the snow water equivalent (mm) has been found and averaged for the three locations using:

$$SWE = \frac{V \cdot 1000}{\pi r^2} \quad \text{Equation 35}$$

where SWE (mm) is the daily snow water equivalent in the snow cover, V is average volume of collected snow where the weight of snow collected is converted (g snow = ml water = 1000 mm<sup>3</sup> water) and r is the radius of the cylinder (mm).

The SWE was added together to form cumulative snowmelt starting on the 26<sup>th</sup> of March (day zero when tracer experiment started). The reason why it is the weight of snow which is used is that measuring the depth of snow would not give the precipitation equivalent, as snow will



compact over time. The total precipitation for the period of interest here, starting 26<sup>th</sup> of March 2010, measured at the weather station at OSL was added to obtain a cumulative infiltration of total snowmelt and precipitation for the period (Bloem 2011). As there is no run off at Moreppen, the cumulative snowmelt calculation is assumed the same amount as the infiltration. Considering cumulative infiltration rather than time has been shown to be useful when considering dispersion and concentration during infiltration (Wierenga 1977).

## 4.2 Resistivity data processing

The data processing of the cross borehole resistivity data entails to create an image in form of inversions of the profile between the two boreholes. At the north and south wall at Moreppen (Table 1), the profile between the boreholes is 3.2 m wide and down to a depth of 4.95 m and it is this area which will be images by the ERT survey. Both individual inversions and time-lapse inversions have been made and are explained in more detail below. An individual inversion is an inversion of the separate dataset for a day of interest, and a time-lapse inversion is an inversion showing the change in resistivity between a dataset of interest to a reference dataset. The individual inversions have first been temperature corrections have been carried out on the individual inversions to a temperature equivalent of 25°C and then converted to water content and saturation.

R2 requires an input file and the same file was used for both individual inversions and the time-lapse inversions. The finite element grid has to be defined in the input file. First a mesh of finer cells close to the boreholes and coarser in the middle of the profile was used. The reason this potentially could improve the models was that the data sensitivity is better close to the boreholes and having finer elements here would allow an improved visualisation based on the best resolution. However, it was found through sensitivity maps of these inversions that the data quality was not good enough for these fine elements and that the sensitivity was affected by the grid system. The effect of this first mesh has some effect on the individual inversions but surprisingly had a greater effect on the time-lapse inversions. After this was realised a new mesh of equal sized coarser elements within the boreholes was adopted. Within the borehole plane in the meshed used, there are 40 elements (41 nodes) in the horizontal axis from -1.6 m to 1.6m. The horizontal length of the elements is in the region between the boreholes. There are 66 elements (67 nodes) within the measured plane in the vertical axis from 0 to -4.95 m with 0.075 m as the vertical length of each element. However, the grid consists of 5928 elements giving the inversion additional finite elements and resistivity blocks outside the region of interest to allow assignment of boundary conditions at infinity, from 166 m to -166 m in the horizontal plane and down to a depth of -158.55 m vertically. The “pixel value” is the value assigned by R2 to these set resolution limits, although this limit is reduced somewhat by the implicit smoothing of the algorithm R2 is based on.

From the measurements collected in the field, the apparent resistivity of the normal and reciprocal were calculated using equation 17.

The error estimate was calculated for each data point by comparing reciprocal and normal measurements:

$$e = \frac{|\rho_N - \rho_R|}{\frac{|\rho_N + \rho_R|}{2}} * 100 \quad \text{Equation 36}$$

where  $e$  is error estimate in percent,  $\rho_N$  is the normal resistivity measurement ( $\Omega$  m) and  $\rho_R$  is the reciprocal resistivity measurement ( $\Omega$  m).

Data used in the inversions are average values of reciprocal and normal values. Two common datasets was created, one for the data collected at the south wall and one for the north wall. This was to allow the removal of the same anomalies for each date by comparing the error estimate and deviation for both normal and reciprocal for the same measuring point for the various dates. This was to reduce noise and to prevent misinterpretation of the inversions. The dataset for the north wall contained 1522 measurements and the south wall had 1469 using the same criteria; where only data points with more than 17 of the 33 dates had less than 10% error for a single point and a deviation less than 10 during the normal and/or reciprocal measurement were included. As argued by Koestel et al. (2008), this choice of threshold criteria is largely arbitrary as a constant threshold leads to bias in the spatial data point density when it is suggested by sensitivity maps that the electrode contact is varying due to frost and variations in water content. The reason for creating a common dataset is to ensure that image sensitivity is not biased by different measurements (French et al. 2002). Ideally, the common dataset should only have included datasets with low error. However, most of the datasets from the beginning of the experiment (March and early April) had the highest error and these were the dates of highest interest.

#### 4.2.1 Individual inversion models

A protocol file was made from the two common datasets for the south and north wall. The aim was to optimize the inversion models to obtain the smallest RMS misfit possible using the same input file and making sure the inversions converge in 10 iterations. The optimal is if the inversion converges within 5 to 7 iterations; if it converges at less iterations than the error weight might be too high. There are three various ways of weighting the data points in the model based on errors. Individual error weighting can be estimated and the forward modelling errors can also be estimated. However, in this case it was found that the errors due to other factors than modelling error and individual data error were greater. Most likely is this due to some errors in the data that the reciprocity and forward modelling do not account for. This might be due to things which are not modelled correctly in this case, such as the fact that point electrodes are not used, the effect of the annulus of the borehole and poor electrode contact due to frozen coarse grained sand at Moreppen (Binley 2010). These are effects which are not really included in the model and hence contribute to mismatch between measured data and the inversion. The optimal inversion model was found to be the simplest method of weighting data points based on error; by appointing one value of data weight error and in this case 10% was chosen. This is a high data weight error and was chosen due to the high error in the datasets (Binley 2010).

The minimum and maximum observed apparent resistivity values were set to infinite to not ignore any data points, as most of the anomalies had already been removed by the criteria in the common datasets. The reference resistivity value was set to be 20 000  $\Omega$  m for a

homogeneous resistivity field for all element blocks. R2 creates a file with pixel values of logarithm resistivity and gives a geometric mean of the apparent resistivity for each inversion. The benefits of logarithm values are that the inversion never yields negative, unphysical resistivity and the inversion gives more reliable results in situations where resistivity vary by orders of magnitude (Day-Lewis et al. 2005). The images have been made in surfer in a grid of 100 by 100 blocks, using nearest neighbour as gridding method. Nearest neighbour compares a point with the neighbouring points and not further, hence it is a suitable gridding method where there are many data points within the field of interest.

Melting of the snow pack can affect the surface boundary conditions (electrically). However, the snowpack is much more resistive than the soil and the effect of the snow pack thickness can therefore be ignored from the ERT inversions (French & Binley 2004).

Inversions with blocking for groundwater and anisotropy in the horizontal direction were also run to see if the inversion was improved. However, it was decided that this gave the model boundaries which might not exist.

To compare the individual inversions, ratios, ERT ratio, were calculated using the geometric mean apparent resistivity:

$$\mathbf{ERT\ ratio} = \frac{\rho_{std}}{\rho_t} \quad \text{Equation 37}$$

where  $\rho_{std}$  ( $\Omega$  m) is the mean apparent resistivity of the background dataset and  $\rho_t$  ( $\Omega$  m) is the mean apparent resistivity of the dataset at time t. 26<sup>th</sup> of March has been used as background to be able to compare the inversions to cumulative snowmelt calculations and this is the day chemicals were applied.  $\rho_{std}$  and  $\rho_t$  were temperature corrected using the average soil temperature for the two hours the measurements were carried out, using the temperature corrected explained below in section 4.2.3. The same equation was used to calculate changes in pore water resistivity from suction cups data.

#### 4.2.2 Time-lapse models

The same optimized input file as described above was used to create time-lapse models and the same protocol files were used. A program called ratio\_program calculates the ratio between the measured apparent resistivity from the background dataset and the dataset from the time step of interest, based on equation 30. This ratio is multiplied for each data point with the forward model values for a homogeneous resistivity field of 1  $\Omega$  m. The program was set to removed data with reciprocal error greater than 10%. The inversion using R2 was performed on these ratioed values. Time-lapse models were made both by using 22<sup>nd</sup> of March 2010 as background dataset (before application of de-icing chemicals) and 6<sup>th</sup> of October 2010 (after de-icing chemical application and potentially after degradation of the chemicals). The reason both these background datasets were used was that datasets collected early on in mid-March, contain a lot of error. Ratios are only calculated for data points present in both datasets, hence using a dataset with high error means few points are left to perform the inversion on. The dataset in October, on the other hand, has less error and is therefore a better background dataset to use as more data points are left to be inverted. However, as the raw data has not

been temperature corrected using October dataset as background means that changes in resistivity in these images are potentially more affected by temperature changes than using mid-March.

Another method of running time-lapse inversions is to use an inversion result of an initial data set as a reference model for the inversion of subsequent data sets. R2 will then run the inversions, attempting to calculate the pixel values as close to the reference pixel values as possible. Miller et al. (2008) found that this was the superior method for their situation. However, here this method did not give good results. The models only converged for the few first time steps. A reason for this might be because there is much change in the soil profile in the time period of interest. The geometric mean apparent resistivity for running these inversions using 22<sup>nd</sup> of March as reference datasets were found to be the same as obtained running the individual inversions.

### 4.2.3 Temperature correction

Resistivity is temperature dependant so when trying to quantify the results from ERT measurements, the signal from temperature needs to be removed to only observe changes due to water and solute. Hayley et al. (2007) suggested a method of correcting for temperature variations in time-lapse resistivity surveys. This method is based on equation 28. They found that for a temperature scale from 0-25°C, theoretical linear relationships between temperature and surface and fluid conductivity of sediments are similar to that observed in their laboratory data. The average estimated porosity of the samples in their study was 0.3 and the samples were glacial tills with sporadic pebbles and cobbles in the sandy clay matrix. The linear relationship they found is:

$$\sigma_{std} = \left[ \frac{m(T_{std}-25)+1}{m(T_i-25)+1} \right] \sigma_i \quad \text{Equation 38}$$

where  $\sigma_{std}$  (S/m) is the resistivity at the standard temperature,  $T_{std}$  (°C) is the standard temperature,  $\sigma_i$  ( $\Omega$  m) is the in situ resistivity,  $T_i$  (°C) is the in situ temperature and  $m$  (°C) is the fractional change in EC per °C for 25°C. Hayley et al. (2007) found  $m$  to be 0.0183.

As temperature dependence experiments on the EC of soil from Moreppen have not been carried out yet, the  $m$  suggested by Hayley et al. (2007) was used in this thesis work. Measurements in this thesis are carried out in mainly medium to coarse grained material, similar to the description of the sediments used by Hayley et al. (2007). Equation 38 was applied to the pixel values of the individual inversions, using 25°C as the standard temperature. This was due to the fact that the EC measurement data from the suction cups are automatically temperature corrected to 25°C by a conductivity meter and the two datasets can therefore more easily be compared.

The average soil temperatures measured during the same two hours as the ERT surveys were used. The temperature measurements were used for the intervals until the depth of the next measurements. Due to the lack of deeper thermistors, the measurement at 2.4 m was therefore applied down to 5 m.

#### 4.2.4 Saturation and water content images

As Forquet (2009) recommended using Yeh et al. (2002)'s formula (Equation 31) to calculate water content from bulk resistivity it was chosen in this study as well. The linear form is of the equation applied here is:

$$\ln \frac{\rho_a}{\rho_w} = \ln \rho_0 - m \ln \theta \quad \text{Equation 39}$$

where  $\rho_a$  ( $\Omega$  m) is the bulk resistivity from the ERT survey,  $\rho_w$  ( $\Omega$  m) is the pore water resistivity measured by the suction cups,  $\theta$  is the water content and  $\rho_0$  and  $m$  are fitting parameter. Forquet (2011) found the parameters from Yeh's formula to be 0.1153 and 1.908  $\ln \rho_0$  and  $m$  respectively for Moreppen soil and these were adapted here. Due to the fact that Yeh et al. (2002)'s formula assumes constant pore water EC, a modified relationship was used. The fitting parameter  $\ln \rho_0$  is not unitless and hence to achieve this, is divide by  $\ln \rho_w$  and the term as fitting parameter is then recalculated for change in pore water resistivity (Forquet 2011). This recalculation is further referred to as Yeh's formula.

As he also found the fitting parameters for Archie's law (Equation 33) for the Moreppen soil, saturation was also calculated to compare the two results. Archie's law has been verified down to low saturation levels, especially in fine-textured materials. It is well-verified for coarse sand which is of interest in the Moreppen sediments. The linear form of Archie's law for unsaturated porous medium is as follows (Forquet 2011):

$$\ln \frac{\rho_a}{\rho_w} = -m \ln \phi - n \ln S \quad \text{Equation 40}$$

where  $\rho_a$  ( $\Omega$  m) is the bulk resistivity from the ERT survey,  $\rho_w$  ( $\Omega$  m) is the pore water resistivity measured by the suction cups,  $\phi$  is the porosity,  $S$  is the water saturation and  $m$  and  $n$  are fitting parameters. Forquet (2011) found  $m$  and  $n$  to be 0.8793 and 1.8851 respectively.

The values for the fitting parameters here differ slightly from those presented in Forquet (2009) as he refitted these parameters, using the complete dataset rather than in his thesis where he only fitted them to each sample (Forquet 2011). Literature values for these constants are 1.5 and 2.5 for  $m$  and  $n$  in Archie's law and Yeh et al. (2002) obtained a value of 1.336 for  $m$  (Forquet 2011).

The value for porosity is needed to calculated saturation from Archie's law. There are some suggested porosity values for the sediments at Moreppen and they differ slightly. Kitterød (2008) estimated the porosity of the three units at Moreppen using grain size distribution based on Gustafson's analytical equations, where he got a porosity of 0.22 for the top set, 0.23 for the fore set and 0.14 for the silt layer in the fore set unit. Pedersen (1994) estimated porosity in the laboratory from sediment samples from Moreppen, where he found the porosity to range from 0.3 to 0.4. In this project, the value for porosity chosen was 0.35, based on Pedersen (1994)'s study. 0.35 is an average of the values Pedersen (1994) measured from sediment samples close to the lysimeter trench.

Archie's law and Yeh's formula was applied to each grid cell in a profile identical to the area between the two boreholes using the corresponding grid values for bulk resistivity from ERT inversions and pore water resistivity from suction cup data.

Change in saturation (Equation 34) and change in water content were calculated, both using average values for each day. The change was calculated compared to 29<sup>th</sup> of March which is the first day of suction cup measurements during the snow melt period 2010. The benefit of looking at the change in saturation is that porosity is assumed fixed. First images of change in water content and saturation were attempted through using corresponding pixel values to calculate the changes. This did not give satisfactory surf images; thus an average value from change in saturation and water content were calculated for each day. The average bulk resistivity values were estimated using the geometric mean apparent resistivity value for each dataset and the average value for pore water resistivity were obtained from averaging the pixel values from the suction cup data images.

Time-lapse inversions show the change in resistivity at a time of interest with respect to a background dataset. Equation 34 was applied to the pixel values for time-lapse inversions using the suction cup data as pore water resistivity. There are no background data for suction cups prior to snowmelt, hence the dataset from 17<sup>th</sup> of September was used.

## 5. Results and Discussion

### 5.1 Groundwater level and snowmelt infiltration

The responds of the groundwater level and snowmelt is of interest as these are part of what is potentially the signal in the ERT data. It is also of interest when comparing infiltration patterns to previous years. The cumulative snowmelt is calculated based on measured volumes of snow from Moreppen and added precipitation during the period. Snowmelt water equivalent is assumed to equal the amount of infiltrating water equivalent during snowmelt as there is no runoff in the area. Groundwater level responds rapidly to the first snowmelt event in (Figure 9), approximately at 31<sup>st</sup> April. This illustrates the short response time of the system to infiltration through the highly permeable sediments at Moreppen. The significant increase in groundwater level, from 4.94 m depth to 4.56 m, is seen to change in about 20 days, about the same time as the majority of the snowmelt infiltration, which levels off after the 15<sup>th</sup> of April. The cumulative snowmelt is seen to increase quite steady, with a short stagnation between 6<sup>th</sup> and 8<sup>th</sup> of April. The same pattern in rapid response in groundwater level as a consequence of snowmelt was found by French and Binley (2004). Langsholt et al. (1996) found that the sharp increase in groundwater level at Moreppen, initiated after the start of snowmelt periods in 1993-6, lasted for a period 2-3 times longer than the melting period. This is not implied here. This could be due to differences in snow water equivalent. The groundwater recharge in 1994 was about 380 mm (Langsholt et al. 1996) which is quite similar to the snowmelt period in 2001, where the cumulative snowmelt was about 400 (French et al. 2002), and about double water equivalent compared to 2010. The groundwater level change during the snow melt period in 2001 was from 3.3 m to 2.85 m, this is more than in 2010 which is also suggested from the water equivalent infiltration. Jørgensen and Østmo (1990), found that 50% of the groundwater recharge takes place during the snowmelt period. Based on the average annual precipitation of 800 mm in the area; it seems that Jørgensen and Østmo (1990)'s observations were valid also in 2001 and 1994, but not in 2010. The total precipitation for the winter season 2010 was measured to be about 250 mm which is also less than previous years. French (1999) found in previous tracer experiments at Moreppen that the movement of a plume is controlled by the quantity of infiltrating water. This might explain some of the difference discussed later between infiltration measured in 1994, 2001 and 2010.

Uncertainty is present in the cumulative snowmelt calculations as this was measured by various people from day to day, with individual interpretation. The location of measured snow also varied for the different days and could lead to errors due to variation in snow depth within the area of Moreppen.

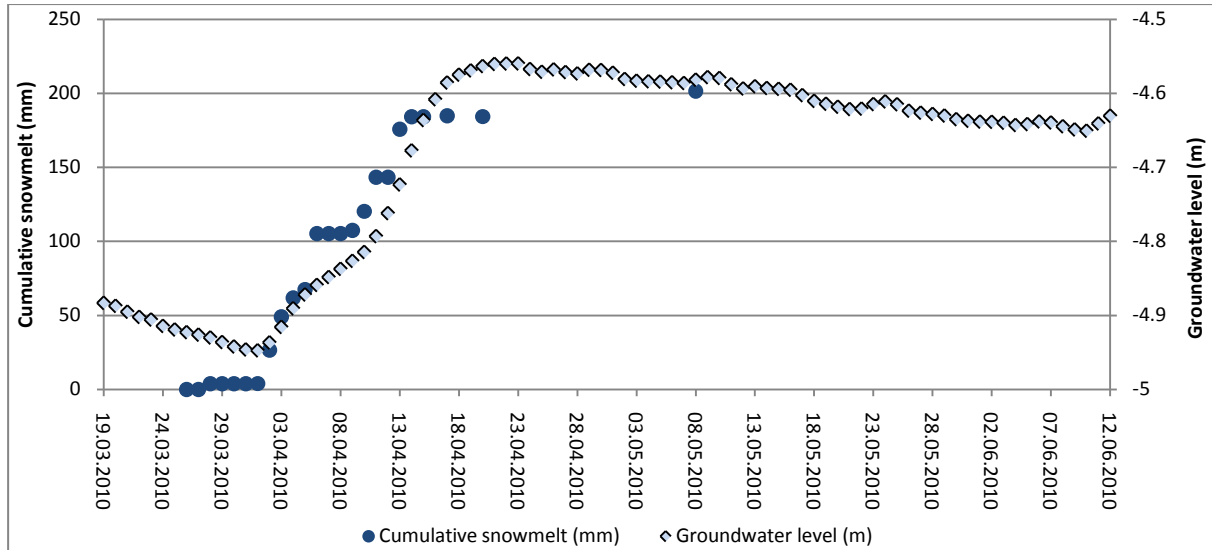


Figure 9: Graph showing the calculated cumulative snowmelt from Moreppen and the measured daily averages groundwater level at Moreppen during the time of interest 2010.

The groundwater is at a profound minimum at the end of the winter season 2010 (Figure 10). Langsholt et al. (1996) found that the groundwater level was at its deepest right before the snowmelt period and this was the case in 2010. The general trend is that the measured groundwater level is shown to be sinking at Moreppen, and these results might either due to drift in the instrument or perhaps due to the artificial lowering of the groundwater in the airport area. The groundwater level appears to be fluctuating during the course of a year, possibly as a consequence of the highly permeable soil where seasonal variations such as autumn rain and snowmelt have a major effect on the groundwater level. There was a drift in the groundwater data recorded and for some time did not work properly during the past few years. Groundwater level during the snowmelt period 2009 and 2008 are lacking; however, the trend visible does not seem to indicate as great a change in groundwater level during earlier snow melt periods as seen during snowmelt 2010. As measured water equivalent snowmelt was higher in 2009, it would also be expected that the groundwater response was greater. This is not seen. The drift was corrected by looking at the previous trend; however, this might be off.

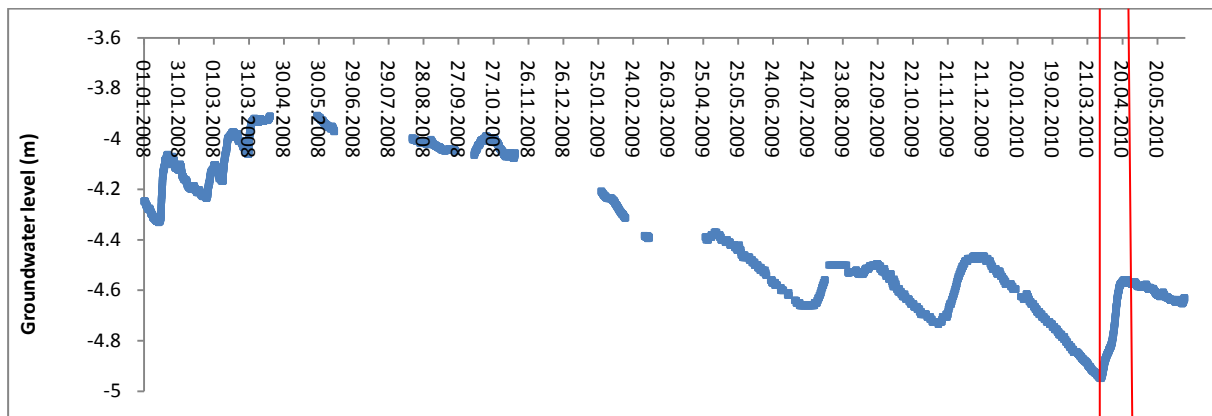


Figure 10: Graph showing the measured hourly groundwater depth at Moreppen during 2008, 2009 and most of 2010. Some data is missing. The two red lines indicate the snowmelt period 2010 in focus here.



## 5.2 Soil and Air Temperature

The tracer experiment at Moreppen started on the 26<sup>th</sup> of March, prior to the snowmelt period. Air temperatures and soil temperatures are of interest to understand the processes in the subsurface during snowmelt. The soil temperatures near the surface seem to be strongly affected by the snow cover in the beginning of the snowmelt period (Figure 11) as stable thermal environments in the soil are seen throughout the period of snow cover (Figure 12). The snow cover insulates the soil from the atmosphere and keeps the soil temperatures stable, compared to the fluctuations seen in the air temperature at the same time (Figure 13). The first day of positive temperatures near the surface of the soil profile is the 14<sup>th</sup> of April (Figure 11) although there are still minus degrees in the soil profile. This correlates with the end of the infiltration of snowmelt (Figure 9). Stable temperatures are seen at the deepest measured point of 2.4 m during the snowmelt period. Propagation of elevated temperatures with depth are observed after the 14<sup>th</sup> of April. Diurnal variations, which are present in the air temperature (Figure 13) seems to have a greater affect on the soil temperature after this date.

The temperature profile for 6<sup>th</sup> of October differs to that seen in the spring. The cooling air temperature during the autumn affects the soil near the surface, compared to deeper in the profile. The highest soil temperature at depth is usually in mid September where the stable thermal environment change is not effected by diurnal air temperature fluctuations. The surface temperature at 5 cm depth show diurnal changes throughout the spring and summer after the snow cover has gone with the highest temperatures measured around July, corresponding more to high air temperatures. Throughout the period monitored, there are great variations both spatially through the profile and in time and illustrates the importance of temperature correction of ERT surveys were the focus is on changes due to infiltration.

The soil temperature variations combined with the stable thermal environment in the profile prior to snow melt is similar to that seen during the snowmelt period 2001 (French & Binley 2004). As the soil temperature for the top 0.4 m until the 14<sup>th</sup> of April were below freezing, the same assumption is made here, as by French and Binley (2004) that the top soil at Moreppen was frozen until the 14<sup>th</sup> of April and that prior to this date the percolation took place through a frozen layer. The ice layer on the ground surface is mostly responsible for the redistribution of melt water and cause preferential flow. It has been found that the typical seasonal soil frost at Moreppen is about 0.4 m deep during the winter season (French et al. 2002). This depth corresponds to the soil temperatures measured in 2010 as well.

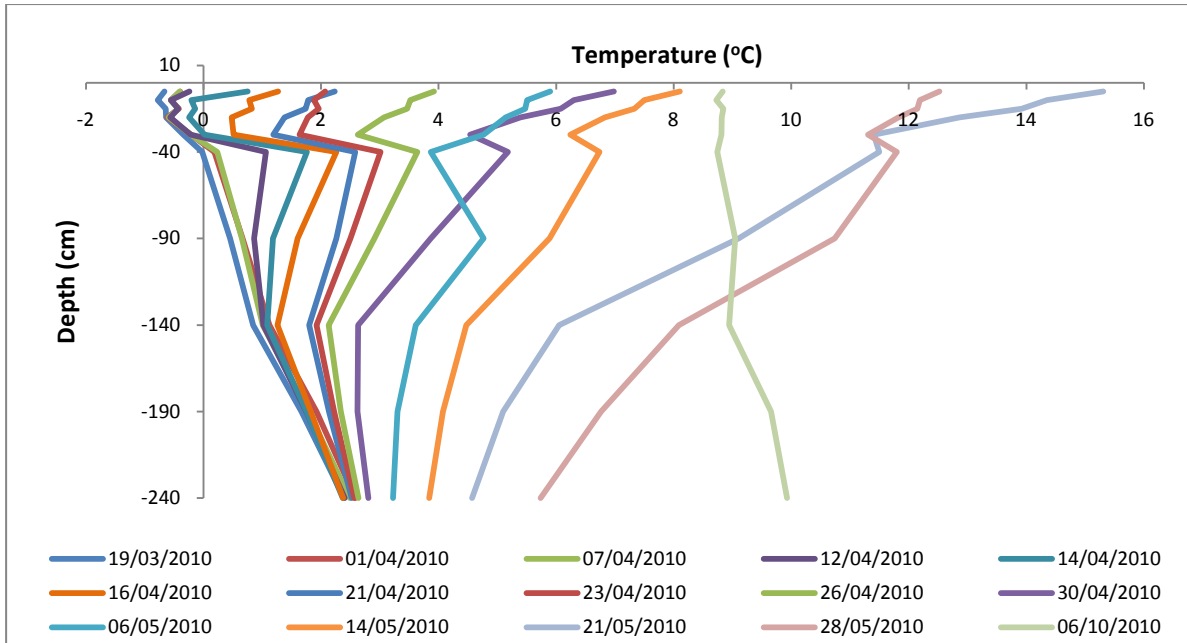


Figure 11: Graph showing the average daily soil temperature with depth measured at Moreppen for some chosen dates during the snowmelt period in 2010, as well as 6<sup>th</sup> of October 2010.

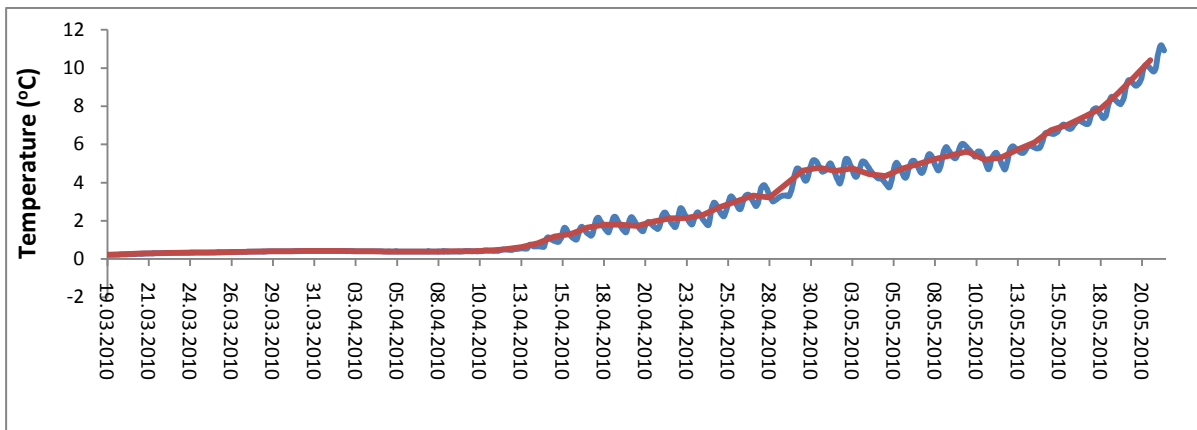


Figure 12: Graph showing the average change in measured soil temperature at Moreppen during the snowmelt period in 2010. Average has been calculated for measurements done at all depth from 0.05 to 2.4 m, where the red line is daily averages and the blue line is hourly averages.

The extent of ground frost depends on the temperature history prior to snowmelt. The air temperature at Moreppen is not as stable as the soil temperature during the snowmelt period 2010 (Figure 13). Periods of thawing and freezing have been discussed to result in the formation of ice lenses under the snow cover and result in preferential flow (Kitterød 2008). From looking at the near surface soil temperatures in 2010 (Figure 13) only two periods of melting and freezing are seen corresponding with the last melting of snow cover during day time 14<sup>th</sup> and 15<sup>th</sup> of April and freezing during the night. Ponding of water and ice lens formation is dependent on repeated temperature fluctuations above and below freezing point during the snowmelt period (Kitterød 2008).

Air temperature has been found to have good correlation with infiltration volume at Moreppen during the snowmelt period in 1994 and 1995 and that air temperature is a key factor for both the melt process of the snow cover and infiltration during snow melt (French

1999). Compared to 1994 at Moreppen, the daily average temperature in 2010 shows the same general increase throughout the snowmelt period (Figure 13). The diurnal fluctuation in air temperature increases during the snowmelt period with some nights with minus degrees. These temperature fluctuations may have resulted in ice lens formation and restructuring of the snow pack during snow melt. Due to the high daily average air temperature on the 20<sup>th</sup> of March, it is likely some reconstruction of the snow pack have occurred prior to snowmelt. However, suggested from the comparison with results from 1994 and 1995, where 1994 had fairly stable and increasing daily average air temperature with little reconstruction of the snow pack and 1995 had huge fluctuations in daily average air temperatures with repeated cycles below freezing; it seems likely that there were less freeze and thaw cycles in 2010, giving less reconstruction of the snow pack and potentially less basal ice formation. The cumulative snow melt (Figure 9) also suggests a fairly even infiltration during 2010.

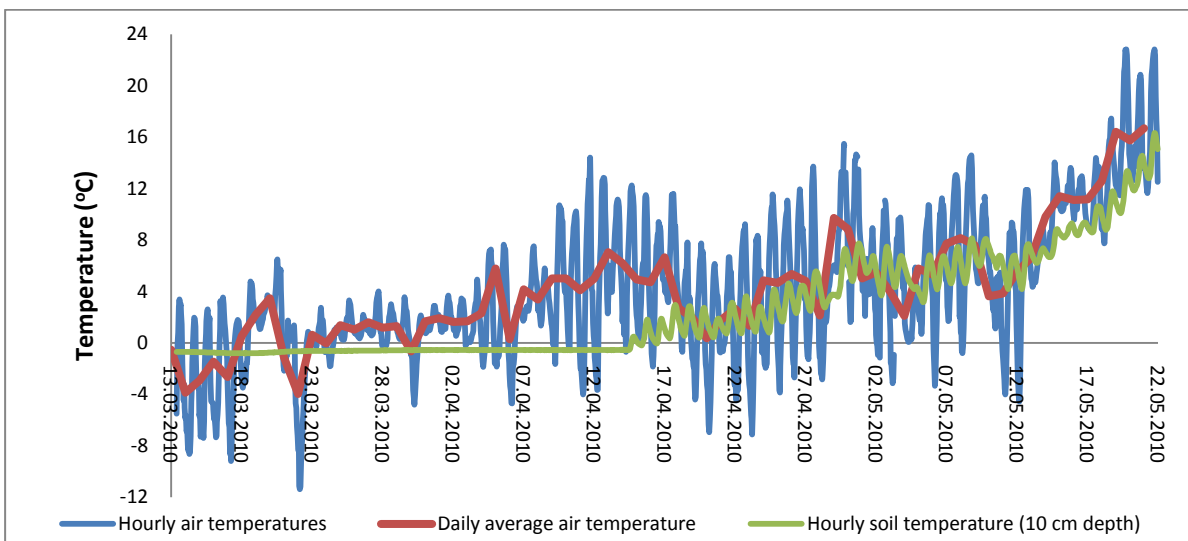


Figure 13: Graph showing the measured hourly and daily average air temperature and hourly measured soil temperature at 10 cm depth at Moreppen in the period 13<sup>th</sup> of March to 21<sup>st</sup> of May.

### 5.3 Interpretation of resistivity data

Two techniques of ERT inversions have been carried out in this thesis and both are discussed in the following section. The individual inversions for the north and south wall can be seen in appendix III and IV. These represent the bulk resistivity measured on a specified date and the final inversions have been temperature corrected. These temperature corrected individual inversions have been used to translate bulk resistivity to water content and saturation using pore water resistivity measured by suction cups in the lysimeter trench. Time-lapse inversions illustrates the change in bulk resistivity between the specified date with respect to a background (here the background used is 26<sup>th</sup> of March 2010). The time-lapse inversions have not been temperature corrected as these inversions are also run based on the raw bulk resistivity data.

#### 5.3.1 Sensitivity plots of the ERT measurements

For a better interpretation of the inversions, sensitivity maps were plotted, following equation 27 both for the time-lapse inversions (Figure 14) and the individual inversions (Figure 15). It is seen from these sensitivity maps that, as expected, the sensitivity is higher closer to the

boreholes and decreases towards the middle of the profile. The sensitivity is lower in the time-lapse inversions compared to the individual once, most likely due to the fact that these are inversions based on the sensitivity of two datasets: the reference dataset and the dataset of interest. Hayley et al. (2010) suggest that the time-lapse ratio method is more sensitivity to data noise and electrode positioning, and could be the reason for lower sensitivity than the individual inversions. The sensitivity seen in the two individual inversions (here chosen 6<sup>th</sup> of October and 22<sup>nd</sup> of March as representative dates after the infiltration and before) is more variable than the maps from the time-lapse, and the sensitivity pattern is less symmetrical. The diagonal artefacts appearing in some of the images are most likely due to bad contact between an electrode and the soil, hence decreasing the sensitivity to all measurements carried out with those electrodes. The reason to use a common dataset and removing the same data points each day was to reduce bias of the sensitivity and remove data points or measurements with electrodes with bad contact and thereby high error. However, it was noticed when looking at sensitivity maps of all the individual inversions that the positions of these low-sensitivity diagonal regions vary for the different datasets, indicating the electrodes with bad contact were not consistent throughout the measuring period. Creating sensitivity plots proved to be useful as an inappropriate mesh for these datasets was noticed.

Sensitivity maps are only qualitative and there are no reference values for “good” data points. However, quantitative sensitivity can be obtained through resolution matrix calculations (Binley 2010) but unfortunately this takes longer and there was not time in this thesis to run these.

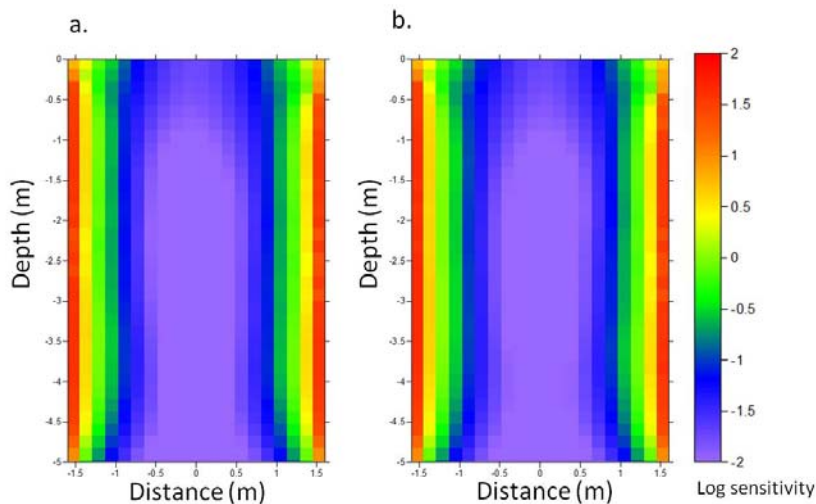


Figure 14: Images showing the sensitivity maps for the soil profile between the boreholes for a) the south wall and b) the north wall for the ERT time lapse inversions for the dataset 26<sup>th</sup> of March 2010 where 22<sup>nd</sup> of March was used as background dataset. The scale is in log sensitivity.

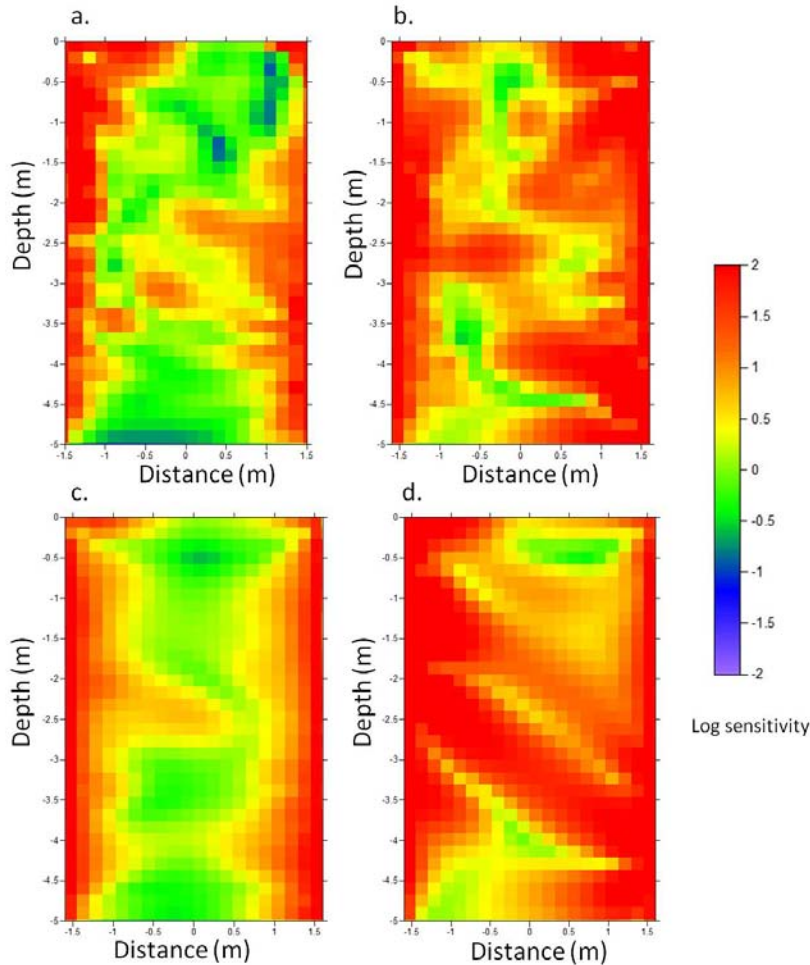


Figure 15: Sensitivity maps of individual inversions for the soil profile between the boreholes for a) 22<sup>nd</sup> of March 2010 south wall b) 22<sup>nd</sup> of March 2010 north wall c) 6<sup>th</sup> of October 2010 south wall and d) 6<sup>th</sup> October 2010 north wall. The scale is in log sensitivity.

### 5.3.2 Comparing ERT measurements to lithology

The individual ERT inversions for the 22<sup>nd</sup> of March 2010 and the 6<sup>th</sup> of October 2010 were compared to the corresponding grain size distribution log from Pedersen (1994) for the south wall (Figure 17) and the north wall (Figure 18). A map of where the logs are collected is seen in appendix II, where the log closest to the north wall is K-18 and south wall K-20. The logs are made based on radiography showing the grain size and lithology. The ERT inversions can also be compared to sketches made of the sediments of the lysimeter trench (Figure 16). It is seen that the logs from Pedersen (1994) vary slightly from the sketches from the lysimeter trench walls.

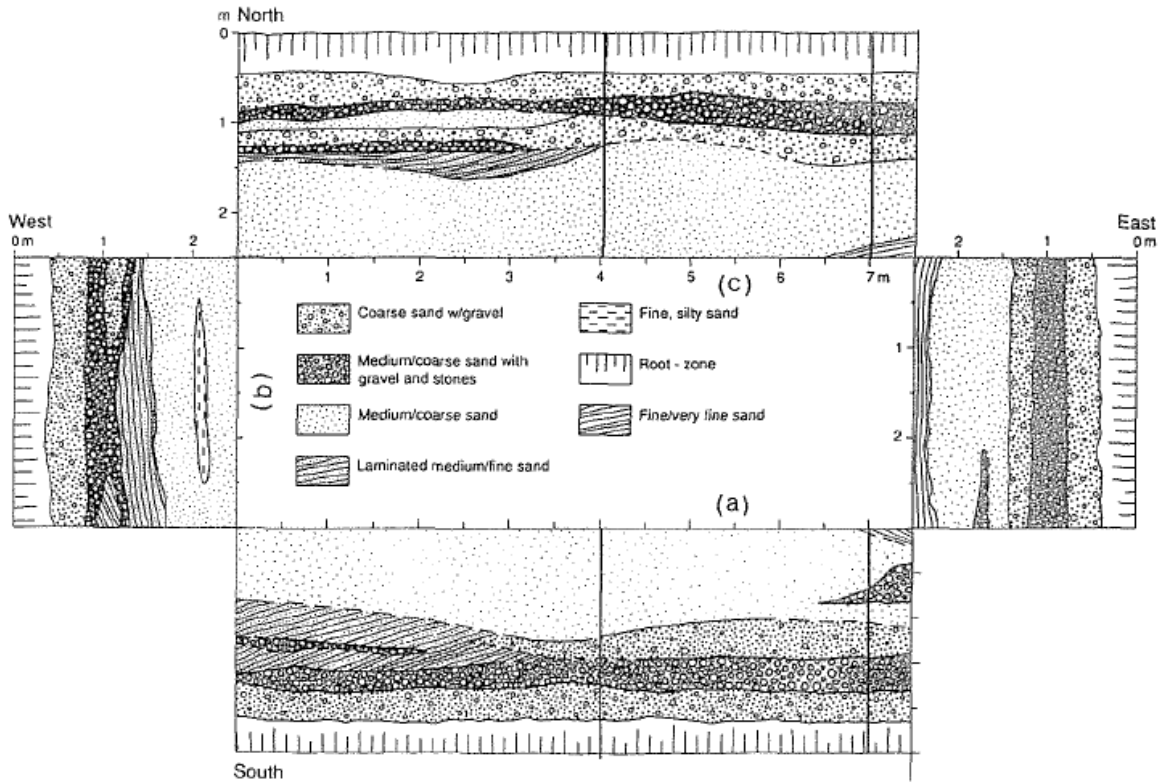


Figure 16: Sketch of the sedimentary layers at Moreppen from the lysimeter trench walls (walls folded out) (French 1999).

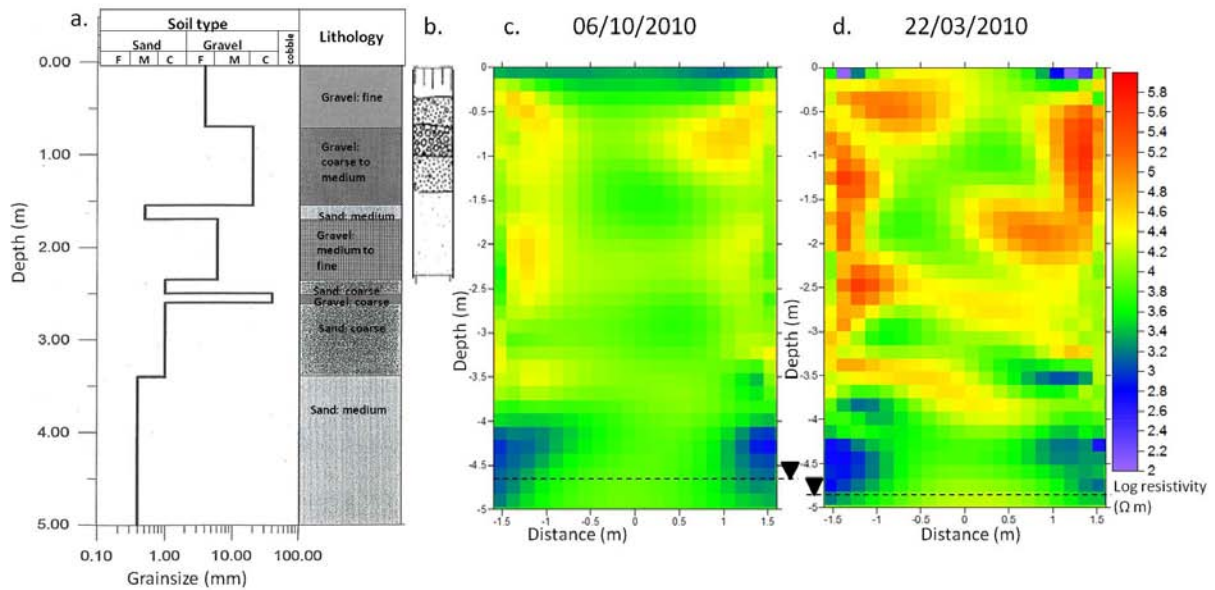


Figure 17: Image showing the a) grain size distribution of soil sample K-20 modified from Pedersen (1994) and b) section from sketch in figure 16 compared to the ERT images from the south wall of the lysimeter trench on the c) 6<sup>th</sup> of October 2010 and d) 22<sup>nd</sup> of March 2010 where the images are the soil profile between the boreholes. In the grain size scale, F= fine, M= medium, C= coarse sand and gravel. After this follows cobble. Location of soil sample is seen in the map in appendix II. Measured groundwater level is indicated on the ERT inversions.



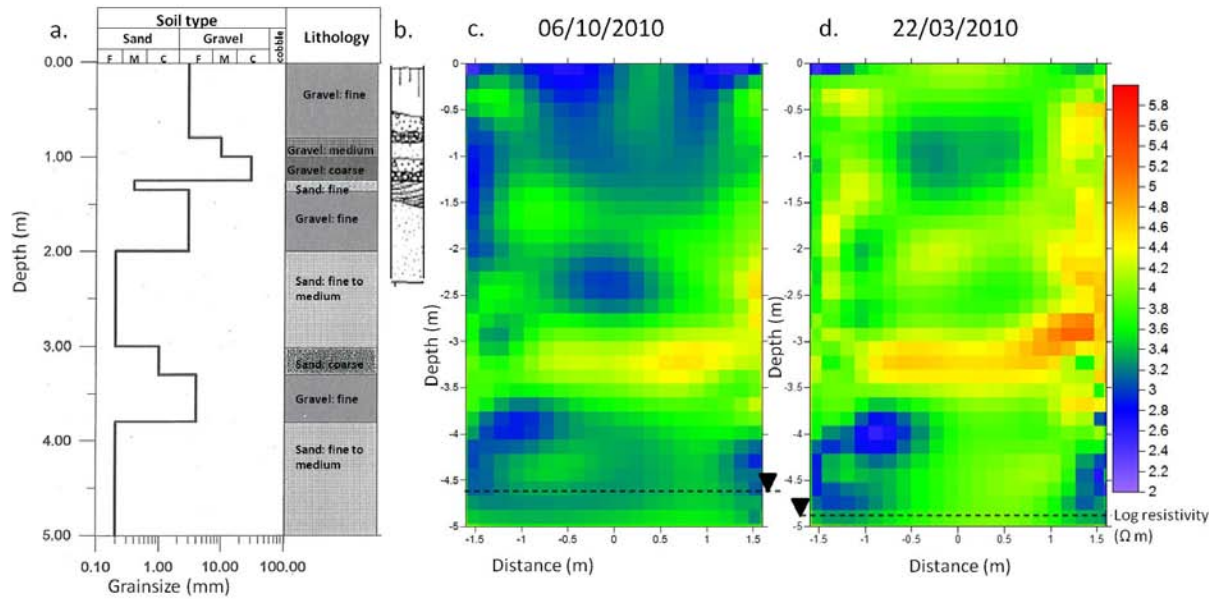


Figure 18: Image showing the a) grain size distribution of soil sample K-20 modified from Pedersen (1994) and b) section from sketch in figure 16 compared to the ERT images from the north wall of the lysimeter trench on the c) 6<sup>th</sup> of October 2010 and d) 22<sup>nd</sup> of March 2010 where the images are the soil profile between the boreholes. In the grain size scale, F= fine, M= medium, C= coarse sand and gravel. After this follows cobble. Location of soil sample is seen in the map in appendix II. Measured groundwater level is indicated on the ERT inversions.

The bulk resistivity is influenced by various factors, such as soil type, moisture content and the porosity. Resistivity decreases with increasing water content and coarse grained sediments have a higher resistivity than fine grained. It is implied from figures 16 and 17 that the south wall has higher resistivity in general than the north wall, and seen from the logs, the south wall seems to contain more layers of coarse grains. The datasets from 6<sup>th</sup> of October appear to have lower resistivity than those of 22<sup>nd</sup> of March. The higher resistivity in March suggest lower moisture content and possibly lower pore water conductivity than in October. The regions of less sensitivity in the measurements mentioned above, is apparent when looking at the expected location of the groundwater level both visible in the south and north wall images. This region of low resistivity of log 2 -3  $\Omega$  m, implied to be the groundwater, is mainly visible to a distance 0.6 m from each borehole. The groundwater appears from the images to be at about 4 m both in October and March. This could potentially be due to the drift in the groundwater logger. The measured depth of groundwater is at 4.9 m on the 22<sup>nd</sup> of March (Figure 9) and at 4.6 m in on the 6<sup>th</sup> of October. The vertical structures close to the sides of the profiles of very high resistivity, log 5 -6  $\Omega$  m, mainly visible in the south wall but also seen in the north wall, are located in the position of the GRP boreholes located within the ERT profile and may possibly explain these high resistivity zones.

The top 0.5 m in both at the north and south wall is a layer rich in organic matter, seen in the trench sketch (Figure 16) and this is implied in the ERT measurements from October were a region of lower resistivity is seen. The higher resistivity in the top of the profiles in March is most likely due to frost. However, this feature is not as dominant as expected.

In the south wall (Figure 17), the October dataset (c) suggests the presence of a high resistivity layer at 0.5 m to 1m, corresponding to that seen in the log (a) of coarse to medium gravel and in the sketch (b), ranging in resistivity from log 4 to 5  $\Omega$  m; however this layer is not visible in the March dataset (c). At 1.5 m there seems to be a thin layer of lower resistivity, about log 3.5-4  $\Omega$  m, corresponding to the layer of sand seen both in the log (a) and the sketch (b). There is also a region of higher resistivity, about log 4.5  $\Omega$  m, at about 2.5 m which might correspond to the layer of medium to fine gravel; however, this structure is seen to vary between datasets. There appears to be a dipping structure at about 3.5 m of coarser material between layers of finer material. This appears in most of the individual inversions.

In the north wall (Figure 18), the ERT data (c and d) suggests a region of lower resistivity, log 2-3.5  $\Omega$  m, for the first 0.7 m, corresponding to the layer of fine gravel. Below this layer down to about 1 m, the dataset from March (d) might identify a part of lower resistivity, log 2.5-3.5  $\Omega$  m, possibly corresponding with the thin sand layer which is also seen in the sketch (b). The two ERT images disagree at a depth of 2 m where low resistivity would be expected to correspond to the thicker sand layer seen in the log and sketch (a and b). There is a very distinct layer of high resistivity, about log 4.5-6  $\Omega$  m, between 3 to 3.5 m in good agreement with the layer of fine gravel shown in the log (a). This is the most dominant feature in the images, suggesting that water content in this layer is possibly lower than in other coarse grained layers.

Hardbatt (2001) and French et al. (2002) found a good agreement between the sedimentary structures from ERT measurements made during the snowmelt 2001 compared to the agreement in the data presented here. However, the boreholes had a smaller spacing and therefore most likely better sensitivity in the region in the centre between the boreholes. Variations in the placement and dipping of structures appearing on the individual inversions might be due to the change in sensitivity between various datasets.

### **5.3.3 Temperature correction**

The initial individual ERT inversions were temperature corrected to 25°C equivalent (Figure 19) to have the same temperature equivalent as the pore water EC from water samples in the suction cups, which are automatically corrected for temperature by the conductivity meter. Hayley et al. (2010) argues that the best method of correcting ERT for temperature is using the raw data and forming temperature correction terms from inversions which are then subtracted from the raw data. Correcting the inversion, rather than the data means possible correcting imperfect inversion resolution. Unfortunately, there was not time in this project to attempt this method. Hence the simpler version published by Hayley et al. (2007) of temperature correction was applied. Hayley et al. (2010) do not comment on the accuracy of either method, but highlights the importance of including temperature in ERT inversions where it is changing over the time of measurement. Without experiments on how the resistivity is affected by temperature on the Moreppen soil, it is hard to quantify the accuracy of the method. As seen from figure 14, there is quite some change in the images going from a) to b) and d) to e). C) and f) are included here to illustrate the data already at 25°C equivalent. The effect of temperature should be removed when attempting to convert ERT inversions to



saturation and water content images. The result is majorly affected if the standard inversion is used rather than the temperature corrected inversion, which might result in wrong estimations of the saturation level and water content present.

Using this simpler version of temperature correction as done here, means that the time-lapse inversions are not temperature corrected, hence part of the change in resistivity seen in the time-lapse inversions are likely due to temperature; especially between the ERT background dataset from October and the snowmelt period. There is not a continuous temperature measurement profile of the soil, only at a discrete number of depths and down to 2.4 m. This is of course a limitation in the temperature correction applied here where these points are used for the whole interval and the measurement at 2.4 m is applied down to 5 m. The constant,  $m$ , from equation 4 is not known for the soil at Moreppen and the value found by Hayley et al. (2007) was used. This might not be applicable.

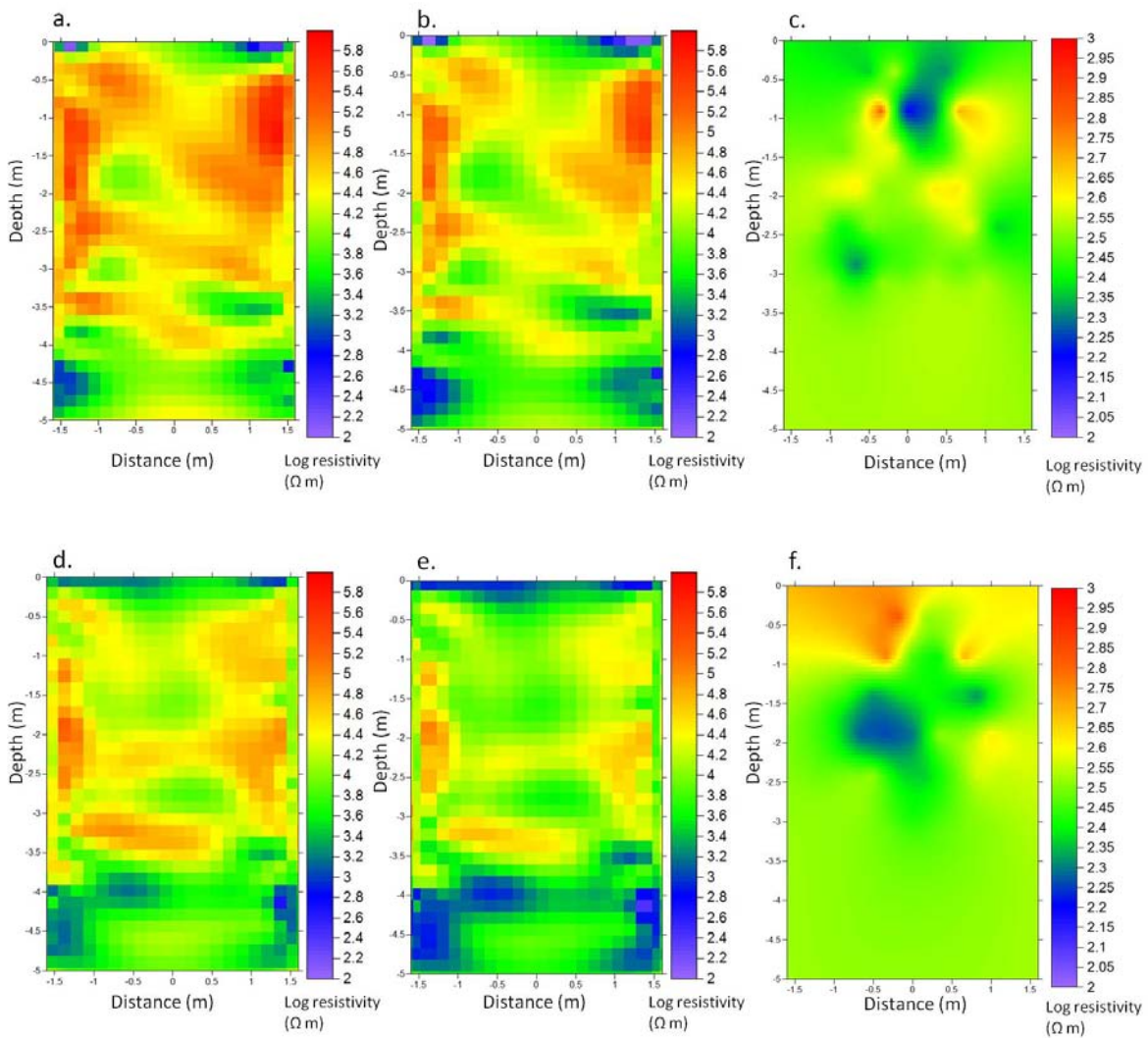


Figure 19: Images illustrating the temperature correction applied to the ERT inversions. Each image shows the profile between the two boreholes where a) is the standard inversion profile from 29<sup>th</sup> of March 2010 b) is the temperature corrected inversion profile from 29<sup>th</sup> of March 2010 and c) is the suction cup data automatically temperature corrected from 29<sup>th</sup> of March d) is the raw ERT dataset from 21<sup>st</sup> of May 2010 e) is the temperature corrected dataset from 21<sup>st</sup> of May 2010 and f) is the suction cup data automatically temperature corrected from 21<sup>st</sup> of May 2010. The images c) and f) are in the log scale 2 to 3.

### 5.3.4 ERT ratio

For a simple quantitative comparison between the individual inversions from the south wall and the north wall, ERT ratios were calculated and temperature corrected. These ratios are calculated using average bulk apparent resistivity given by R2 for the dataset where the ratio shows the difference between 26<sup>th</sup> of March (day of chemical application to the profiles) to the date of interest. Using the average bulk resistivity of the raw apparent resistivity rather than averaging pixel values from the inversions, means the uncertainties from imperfect inversion solutions are not considered. These ratios can be compared to the increase seen in the cumulative snowmelt (Figure 20). The cumulative snowmelt is calculated based on snow water equivalent at Moreppen and precipitation during the period measured at OSL, and also starts on the 26<sup>th</sup> of March.

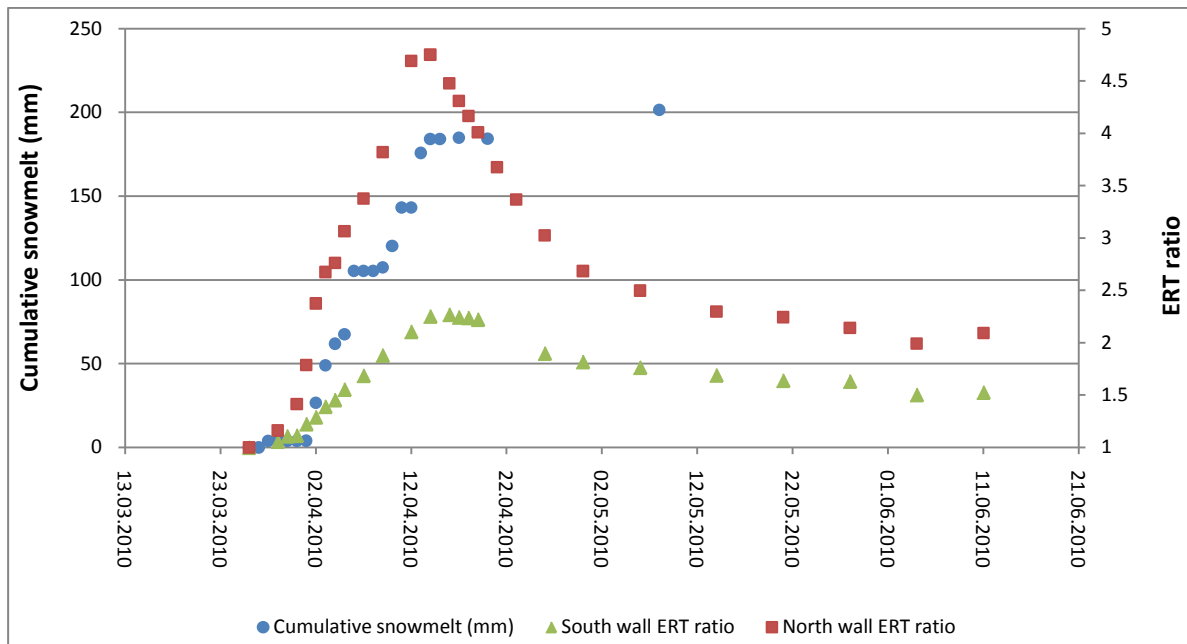


Figure 20: Graph showing the progression of ERT ratio for the south and north wall, together with cumulative snowmelt at Moreppen. 26<sup>th</sup> of March 2010 is used as background date, both for cumulative snowmelt and ERT ratios.

Different de-icing chemicals were applied to the two walls on the 26<sup>th</sup> of March; KFo on the north wall and PG on the south wall. The inactive tracer  $\text{Br}^-$  was applied to both walls. PG does not affect conductivity while both KFo and the tracer  $\text{Br}^-$  does (Bastani et al. 2010). This most likely explains the difference in ERT ratio between the walls where it is seen that the north wall has a far higher increase in ERT ratio than the south wall. The ERT ratios for the south and north wall both show increasing response compared with the trend in cumulative snowmelt. Changes in ERT ratio for both walls start to increase before the most intense snowmelt starts on the 30<sup>th</sup> of March. It has been found that these de-icing chemicals are concentrated in the first flush of infiltrating melt water (French 1999). As the ERT ratio increases prior to snowmelt, it suggests that de-icing chemicals and tracer may cause an early melt which infiltrates the soil and possibly an earlier start of the snowmelt than in the undisturbed area. Studies from OSL have shown that de-icing chemicals have melted out of the snow, even at  $-10\text{ }^\circ\text{C}$  (Øvstedal & Weiden 2007).

The increase in north wall ERT ratio peaks at 4.8 on the 14<sup>th</sup> of April compared to south wall which peaks at 2.3 on the 16<sup>th</sup> of April. The timing corresponds to the last days of snow cover at Moreppen (Figure 13) implying that this is the point of highest infiltration of water and chemicals. The south wall ERT ratio decreases slightly compared to the decrease in the north wall ERT ratio, and then levels off after 16<sup>th</sup> of April while the north wall ERT ratio decreases from 4.8 to 2.3. This difference could indicate degradation of KFo in the soil profile. As the Br<sup>-</sup> tracer does not react with soil and the concentration will remain constant and the infiltration of melt water should be the same at both walls; the difference in signal between the south and north wall is most likely explained by concentrations of KFo. Removing the difference in ERT ratio between the walls should give an indication of KFo. Degradation of de-icing chemicals can cause local regions of reducing conditions which leads to iron and manganese to oxidize; hence decrease the resistivity. This effect might also be seen in the drop in ERT ratio. After snowmelt it has been found that tracer and water is kept at constant depth by capillary forces in the Moreppen soil throughout summer due to evapotranspiration exceeding precipitation. The water and chemicals are pushed further down the profile after autumn rain (French 1999). It is seen in pore water data from suction cups (Figure 23) that the plume of water and tracer stops at one depth and stays here the rest of the measuring period. The trend of levelling off might in ERT ratio after the snowmelt period be caused by this effect. If the difference in ERT ratio between the north and south wall are due to KFo concentrations, then a following decreasing trend during the summer would be expected for the ERT north wall until it reaches the same level as the south wall, assuming similar infiltration patterns and depths of the two walls. Experiments on KAc at Moreppen have shown half lives of between 7 and 50 days with variations due to differences in soil temperature, initial concentration of contaminant and previous contamination history of the soil (French et al. 2002). Potentially, a graph like this can give some indication of degradation of KFo if the effect of it on ERT results is known.

Seen from this, a simple ratio calculation of the mean apparent resistivity measured gives valuable information about the infiltration and possibly the fate of chemicals in the profile. The temperature logger stopped working during June, and is the reason why only these dates are included here. A very simple temperature correction was carried out on the ERT ratios were a temperature average for the whole profile was applied. This is of course a big limitation; however, exclude most of the effect of temperature.

The pore water EC for the north wall was not ready by the time this thesis was written, hence only south wall pore water EC has been looked at in this thesis. As PG does not affect conductivity, the changes in pore water EC is likely due to changes in Br<sup>-</sup> concentrations. Comparing changes in the ERT ratio for the south wall and change in pore water EC (Figure 21) shows less correlation than expected. There are two peaks in change in pore water EC, on the 16<sup>th</sup> of April and the 26<sup>th</sup> of April. The first peak corresponds to the peak in ERT ratio, although not as great increase in change is seen. There is a drop in pore water EC on the 4<sup>th</sup> of April below the initial concentration. This could be due to two measurements of high EC at the bottom of the profile on the 29<sup>th</sup> of March, suggesting left over Br<sup>-</sup> from the previous experiment during the snowmelt 2009. These few high EC spots disappeared by the next

measurement on the 1<sup>st</sup> of April. This can have affected the ratio calculation. However, the ERT ratio also would have measured these “leftover” tracers but is not seen in the ERT ratio calculation. Comparing the change in ERT ratio with pore water EC, the ERT must be mainly affected by increased water content rather than the pore water EC. The conclusion was made by Hardbattle (2001) that Br<sup>-</sup> concentrations account for little of the change seen in ERT measurements from a tracer experiment carried out in 2001 at Moreppen. The effect of piston flow might also be causing this result in the ERT ratio where old water is pushed to further depths by new infiltrating water. The pore water EC only shows the infiltrating tracer while the ERT ratio also measures the movement of piston flow.

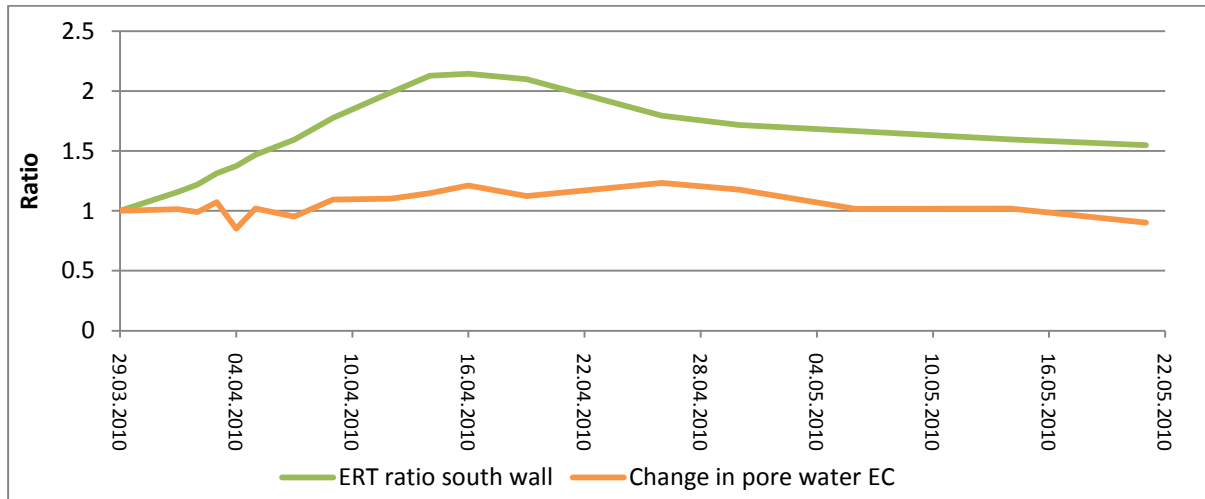


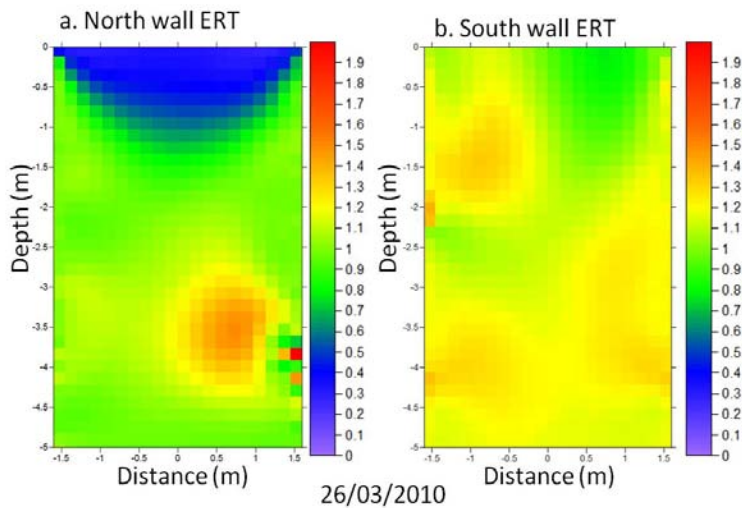
Figure 21: Graph showing change in average ERT measurements (bulk resistivity) and change in suction cup measurements (pore water resistivity). The background dataset used is 29<sup>th</sup> of March 2010.

There are weaknesses in the suction cup data which might cause it to not be as reliable. There are only 38 suction cups, giving few data points compared to ERT measurements. The data was interpolated to give values for all suction cups and this might remove the effect of preferential flow down the profile, as values were calculated for suction cups without samples for each day based on neighbouring cups. This interpolation had to be done due to the fact that not all suction cups collected water every day and some never collected water. There might be limited water available in the soil profile and some suction cups might be damaged or exposed to weathering after being in place in soil for over 15 years. The applied suction by the vacuum pump was set to a fixed value of 0.15 bar, where in 2009 it was set to 0.03 bar (Eggen 2010). Before 2009 it was linked to the tensiometers to vary with the natural suction through the soil profile (Elkin 2011). A low suction should be applied to minimise the effect of on the natural infiltration patterns in the soil. The reason the vacuum pump was set to a fixed suction was due to tensiometers in the profile not working properly. Langsholt et al. (1996) showed that the natural suction at 1 m is around 0.15 bar at Moreppen but lower higher up in the profile. The applied suction might have influenced the natural flow in the top of the profile.

### 5.3.5 Infiltration patterns seen from ERT inversions

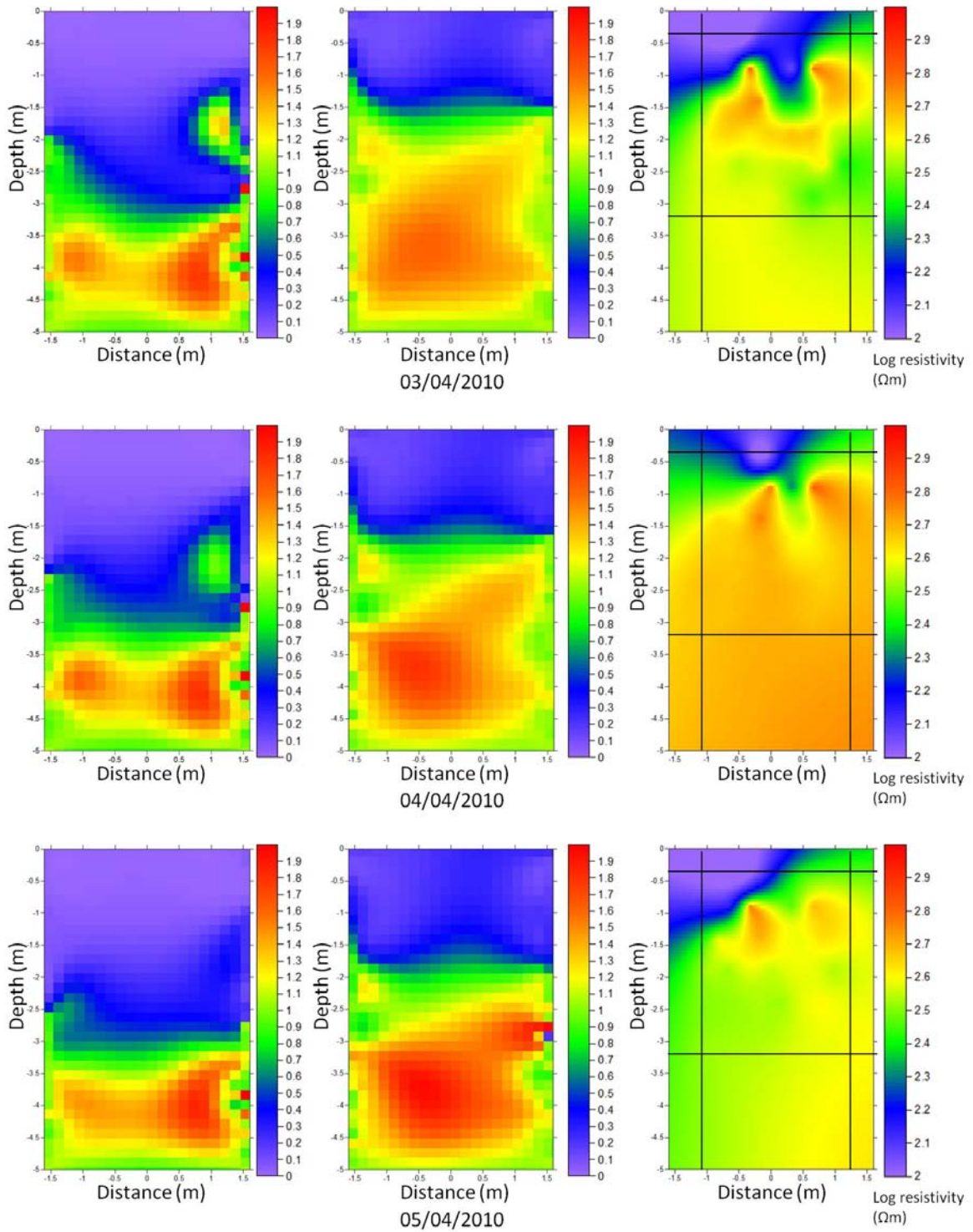
The benefit of time-lapse inversions is that changes which remain constant will not appear, such as sedimentary structures, and the focus will be on changes due to water content, pore

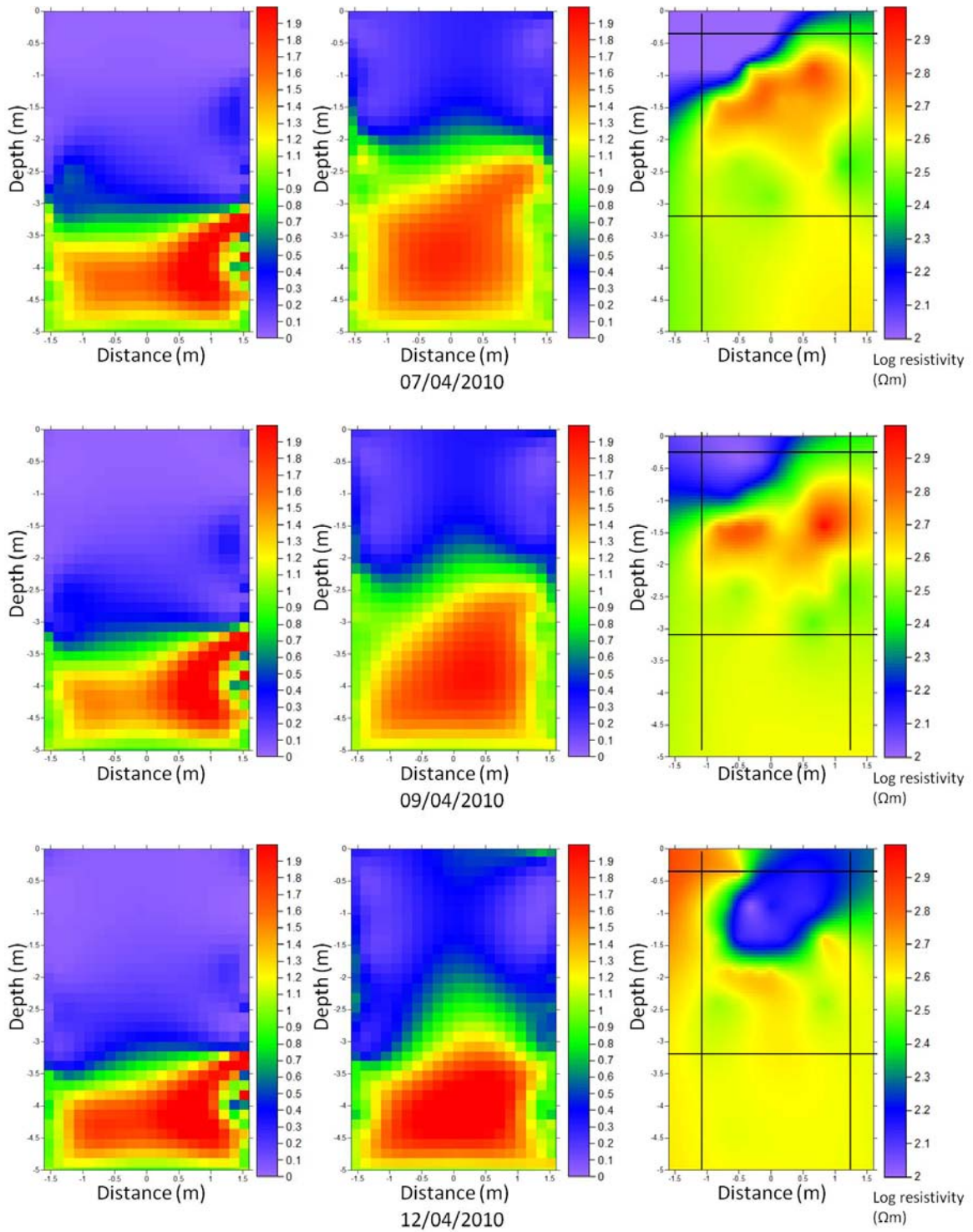
water EC and temperature. Two different background datasets were used for time-lapse inversions during this project, both 22<sup>nd</sup> of March and 6<sup>th</sup> of October. Here only the time-lapse inversions where changes in resistivity against 22<sup>nd</sup> of March are shown (Figure 22). The dataset 6<sup>th</sup> of October was initially used as background dataset since these datasets had less reciprocal errors compared to most datasets from March. However, as the time-lapse inversions are not temperature corrected, much of the change here might be due to temperature. To minimize the effect temperature will have on the time-lapse, the inversions up until the 16<sup>th</sup> of April are shown; where soil temperatures were seen to be fairly stable (Figure 10). The time-lapse inversion for the south wall can be compared to the pore water EC measurements from suction cups. The left column (a) is time-lapse inversions for the south wall, and the middle column is the north wall (b). Both in the scale of change in resistivity where blue indicates decrease in resistivity from 22<sup>nd</sup> of March, green is no change in resistivity and red is increase in resistivity. The right column (c) is the pore water EC from suction cup measurements plotted as log resistivity. The pore water images have a square drawn on to indicate the region of the locations of suction cups in the south wall where the first suction cups are at 0.4 m and the last row at 3.1 m depth. There is also one suction cup at 4.5 m not included in the square on the image. Not all suction cups had water samples each day and these were interpolated to give 38 measurements. The rest of the profile is extrapolated based on the 38 measurements. (Position of suction cups in Appendix I). This highlights the uncertainty involved in the extrapolation of the data to fit the same grid as the ERT data. Some datasets due to poor ERT data have been left out and not all dates coincided with measurements from both ERT and suction cups and those were left out as well.













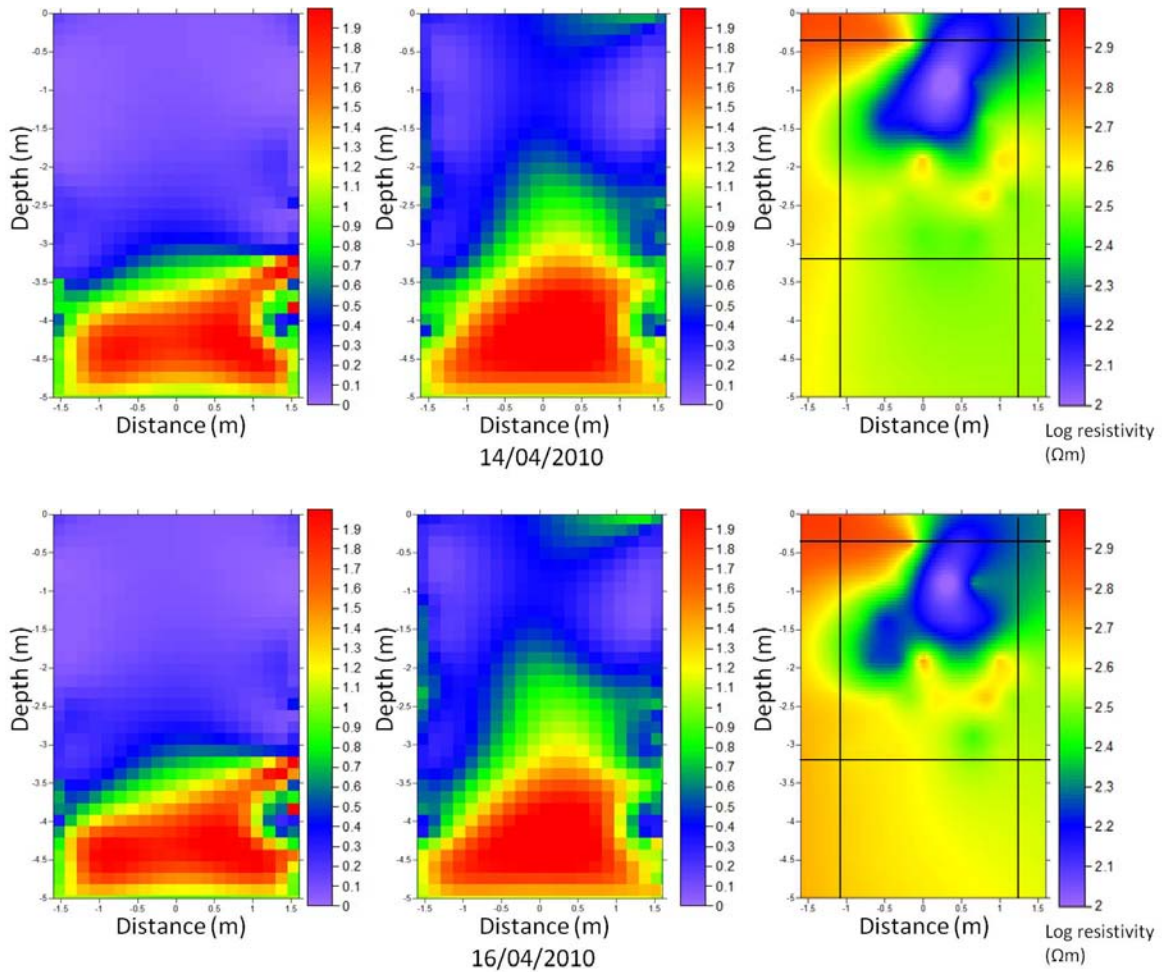


Figure 22: Images of time-lapse inversions for a) the south wall and b) the north wall. The background dataset is the 22<sup>nd</sup> of March, prior to tracer applications. C) is the pore water resistivity interpolated from suction cups from the south wall. The images illustrate the soil profile between the boreholes. The pore water resistivity images have a square indicating the region containing 37 of the 38 suction cups.

### 5.3.5.1 Comparing south wall and north wall time-lapse inversions

Suggested from Figure 19, changes in resistivity will be more visible on the north wall than the south wall during the period of interest, likely due to the application of KFo on the north wall. The time-lapse inversions (Figure 22) for the 26<sup>th</sup> of March are relatively green, implying less change in resistivity between the 22<sup>nd</sup> to the 26<sup>th</sup> of March. A region of decreasing resistivity is visible in the centre of the profile on the 26<sup>th</sup> of March on the north wall profile, suggesting that there is already infiltration taking place by the time the tracer experiment started. From the inversion, it seems the infiltration is already down to 1 m at the centre. French and Binley (2004) found in a previous study at Moreppen that infiltration started before the soil temperature reached above 0°C, which would suggest that fluid water bypasses zones of frozen water. This is suggested from these results as well and due to the fact that no de-icing chemicals were applied in their study, this effect might be larger in this study. Eggen (2010) also found differences in water equivalent snow cover changes between the south wall and north wall during the snowmelt in 2009 at Moreppen. She, however, concluded that with this was most likely due to human measuring error. From the time-lapse inversions it seems that there could be a difference in start time of melt between the two walls. Another explanation could be that the applied de-icing chemicals caused the snow to melt already by the time ERT

measurements were carried out on the 26<sup>th</sup> of March. De-icing chemicals have been found to melt out of snow packs (French 1999) and this could be what is seen here, especially at the north wall. However, 1 m depth seems far for infiltration due to de-icing chemicals on the first day. PG and KFo were applied to the same wall in 2009 as in 2010 and a hypothesis could be that KFo melts out faster from snowpack than PG does.

By the 29<sup>th</sup> of March, a region of decreasing resistivity is also seen in the south wall profile down to 1 m depth and 2 m depth in the north wall profile. Infiltration capacity of soil is known to increase as a consequence of increased water saturation of the soil (Kitterød 2008) and here a possibly early infiltration caused by de-icing chemicals increases the following capacity. The regions of decreasing resistivity, as well as being the new infiltrating water, can also be combined with the effect of piston flow, where new infiltrating water pushes old water down. The groundwater depth is measured to be at 4.9 m on the 30<sup>th</sup> of March (Figure 9). There is a horizontal green layer, indicating no change in resistivity, at the bottom of the north and south inversions on the 1<sup>st</sup> of April which corresponds well to the presence of groundwater. The groundwater is expected to not change much in resistivity and would therefore be expected to appear as green. The regions of decreasing resistivity which is likely to be caused by the infiltrating plume of melt water and chemicals is seen to have moved down the profiles by the 1<sup>st</sup> of April, to 1.5 m in the south wall profile and about 2.5 m in the north wall profile. Eggen (2010) also found differences in the vertical centre of mass of Br between the north and south wall during the snow melt period 2009. She found the vertical centre of mass to be 30-50 cm higher in the south wall profile compared to the north wall profile. From the ERT inversions here, 1 m difference is suggested. However, previous infiltration experiments carried out at Moreppen have not shown any difference in transport between the two walls (French 1999) and it is therefore thought that differences in soil physical parameters between the walls are unlikely. The differences might be due to variations in snow cover and infiltration patterns due to ice formations. The region of decreasing resistivity, which is suggested to be the front of melt water and chemicals infiltrating as well as piston flow, is shown to be closer to purple (0) than the same bluer region discussed in the south wall. This is likely due to the application of KFo at the north wall infiltrating which is conductive in contrast to PG which is not at the south wall.

The region of decreasing resistivity stays at a level of 1.5 m in the south wall profile until the 4<sup>th</sup> of April while in the north wall profile it appears at 3 m by the 4<sup>th</sup> of April and stays at this depth until the 7<sup>th</sup> of April. The region of decreasing resistivity at the north wall seems to be more biased towards the left of the profile compared to the south wall where it is located in the centre. The south wall ERT inversions shows a decreasing resistivity region down to 2 m depth by 7<sup>th</sup> of April and is here seen to be biased towards the two sides of the profile. At both walls the lowest point of the regions of decreasing resistivity are seen to be down to 3.5 m by the 14<sup>th</sup> of April and 4 m by the 16<sup>th</sup>. A small region of green is seen at the top right of the south wall profile on the 14<sup>th</sup> and 16<sup>th</sup> of April, suggesting that the top of the profile is starting to dry up or could be due to the effect of temperature. The region of decreasing resistivity is suggested to be the infiltration of water and conductive chemicals combined with piston flow. The depth suggested by the inversions for stagnation of this front might correspond to the

dominant sedimentary layer appearing to have higher resistivity, at 3 to 3.5 m in the north wall profile and 1.5 to 2 m in the south wall profile. Flow of water might be slower through these layers. Kitterød (2008) found that funnelling of water flow was caused by a low permeability dipping layer. He found that a low permeable dipping layer gave a relative increase in water saturation above the layer and a relative decrease beneath it. Focused infiltration flow has a major impact on the flow velocities as hydraulic conductivities vary non-linear to water saturation. Residence time of water in the unsaturated zone increases with the presence of a low permeable dipping layer. However, he also found that if the first arrival of tracer to the ground water is of interest then this is always faster if there is a dipping low permeable layer in the flow domain. The presence of coarse grained layers might be affecting the water flow in this case. Hillel and Baker (1988) found that a wetting front will not penetrate into a coarse-textured soil from a fine-textured layer until the suction at the interlayer falls to a water entry suction which is characteristic of the sub-layer and this might be explaining what is seen in the inversions.

The groundwater level which is measured to increase from 4.9 m up to 4.6 m over the same period, is neither seen in the inversions for the south nor the north wall. Instead, a region of increasing resistivity is seen to develop in both profiles, pushed down by the moving infiltration plume. This was not expected. Temperature is stable at the deepest measuring point at 2.4 m (Figure 11) therefore it is assumed that the temperature of the groundwater is stable during this time and is not to be the cause of increasing resistivity in this region. One explanation could be that there was leftover tracer, degradation products or associated ions such as iron or manganese, from the previous experiment in 2009 still present on the 22<sup>nd</sup> of March and that this is pushed downwards by the new plume. The presence of left-over tracer and de-icing chemicals are supported by the vertical centre of mass from EC, PG and Br<sup>-</sup> which are all found to be at 2 m on the 29<sup>th</sup> of March and shift to 0.4 m by the 1<sup>st</sup> of April (Eggen 2011). Maybe tracer soluble in the groundwater, or the presence of other ions from previous infiltration experiments have a greater affect on the ERT measurements than the tracer moving through the unsaturated zone.

The time-lapse inversions do not suggest preferential flow through the profile; the infiltration seems to have been a fairly uniform front. There have been several tracer experiments and model simulations at Moreppen, all suggesting preferential flow through the unsaturated zone (e.g. French et al. 1995; French 1999; French et al. 2002; Søvik et al. 2002; Kitterød 2008).

The heterogeneity of snowmelt infiltration which has been seen at Moreppen during previous studies is not visible either. The ERT survey done by French and Binley (2004) study suggested that infiltration during the early stages of snowmelt is localised by microtopography and melt water is thought to be infiltrating through small portions of the surface area. This heterogeneity of infiltrating water is not seen in the inversions. The inversions suggest a front moving across the whole profile, both in the south and north wall. This does correspond to the air and soil temperature (Figure 12 and 13) which suggested few cycles of thawing and freezing than previously seen at Moreppen and could have resulted in more homogeneous infiltration pattern. This is the first time at Moreppen that ERT has been used to monitor infiltration of degrading chemicals which were applied over the entire surface

above the walls of the lysimeter trench instead of a point source. This could be an explanation for seeing a front rather than a plume previously being described. From the individual inversions of the north wall (appendix IV) some preferential flow is suggested. However, it is difficult to draw conclusions based on the individual inversions.

Since the pattern of heterogeneous infiltration and preferential flow were observed in previous experiments, this was expected. The inversions were run with high data weight error (10%) and it is possible that this smoothes the anomalies which would suggest preferential flow. The time-lapse inversions also had data with higher than 10% reciprocal error removed and due to the high percentage of data with high error, some of the inversions are based on less than half the original data due to the background dataset from 22<sup>nd</sup> of March for both walls contained a high number of data with high reciprocal error. The time-lapse inversions would be more accurate with a better quality background dataset as the inversions would be based on more data with less error.

### 5.3.5.2 Comparing ERT time-lapse inversions with pore water EC measurements

In the case of the south wall, the time-lapse inversions can be compared to pore water EC collected by suction cups in the lysimeter trench (Figure 24). The two chemicals applied on the south wall were Br<sup>-</sup> tracer and PG where only Br<sup>-</sup> is conductive; hence changes in resistivity in the pore water collected by the suction cups is thought to be mainly Br<sup>-</sup>. The pore water EC data, given in log resistivity, suggests slight bypass flow in the first day of measurements, 29<sup>th</sup> of March, where lower resistivity of about log 2  $\Omega$  m is seen at two suction cups at 0.9 m. The infiltration suggested in the time-lapse inversion does not show bypass flow. From the suction cup measurements, the plume seems stagnant at 1 m depth until the 9<sup>th</sup> of April, though the lowest resistivity values, of log 2  $\Omega$  m, shift from the right hand side on the 2<sup>nd</sup> of April to the left by the 3<sup>rd</sup> of April and back to the right by the 12<sup>th</sup>. This pattern is not seen in the inversions. Here the infiltration is suggested to be a front moving over the whole profile. The difference might be due to poor sensitivity of the ERT measurements in the middle of the profile or due to the interpolation of the suction cup data. Both ERT and suction cup data show a stagnation of the suggested infiltration for the same duration, although at slightly different depths. This could be due to the limitation of resolution of suction cups or that water travelled slightly further due to piston flow of old water in the profile than the Br<sup>-</sup> tracer picked up by the suction cups. However, Br is thought to not have any retardation in the soil profile (French 1999). By the 12<sup>th</sup> of April low resistivity of log 2  $\Omega$  m is measured by suction cups at 1.4 m and 1.9 m by the 16<sup>th</sup> of April. There seems to be a dilution effect with lower resistivity with depth over time. The difference in depth between the ERT inversion and the suction cup images is supported by the vertical centre of mass calculations of EC, Br<sup>-</sup> and PG. They showed that the Br was transported to a depth of 1.3 m by the 16<sup>th</sup> of April, the end of the snow melt period and levelled off at about 1.5 m after this. The PG vertical centre of mass is at 1.6 m depth by the same date but shows further infiltration down to 2 m by June which is deeper than both the EC and Br<sup>-</sup> vertical centre of mass (Eggen 2011). Water and PG are therefore suggested to be transported further than total EC. The transport of both water and PG might be piston flow of water and left over PG from experiments in 2009.

It was found by French et al. (2002) that the depth interval with largest changes in conductivity was between 0.5 and 1.5 m explained by flushing of tracer through thawing of the surface soils. A more uniform distribution of larger conductivity values were seen near the surface. Here the depth interval with greatest change in resistivity from the beginning of snowmelt is suggested by the ERT inversions to be from the top of the profile down to 1.5 m in the south wall profile and 3 m in the north wall profile. Differences between previous years could also be due to the variations in infiltration patterns and snowmelt each year. The vertical centre of mass for  $\text{Br}^-$  was found to be deeper in 2010 by the end of the snowmelt period at 1.5 m depth (Eggen 2010); however, a bypass flow in 2001 caused the vertical centre of mass to be at 1.6 m depth already half way through the snowmelt period and the resulting vertical centre of mass was at 1 m depth by the end of the snowmelt (French et al. 2002).

### 5.3.6 Quantitative interpretation of the ERT measurements for the south wall

Conversions of ERT images (Figure 23 a) were carried out using Archie's law (Equation 40) to calculate saturation (Figure 23 b) and Yeh's formula (Equation 39) to calculate water content (Figure 23 c) for all the selected datasets from the south wall and can be seen in appendix III and a chosen example is seen in Figure 23. Full saturation is when percentage water content equals porosity; hence the scale of estimated water content (c) is set to 35% as this is the water content at full saturation with the estimated porosity (0.35) used to calculate the saturation level (b). The general trend in these images is that saturation level is estimated to be lower than that equivalent to water content.

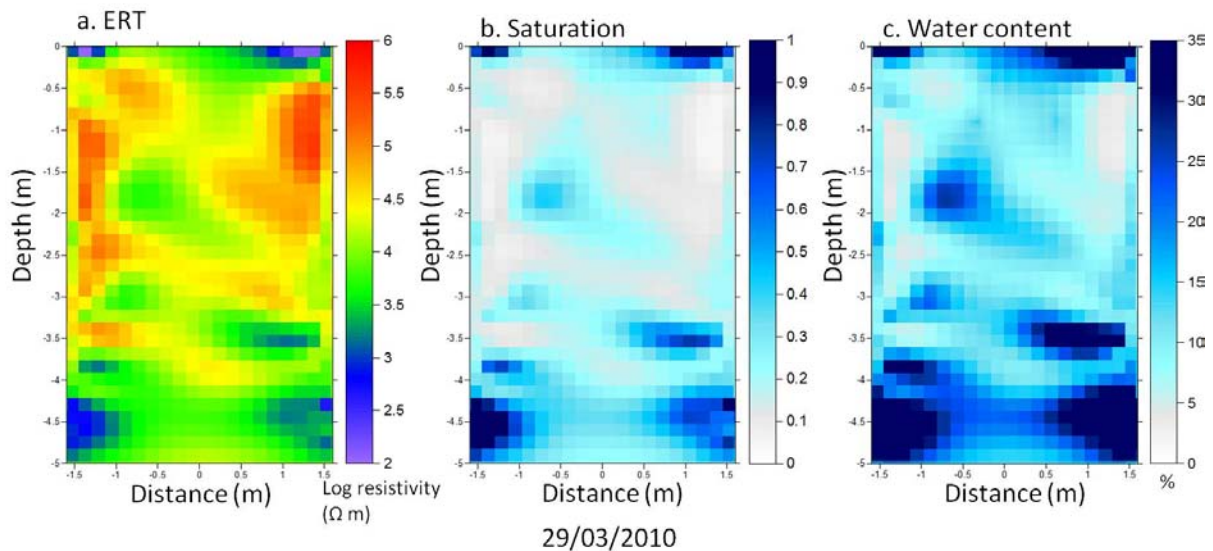


Figure 23: Images illustrating the interpretation of the ERT inversions for the 29th of March 2010 where a) is the ERT inversion in log resistivity scale b) is estimated saturation from 0 to 1 and c) is the water content in percentage.

It is difficult to draw quantitative conclusions based on qualitative images and compare to other measured water contents; hence the estimated water contents calculated from ERT data and pore water EC from suction cups were averaged for depth intervals of 0.5 m from the pixel values of the images. This can be compared to moisture content measured at Moreppen during the snowmelt period in 1994, using a neutron moisture probe (Langsholt et al. 1996)

(Figure 24). In 1994, three neutron moisture probes were used to measure moisture content; here the results from N-12 is included as it is the neutron moisture probe located closest to the lysimeter trench (Seen on map in Appendix II). Neutron moisture probes measure total water content in contrast to TDR were only liquid water in measured. The snowmelt periods in 2010 and 1994 both started in the end of March with the most intensive period during April. The two equations, Archie's law and Yeh's formula, are not parallel, linear relationships and give various results for water content. Yeh's formula (a) seems to be somewhat overestimating water content but shows the same shape as that measured in 1994 (c). Archie's law (b) on the other hand show similar values at the top of the profile while seems to underestimate the water content in the bottom of the profile. The three graphs show similar shapes, where the general shapes of the curves are highest water content in the first 0.5 m and at about 4 m and downwards, likely due to the groundwater. Yeh's formula (a) is more similar to the measured results in 1994 (c) than Archie's law both when comparing regions of highest and lowest water content and dates in which they occur.

Comparing the two estimates for water content in a) and b), the general shapes with relatively high water content at the top 0.5 m is seen in both. However, these measurements are seen to be on different dates, where 37% is seen in a) to be on the 14<sup>th</sup> of April which is the last day of snow, while 40% in b) is on the 1<sup>st</sup> of April which is early in the snowmelt period. The lowest water content at the top 0.5 m are 21.5% in a) on the 15<sup>th</sup> of May which is after the snowmelt period and 19% in b) on the 7<sup>th</sup> of April. The lowest water content measured in 1994 (c) at the top of the profile is seen to be the 25<sup>th</sup> of March at about 20%, before snowmelt in 1994, corresponding to what is seen in b) in 2010. The highest in 1994 at the top of the profile is 27% on the 28<sup>th</sup> of April.

Both estimated water contents from 2010 a) and b) show an increase in water content again at 4 m, around the location of groundwater; however a) shows a greater increase here than b) from 30% to 47% on the 29<sup>th</sup> of March which is the first day of measurements to the 16<sup>th</sup> of May which is around the last day of snowmelt. In b) the increase in water content increase from 17.5% to 26.5% on the 1<sup>st</sup> of April to the 16<sup>th</sup> of May. This supports the idea of groundwater recharge from the snowmelt, where groundwater level rises during the snowmelt period and increases the average water content estimated in this region. The measured water content in 1994 (c) is seen to stay at about 30% at 5 m depth on all days during the snowmelt period. There is also a drop in water content from 4 to 4.5 m in the estimated 2010 water content data. Both of these observations might be due to the poor resolution in the ERT data at the centre-bottom of the profile and pore water EC data is here only based on one suction cup. Both graphs of estimated water content (a and b) show a drop in estimated water content at 2.5 m and 3.5 m and this might suggest layers which hold less water at 2.5 m and 3.5 m which could correspond to the two layers of coarse gravel (Figure 16). The complexity of the unsaturated flow system through this profile is illustrated by all three data sets. It seems like deeper parts of the profile is wetted before overlying layers.



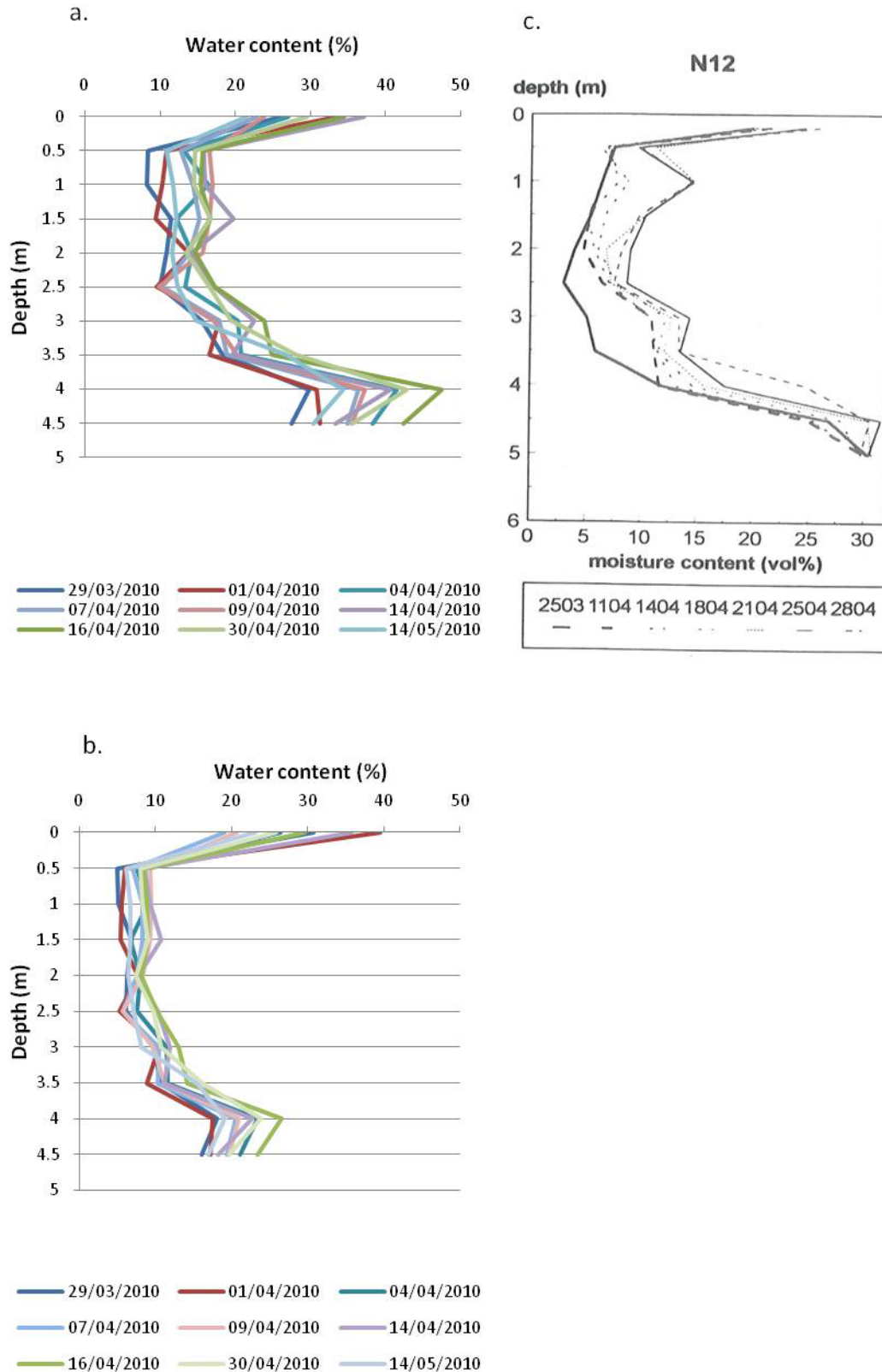


Figure 24: Graph showing a) the estimated water content (%) using Yeh et al. (2002)'s formula (equation 39) b) estimated water content from Archie's law (equation 40), where both a and b are calculated from ERT and pore water EC data with depth (m) of soil profile between boreholes for the snowmelt period 2010. Average pixel values are calculated for intervals of 0.5 m. c) is the measured moisture content by Langsholt et al. (1996) using a neutron moisture probe at Moreppen during the snowmelt period 1994. The location of the neutron moisture probe (N12) can see seen on the map in appendix II.

There are quite some differences in the estimated water content from the two formulas used in a) and b). B) is seen to follow the trend of the measured data from 1994 (c) better than a). The differences between the estimated water content and the measured water content might be due to the generalization involved in averaging pixel values from the images in intervals and possibly due to the temperature correction and the difference between a) and b) is likely due to the uncertainty in estimated porosity used in Archie's law. There are some uncertainties involved in the interpretation calculations carried out for water content using Yeh et al. (2002)'s formula and Archie's law. The constants used in this case were estimated by Forquet (2009) for the soil at Moreppen and were obtained through experimental calibration procedures with variability around the calibration line. Calculating saturation also depends on the value chosen for porosity. Here an average value was used; however, this was shown by Pedersen (1994) to vary for the different sedimentary layers. The formula from Yeh et al. (2002) assumes no change in pore water EC and this is not the case here, hence an adapted form of their formula was used. This might not be appropriate. The ERT data has poor resolution in the middle of the profile as shown by the sensitivity plots which makes the calculations of the data in the centre less reliable than by the boreholes. The smoothing in the inversions will affect sharp boundaries in the sub-surface. The pore water resistivity data is only based on 38 measurements, which have been interpolated for missing data points and extrapolated to the same profile as the ERT data. Forquet (2009) did not specify which temperature he used when finding the fitting parameter for Archie's law and Yeh's formula. The equivalent temperature at which these fitting parameters are measured should have been used. The presence of frozen water in the soil profile might also have an unknown effect on the estimations of water content and saturation.

Using the pixel values to calculate change in water content and saturation did not give satisfactory images; hence the change per day for the whole profile was considered and compared to change in TDR measurements and cumulative snowmelt (Figure 25). Looking at change in saturation removed the uncertainty of porosity. Estimating the change in water content and saturation for the whole profile based on ERT measurements and average pore water resistivity from suction cups involve the limitations of imperfect inversions where each pixel is weighted equally and might not be the case especially for the suction cup data. However, illustrates the general trend in response of the soil system to snowmelt infiltration.



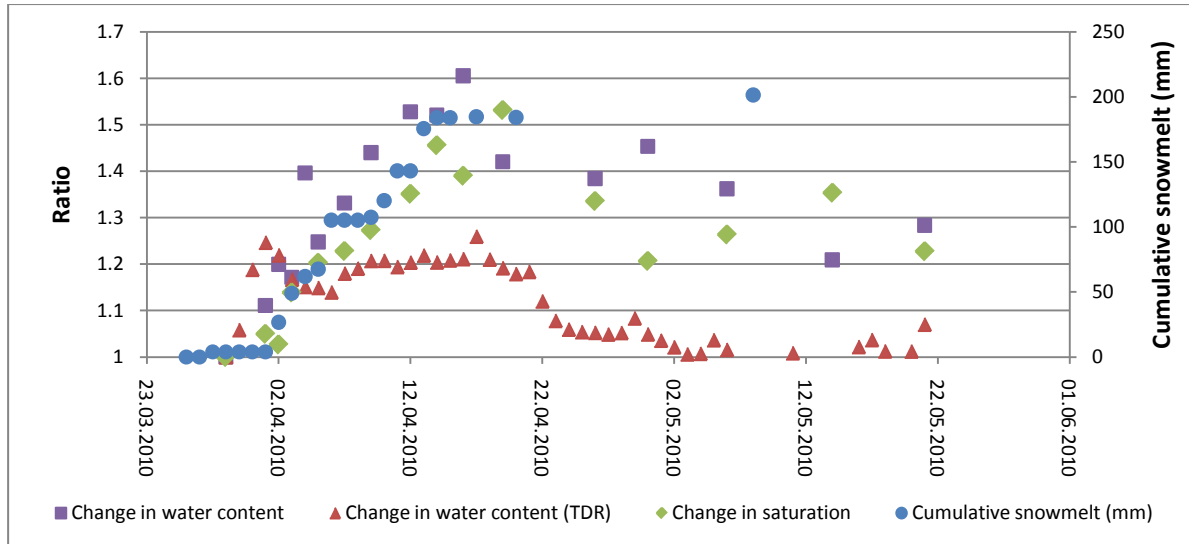


Figure 25: Graph showing calculated cumulative snowmelt (mm), change in saturation and water content estimated from ERT data and pore water EC for the soil profile between the boreholes (0-5 m depth) and change in water content measured by TDR at 30 cm for the south wall. Cumulative snowmelt has start date 26<sup>th</sup> of March 2010 and the changes are compared to 29<sup>th</sup> of March 2010.

The change in water content measured by TDR has been used for the comparison with the estimated water content and saturation, due to the possibility of drift in the TDR data as it has been placed in the field since 2005 (French 2011). Estimated change in saturation is lower than change in water content and this is the trend seen in the converted images and is likely due to limitations within the calculations and fitting parameters. There were no available pore water EC data for the 26<sup>th</sup> of March, hence 29<sup>th</sup> of March is used as background date. This means that changes are calculated compared to the infiltration already taken place by the 29<sup>th</sup> of March. TDR measurements are made with 30 cm long probes. Some of the change in TDR measurements are less than one and hence do not appear in Figure 25. The reason to set the primary y-axis to one is to better compare the data to cumulative snowmelt on the secondary y-axis. However, the same TDR data is seen in Figure 26.

There are noticeable differences between the change in water content measured by TDR and estimates through ERT and pore water EC (Figure 25). Changes in measured water content from TDR are seen to increase before snowmelt up to 1.25 change. As temperature at this depth is measured to be below freezing, change in water content is likely infiltrating water rather than pore water melting. TDR only measure liquid water. The change in estimated water content also increases prior to cumulative snowmelt while change in saturation lags behind but both show a steady increase. Estimated water content peaks on the last day of snow cover on the 16<sup>th</sup> of April at 1.6, while estimated change in saturation drops on this day and peaks later on the 19<sup>th</sup> of April at 1.53. There is a stagnation of cumulative snowmelt between the 6<sup>th</sup> and 9<sup>th</sup> of April but the affect of this is not seen in either the change in saturation or change in water content where a steady increase in change is seen. TDR measurements on the other hand show constant change in water content, at 1.2, after the initial peak on the 1<sup>st</sup> of April. After the snow has melted, both estimated saturation and water content show a general decreasing trend. However, neither estimates drop back to the background level as is seen in the TDR measurements. This is most likely due to TDR only

measuring the top 30 cm of the profile while the estimates are for the whole profile down to 5 m and therefore include the recharge of the groundwater which takes place during the snow melt period.

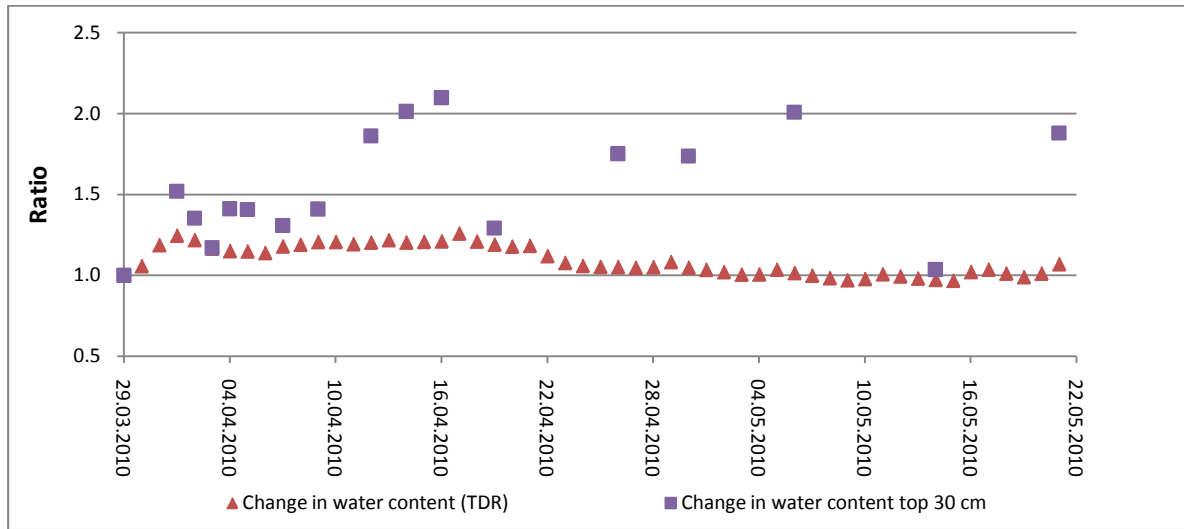


Figure 26: Graph showing change in water content measured with TDR at 30 cm, and estimated change in water content using ERT and pore water EC data from pixel values in the depth 30cm. Changes are compared to 29<sup>th</sup> of March 2010 as background.

The estimated change in water content from ERT data and pore water EC for the top 30 cm have been compared to measured water content at Moreppen from TDR data (Figure 26) to better match the TDR measurements and the estimates at the same depth. The TDR data suggests a fairly stable increase in water content during the snowmelt period, followed by drying of the top soil in late April. The estimated change in water content on the other hand is seen to be more variable. The initial increase at the start of snowmelt is also seen, and there is a general increase towards 16<sup>th</sup> of April, peaking at 2, when all the snow has melted. The estimated water content from ERT and suction cup data shows little correlation with the TDR measurements. One possible explanation is that the chemicals applied to the snow cover can have had an effect on melting of the snow, compared to the TDR readings where no chemicals were applied. However, it might be that averaging pixel values might not be a suitable way of viewing the change in water content at 30 cm, especially considering the fact that the first suction cups are located at 40 cm and extrapolated to this depth.

### 5.3.7 Change in saturation images

The time-lapse inversions shown in figure 22 give resistivity at the specified date with respect to the background date, 22<sup>nd</sup> March. The change in resistivity in these images is a function of water content, solute and temperature. As the soil temperature until the 16<sup>th</sup> of April, is measured to be stable, temperature is thought not influence bulk resistivity and the remaining effect on resistivity is thought to be change in water content and solute. Looking at the change in saturation, the porosity is assumed fixed and the uncertainty from using an estimated porosity value is removed. Porosity is assumed fixed as it is unlikely to change over the measuring period. Using equation 34 the time-lapse inversion pixel values were converted to change in saturation. Pore water EC data from suction cups were not measured prior to the tracer experiment, hence 17<sup>th</sup> of September 2010 was used as background. Due to the many

uncertainties involved in calculating the saturation change based on time-lapse inversions, the images (Figure 27) are shown here as suggestions to be done in the future. However, converting them as shown here will still give an indication of the change in saturation.

The images show change in saturation were green indicate no change between background date and date of interest, red is increase in saturation and blue is decrease in saturation (notice inverse colours compared to Figure 22). The uncertainties involve the fact that the time lapse-inversions are not temperature corrected, and that 17<sup>th</sup> of September was used as background. The pore water conductivity was very low for this date; with measurements of about 4  $\mu\text{S}/\text{cm}$  near the surface. This is far lower than conductivities in March and might explain why the regions seen in Figure 22 to have high pore water EC are calculated to have a decrease in saturation here. The correlation loss of data at regions with low sensitivity is also an uncertainty here making the use of time-lapse inversions less reliable for conversions. Calculating the change in saturation will indicate which changes in ERT data observed are due to water infiltrating and piston flow and which are due to tracer and de-icing chemicals. From figure 27 it is seen that the very distinct front from the time-lapse inversions are not as dominant anymore.

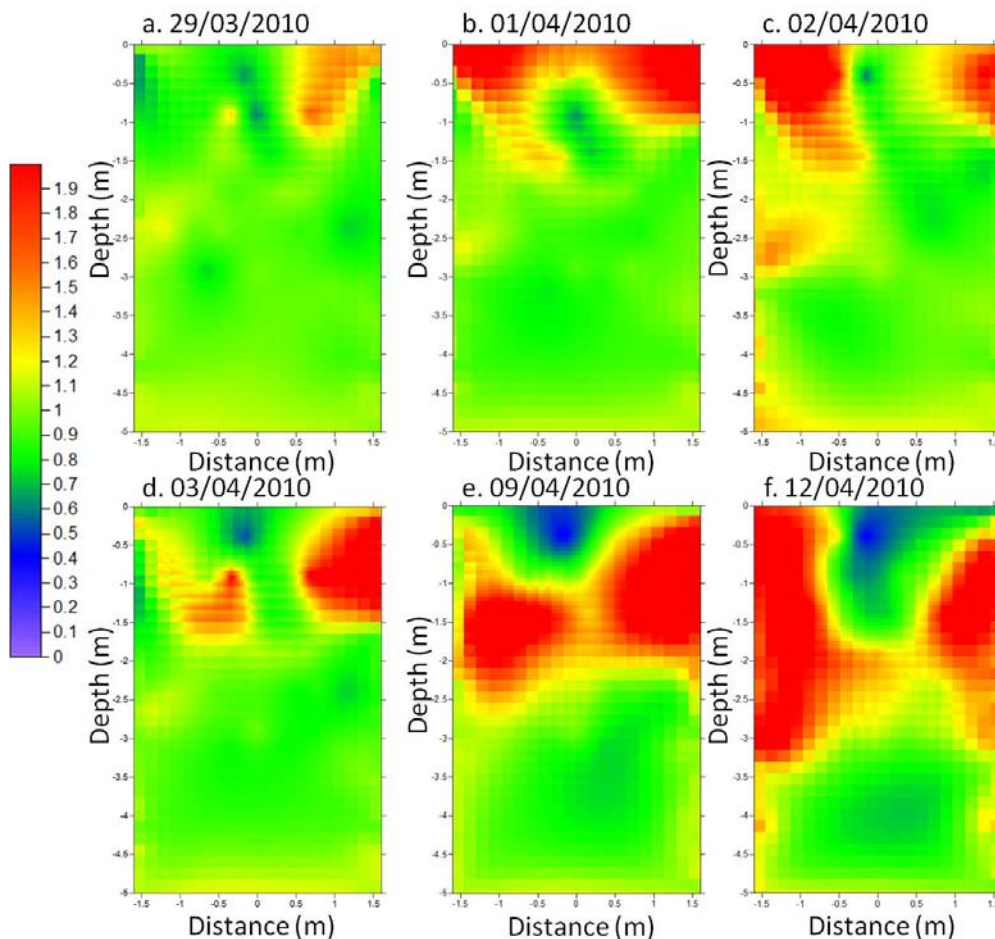


Figure 27: Images showing calculated change in saturation in the soil profile between the boreholes. It is calculated using 22<sup>nd</sup> of March 2010 as background ERT and 17<sup>th</sup> of September 2010 as background for pore water conductivity. Dates are given above figure. The scale is change hence green implies no change, blue is decrease and red is increase in saturation. Notice the inverse colours compared to figure 22.

## 6. Conclusion

In this thesis, cross-borehole ERT surveys have been used to investigate the infiltration of tracer and de-icing chemicals during the snowmelt period 2010. Data was collected from the north and south wall of the lysimeter trench at Moreppen, close to Oslo Airport, Garderomoen, OSL. The ERT inversions were compared to pore water EC measurements from suction cups in the south wall of the lysimeter trench. The individual inversions were temperature corrected and those from the south wall were converted to images of saturation and water content and compared to previous finding at Moreppen to validate the conversions.

There are still challenges using cross-borehole ERT when working with a frozen soil system and these were seen in this study. There was a high noise level in the data, requiring high removal of data points and running the inversions with a high data weight error to allow the inversions to converge. This is most likely due to the weak electrode contact with coarse grained sand and the back-filled sand in the boreholes after construction, especially when the soil is frozen. It also seems that the distance between the boreholes is too great for good resolution of the data in the centre of the profile. Plotting sensitivity maps proved to be helpful to select the most appropriate mesh.

The ERT method is shown to be a helpful method to view infiltration patterns and subsurface structures at a small-scale up to a few meters. The individual inversions showed subsurface structure. The infiltration of melt water and conductive chemicals was clearly seen in the time-lapse inversions, although the method did not show exactly the same patterns as pore water EC measured by suction cups in the lysimeter trench monitoring the same infiltration on the south wall. The depth difference is likely due to resolution differences and to water being transported to depths which are only measured by ERT. Preferential flow patterns in the unsaturated zone and heterogeneous snow melting, as observed in previous experiments were not as clearly visible in the data presented here. Although preferential flow might not be as visible with this method, the topographical difference within the area of OSL is greater and infiltration will be therefore more focused, and from the results presented here ERT has the potential to locate this. There was a clear difference observed in the ERT inversions between the infiltration of PG which is not conductive and KFo which is conductive. ERT surveys might therefore be a more suitable method for monitoring KFo. Simple ratio calculations using average values of bulk resistivity is seen here to have the potential to give valuable information over time. Combining cross-borehole GPR surveys carried out at the same profile using “joint inversions” discussed below in section 7, has the potential to improve the inversions.

Conversions of ERT inversions to water content using Yeh et al. (2002)’s formula seems to give water content estimates within the expected range, although somewhat overestimated. The accuracy of using Archie’s law seems to be limited by the uncertainty of porosity distribution throughout the profile but might yield improved results when looking at the change in saturation when the uncertainty of porosity is removed by assuming porosity does not change over time. As it has been shown here that the water content can be calculated within realistic range of values, these conversions now offers the potential to convert bulk

resistivity from ERT to the change in solute resistivity in the unsaturated zone if combining ERT with water content measurements. This work highlights the importance of temperature corrections to remove the effect of temperature when converting resistivity to water content. The inversions were temperature corrected and the bulk resistivity seems to have been adjusted suitably. Sadly, the accuracy of the correction cannot be commented on from this work.

Cross-borehole ERT survey is shown here to be a suitable method to be used for small scale experiments to look at water and solute transport through the unsaturated zone. The benefit is that cross-borehole ERT survey gives more realistic depth values compared to surface surveys. Depths of subsurface structures are therefore better estimated from this method. Acquisition geometry and survey design vary depending of site conditions and field experiments are therefore important to test these. As the data sensitivity is constrained to the area between the two boreholes, this is perhaps not the most appropriate method for monitoring large areas such as along the runways at OSL but could possibly be used to validate processes on a smaller scale and in combination with point measurements of e.g. water content and pore water electrical conductivity etc. Surface ERT surveying might be more suitable.

## 7. Future work

It seems that the ERT boreholes are too far apart for good resolution in the centre of the profile, compared to earlier findings at Moreppen. The high number of non-reciprocating values in these datasets especially just before the snowmelt could indicate poor contact between the coarse sediments and the electrodes, especially in frozen soil. As seen in the sensitivity plots (Figure 15), the region of most interest at the centre top of the profile has poor resolution. This could be improved by including a row of surface electrodes between the boreholes to better monitor the changes at the surface. Another improvement would be to carry out two measurements each day with different electrode spacing and combining the results. Having smaller electrode spacing would improve the signal-to-noise ratio by the boreholes and larger electrode spacing would improve the resolution in the centre of the profile.

The temperature correction was carried out on inversions rather than the raw data; hence the time-lapse inversions are not temperature corrected. The  $m$ -value used in the temperature corrections were taken from Hayley et al. (2007) and is assumed to be similar for the soil at Moreppen. The  $m$ -value should be found by laboratory experiments with the Moreppen soil for a better temperature correction. In the future, the raw ERT data should be temperature corrected. There are only temperature records down to 2.4 m from the trench. To be able to decrease the uncertainty within the temperature corrections, there should be thermistors at intervals down to 5 m.

There might have been leftover tracer and associated ions with degradation products in the profiles from previous infiltration experiments. To be able to only follow the new infiltration plume, maybe only one wall of the lysimeter trench should be used, swapping between them each year.

In this thesis there was unfortunately not time to run resolution matrices, only qualitative sensitivity plots of the ERT data. Resolution matrix gives quantitative information on the sensitivity of the ERT survey and this could be helpful considering the survey design. Day-Lewis et al. (2005) used resolution matrices to evaluate the correlation loss of data and uses the resolution matrix to up-scale the conversion of inversions to water content at the pixel scale. This approach could be used with the data presented here to improve the conversions to water content and saturation.

For both conversions of ERT data to water saturation and water content, the use of pore water EC from the suction cup data was used. The resolution of this data is quite poor as it is only based on 38 measuring points. To better assess the conversions, especially as the water content formula by Yeh et al. (2002) assume no change in pore water EC, ERT time-lapse measurements should be attempted on infiltration of only water where this assumption is correct. Jayawickreme et al. (2008) used another form of Archie's law:

$$S = \left(\frac{\rho_s}{\rho}\right)^{\frac{1}{m}}$$

Equation 41

where  $S$  is the saturation,  $\rho_s$  ( $\Omega$  m) is the bulk resistivity at 100% saturation,  $\rho$  ( $\Omega$  m) is the measured bulk resistivity at unknown saturation and  $m$  is a constant. Here, the assumption of no change in pore water resistivity is also applied. However, it does remove the effect of possibly varying porosity. A simple laboratory experiment would have to be carried out to find the resistivity at full saturation. Again, the limitation of not being able to monitor the contamination would be present. The potential of this conversion in monitoring contamination is that if the water content is known, it would be possible to estimate the pore water resistivity using the initial form of Archie's law. If the saturation level is known, the only unknown is the pore water resistivity and consequently changes can be investigated. This could be achieved by placing TDR probes horizontally into the lysimeter trenchwall and monitoring the water content of the same infiltration as the ERT, GPR and lysimeter. Leroux and Dahlin (2006) did a simple regression calculation between measured chloride concentration and conductivity of the groundwater and found that 100% increase in chloride caused 34% increase in groundwater conductivity. They concluded a similar relationship was expected in field measurements in sediments with no clay. A similar calculation is possible when the concentration of Br and KFO from the suction cups have been measured. Then it would be possible to estimate change in Br or KFO concentrations based on changes in ERT data, when water content is either assumed fixed or known (e.g. measured).

For more accurate characterization of the subsurface, running joint inversions of different geophysical surveys has been proposed. This can improve the geophysical models and increase their usefulness in hydrogeological studies. (Linde et al. 2006). Geophysical inverse problems have varying resolution throughout the model; however, the variation in the resolution pattern differs for different geophysical techniques (Day-Lewis et al. 2005). Gallardo and Meju (2004) suggested a method of joint inversion of resistivity data and seismic travel time data and found that jointly estimated models gave superior models compared to separate inversions. They found a cross-gradient function between resistivity and velocity by assuming both methods sense the same underlying geology. Seismic data helps develop images of the sub-surface structures such as the sedimentary layers and groundwater level and this could be helpful in case where the ERT inversions shown in this thesis did not show fully the sedimentary structures. This might be improved by combining the inversions with seismic travel time data and changes due to infiltration of water and chemicals would be more apparent. Seismic refraction has not been carried out at Moreppen so this would be an addition to the data collection already in place. Linde et al. (2006) proposes a method of joint inversions of ground penetrating radar (GPR) with ERT data for cross-borehole surveys. GPR cross-borehole surveys are also carried out at Moreppen for the south and north wall of the lysimeter trench and it will therefore be possible to combine these two methods in joint inversions. GPR surveys have best resolution in the centre between the boreholes while ERT surveys have a better resolution close to the boreholes (Day-Lewis et al. 2005).

The TDR probe at Moreppen is possibly drifting due to being placed in the field since 2005. Comparing TDR results and ERT qualitatively and quantitatively has been shown by Koestel et al. (2008) to be effective. TDR probes can also measure EC as well as water content and can therefore be compared directly to the ERT measurements especially when concerning

appropriate data error weighting and indirectly to converted water content values from ERT inversions.



## 8. References

- Aagaard, P. & Breedveld, G. (2008). *Fanprosjektet Gardermoen. Erfaringer og kompetansebygging samt utvikling av kunnskapene om naturbaserte renseløsninger generelt på Gardermoen.:* OSL – 10 års erfaring med utfordringer knyttet til vannkvalitet. Seminar arrangert av Norsk vannforening. Available at: <http://www.tekna.no/ikbViewer/Content/745143/%285%29%20Per%20Aagaard.pdf> (accessed: 10.11.2010).
- Aaltonen, J. (2001). Seasonal resistivity variations in some different swedish soils. *European Journal of Environmental and Engineering Geophysics*, 6: 33-45.
- Appello, C. & Postma, D. (1993). *Geochemistry, groundwater and pollution*. Rotterdam: Balkema. 649 pp.
- Barneveld, R. (2011). *Bioforsk* (Personal communication, e-mail).
- Bastani, M., Kamm, J., Pedersen, L., Godio, A., French, H. K., Bloem, E., Arato, A., Bernard, J., Stocco, S. & Girard, J. (2010). Deliverable 1.3: Multi-method estimates of soil properties. *SoilCAM Project Deliverable*
- Binley, A., Cassiana, G., Middleton, R. & Winship, P. (2002). Vadose zone model parameterisation using cross-borehole radar and resistivity imaging. *Journal of Hydrology*, 267: 147-159.
- Binley, A. & Kemna, A. (2005). DC Resistivity and Induced Polarization Methods. In Rubin, Y. & Hubbard, S. (eds) *Hydrogeophysics*, pp. 129-156. Dordrecht: Springer.
- Binley, A. (2010). *Lancaster University*. Lancaster (Personal communication, e-mail).
- Bloem, E. (2002). *Two- and three-dimensional geo-electrical methods for hydrogeological applications. Environmental study on a leachate plume from a former landfill*. Master Thesis. Delft: Delft University of Technology, Department of Applied Earth Sciences. 101 pp.
- Bloem, E. (2011). *Bioforsk, Soil and Environment*. Ås (Personal communication, in person).
- Campbell, R. B., Bower, C. A. & Richards, L. A. (1948). Change of electrical conductivity with temperature and the relation of osmotic pressure to electrical conductivity and ion concentration for soil extraction. *Soil Science Society of America Proceedings* (13): 66-69.
- Corsi, S. R., Geis, S. W., Loyo-Rosales, J. E. & Rice, C. P. (2006). Aquatic toxicity of nine aircraft deicers and anti-icer formulations and relative toxicity of additive package ingredients alkylphenol ethoxylates and 4,5-methyl-1H-benzotriazoles. *Environmental Scientific Technology*, 40: 7409-7415.
- Dailey, W. D. & Owen, E. (1991). Cross-borehole resistivity tomography. *Geophysics*, 56: 1228-1235.
- Dailey, W. D., Ramirez, A. L., Labrecque, D. J. & Nitao, J. (1992). Electrical resistivity tomography of vadose water movement. *Water Resources Research*, 28: 1429-1442.
- Davie, T. (2003). *Fundamentals of Hydrology*. 2nd ed. London: Routledge. 169 pp.
- Day-Lewis, F. D., Singha, K. & Binley, A. (2005). Applying petrophysical models to radar travel time and electrical resistivity tomograms: Resolution-dependent limitation. *Journal Geophysical Research*, 110: B08206.
- deGroot-Hedlin, C. & Constable, S. C. (1990). Occam's inversion to generate smooth, two-dimensional models from magnetotelluric data. *Geophysics*, 55: 1613-1624.
- Domenico, P. A. & Schwartz, F. W. (1998). *Physical and Chemical Hydrogeology*. 2nd ed. New York: Wiley. 506 pp.
- Eggen, G. (2010). *Transport of deicing chemicals through the unsaturated zone at Moreppen and OSL*. Master Thesis. Ås: Norwegian University of Life Sciences, Institute for Plant and Environmental Sciences. 88 pp.
- Eggen, G. (2011). *Bioforsk, Soil and Environment*. Ås (Personal communication, by e-mail).
- Elkin, K. (2011). *Research fellow; Institute for Plant and Environmental Sciences* (Personal communication, in person).
- Erikstad, L. & Halvorsen, G. (1992). *Områder med nasjonal og internasjonal naturverdi ved Hauer seter-trinnet, Akershus fylke*. Oslo: Norsk institutt for naturforvaltning. 28 pp.
- Evans, W. H. & David, E. J. (1974). Biodegradation of mono-, di-, and tri-ethylene glycols in river waters under controlled laboratory conditions. *Water Research*, 8: 97-100.

- Forquet, N. (2009). *Two-phase flow modelling of vertical flow filters for wastewater treatment*. Ph. D. Thesis. Strasbourg: University of Strasbourg, ENGEES. 152 pp.
- Forquet, N. (2011). *Cemagref, Department of Waste Water Treatment* (Personal communication, e-mail).
- French, H. K., Swensen, B., Englund, J.-O., K.F., M. & Van der Zee, S. E. A. T. M. (1994). A lysimeter trench for reactive pollutant transport studies. In Soveri, J. & Sukko, T. (eds) *Future Groundwater Resources at Risk: Proceedings of an international conference (FGR 94) held at Helsinki, Finland, 13-16 June 1994*, pp. 131-138. Wallingford: IAHS.
- French, H. K., Longsholt, E. & Kitterød, N. O. (1995, March 20-24). *A multi tracer study in the unsaturated zone of a heterogeneous formation*. International symposium on isotopes in water resources management, Vienna, Austria: International Atomic Energy Agency, United Nations Educational, Scientific and cultural Organization.
- French, H. K. (1999). *Transport and degradation of deicing chemicals in a heterogeneous unsaturated soil*. Ph. D Thesis. Ås: Agricultural University of Norway, Department of Soil and Water Sciences. 136 pp.
- French, H. K., Bakken, L. R., Breedveld, G., Hem, L., Kraft, P. I., Roseth, R., Søvik, A. K., Sparrevik, M., Weideborg, M., Zheng, Z., et al. (2000a). *Kjemikaliebruk. Konsekvenser ved bruk av umettet og mettet sone som rensemedium. Rapport A*. Ullensaker: OSL.
- French, H. K., Bakken, L. R., Roseth, R. & Kraft, P. I. (2000b). Nedbrytning av avisningskjemikalier i jord langs rullebane. Teknisk notat 1.2. In French, H. K. (ed.) *Kjemikaliebruk. Konsekvenser ved bruk av umettet og mettet sone som renseanlegg. Rapport B*, p. 75. Ullensaker: OSL.
- French, H. K., Van der Zee, S. E. A. T. M. & Leijnse, A. (2001). Transport and degradation of propyleneglycol and potassium acetate in the unsaturated zone. *Journal of Contaminant Hydrology*, 49 (1-2): 23-48.
- French, H. K., Hardbattelle, C., Bindley, A., Winship, P. & Jakobsen, L. (2002). Monitoring snowmelt induced unsaturated flow and transport using electrical resistivity tomography. *Journal of Hydrology*, 267 (3-4): 273-284.
- French, H. K. & Binley, A. (2004). Snowmelt infiltration: monitoring temporal and spatial variability using time-lapse electrical resistivity. *Journal of Hydrology*, 297: 174-186.
- French, H. K., du Saire, M., Baker, J. & Binley, A. (2006, December 11-15). *Time-lapse Measurements of Electrical Resistivities to Characterise Snowmelt Infiltration Patterns*. Joint Assembly: American Geophysical Union, San Francisco, CA.
- French, H. K., Godio, A., Van der Zee, S. E. A. T. M. & Ghinda, T. (2009a). Deliverable 6.1: Initial meta-data and ceconcept of meta-model. *SoilCAM Project Deliverable*.
- French, H. K., Van der Zee, S. E. A. T. M. & Meju, M. (2009b). SoilCAM: soil contamination: advanced integrated characterisation and time-lapse monitoring. *Reviews in Environmental Science and Biotechnology*, 8: 125-130.
- French, H. K. (2011). *Norwegian University of Life Science, Department of Plant and Environmental Science*. Ås (Personal communication, in person).
- Gallardo, L. & Meju, M. (2004). Joint two-dimensional DC resistivity and seismic travel time inversion with cross-gradient constraints. *Journal of Geophysical Research*, 109: B03311.
- Geo. (2011). *Resistivity Meter*. Ha Noi, Vietnam: Geophysical Technology Joint Stock Company. Available at: <http://www.diavatly.com.vn/index.php> (accessed: 08.05.2011).
- Hardbattelle, C. (2001). *Water and solute transport in a heterogeneous media during snowmelt, Norway*. Master thesis. Lancaster: Lancaster University, Institute of Environmental and Natural Sciences. 71 pp.
- Hartwell, S. I., Jordahl, D. M., Evans, J. E. & May, E. B. (1995). Toxicity of aircraft de-icer and anti-icer solutions to aquatic organisms. *Environmental Toxicology and Chemistry*, 14: 1375-1386.
- Hayley, K., Bentley, L. R., Gharibi, M. & Nightingale, M. (2007). Low temperature dependence of electrical resistivity: Implications for near surface geophysical monitoring. *Geophysical Research Letters*, 34: L18402.
- Hayley, K., Bentley, L. R. & Pidlisecky, A. (2010). Compensating for temperature variations in time-lapse electrical resistivity difference imaging. *Geophysics*, 75 (4): WA51-WA59.
- Hillel, D. (1982). *Introduction to soil physics*. New York: Academic Press. 364 pp.

- Hillel, D. & Baker, R. S. (1988). A descriptive theory of fingering during infiltration into layered soils. *Soil Science Society of America Proceedings*, 146: 51-56.
- Jaesche, P., Totsche, K. U. & Kögel-Knabner, I. (2006). Transport and anaerobic biodegradation of propylene glycol in gravel-rich soil materials. *Contaminant Hydrology*, 85: 271-286.
- Jartun, M. (2011, February 14-15). *Vinterdrift ved Oslo lufthavn- utfordringer for "Vann og grunn"*. Det 20. nasjonale seminar om hydrogeologi og miljøgeokjemi, Trondheim: NGU.
- Jayawickreme, D. H., Van Dam, R. L. & Hyndman, D. W. (2008). Subsurface imaging of vegetation, climate, and root-zone moisture interactions. *Geophysical Research Letters*, 35: L18404.
- Jørgensen, P. & Østmo, S. R. (1990). Hydrology in the Romerike are, southern Norway. *NGU Bulletin*, 418: 19-26.
- Kemna, A., Vanderborght, J., Kulesa, B. & Vereecken, H. (2002). Imaging and characterisation of subsurface solute transport using electrical resistivity tomography (ERT) and equivalent transport models. *Journal of Hydrology*, 267: 125-146.
- Kieft, T. L., Amy, P. S., Brockman, F. J., Fredrickson, J. K., Bjornstad, B. N. & Rosacker, L. L. (1993). Microbial abundance and activities in relation to water potential in the vadose zones of arid and semiarid sites. *Microbial Ecology*, 26: 59-78.
- Kitterød, N. O. (2008). Focused flow in the unsaturated zone after surface ponding of snowmelt. *Cold Regions Science and Technology*, 53: 42-55.
- Klif. (2001). *Ny utslippstillatelse til OSL*. Oslo: Klima- og forurensningsdirektoratet. Available at: <http://www.klif.no/Aktuelt/Nyheter/2001/Oktober/Ny-utslippstillatelse-til-OSL/> (accessed: 27.03.2011).
- Koestel, J., Kemna, A., Javaux, M. & Binley, A. (2008). Quantitative imaging of solute transport in an unsaturated and undisturbed soil monolith with 3-D ERT and TDR. *Water Resources Research*, 44: W12411.
- Labrecque, D. J., Miletto, M., Dailey, W. D., Ramirez, A. L. & Owen, E. (1996). The effects of noise on Occam's inversion of resistivity tomography data. *Geophysics*, 61 (2): 538-548.
- Langsholt, E., Kitterød, N. O. & Gottschalk, L. (1996). The Moreppen I field site: hydrology and water balance. In Aagaard, P. & Tuttle, K. J. (eds) *Protection of groundwater resources against contaminants: Proceedings to the Jens-Olaf Englund seminar 16-18 September 1996, Gardermoen*, pp. 9-37. Oslo: FANE prosjekt Gardermoen.
- Leroux, V. & Dahlin, T. (2006). Time-lapse resistivity investigations for imaging saltwater transport in glaciofluvial deposits. *Environmental Geology*, 49: 347-358.
- Linde, N., Binley, A., Tryggvason, A., Pedersen, L. B. & Revil, A. (2006). Improved hydrogeophysical characterization using joint inversion of cross-borehole electrical resistance and ground-penetrating radar traveltimes. *Water Resources Research*, 42: W12404.
- Liu, S. & Yeh, T. C. J. (2004). An integrative approach for monitoring water movement in the vadose zone. *Vadose zone Journal*, 3: 681-692.
- Llera, F. J., Sato, M., Nakatsuka, K. & Yokoyama, H. (1990). Temperature dependence of the electrical resistivity of water-saturated rocks. *Geophysics*, 55 (5): 576-585.
- Miljøverndepartementet. (1985). *FOR 1985-11-01 nr 1943: Forskrift om vern for Romerike landskapsvernområde, Nannestad og Ullensaker kommuner, Akershus*.
- Miljøverndepartementet. (1999). *FOR 1999-12-17 nr 1424: Forskrift om vern av Elstad som landskapsvernområde, Ullensaker kommune, Akershus*.
- Miller, C. R., Routh, P. S., Brosten, T. R. & McNamara, J. P. (2008). Application of time-lapse ERT imaging to watershed characterization. *Geophysics*, 73 (3): G7-G17.
- Müller, K., Vanderborght, J., Englert, A., Kemna, A., Huisman, J. A., Rings, J. & Vereecken, H. (2010). Imaging and characterization of solute transport during two tracer tests in a shallow aquifer using electrical resistivity tomography and multilevel groundwater samplers. *Water Resources Research*, 46: W03502.
- OSL. (1999). *Miljørapport 1999*. Ullensaker: Oslo Lufthavn Gardermoen. Available at: <http://www.osl.no/osl/omoss/Rapporter> (accessed: 10.11.2010).
- OSL. (2009a). *Miljørapport*. Ullensaker: Oslo Lufthavn Gardermoen. Available at: <http://www.osl.no/osl/omoss/Rapporter> (accessed: 10.11.2010).
- OSL. (2009b). *Årsrapport*. Ullensaker: Oslo Lufthavn Gardermoen. Available at: <http://www.osl.no/osl/omoss/Rapporter> (accessed: 09.11.2010).

- Pedersen, T. S. (1994). *Væsketransport i umettet sone. Stratigrafisk beskrivelse av toppsedimentene på forskningsfeltet, Moreppen og bestemmelse av tilhørende hydrauliske parametre del 1*. Master Thesis. Oslo: University of Oslo. 122 pp.
- Pillard, D. & DuFresne, D. (1999). Toxicity of formulated glycol deicers and ethylene and propylene glycol to *Lactuca sativa*, *Lolium perenne*, *Selenastrum capricornutum*, and *Lemma minor*. *Archives of Environmental Contamination and Toxicology*, 37: 29-35.
- Ramirez, A. L., Dailey, W. D., Binley, A., LaBrecque, D. J. & Roelant, D. (1996). Detection of leaks in underground storage tanks using electrical resistance methods. *Journal of Environmental and Engineering Geophysics*, 1 (3): 189-203.
- Rein, A., Hoffmann, R. & Dietrich, P. (2004). Influence of natural time-dependent variations of electrical conductivity on DC resistivity measurements. *Journal of Hydrology*, 285 (1-4): 215-232.
- Reynolds, J. M. (1997). *An Introduction to Applied and Environmental Geophysics*. Chichester: John Wiley & Sons. 796 pp.
- Samouëlian, A., Cousin, I., Tabbagh, A., Bruand, A. & Richard, G. (2005). Electrical resistivity survey in soil science: a review. *Soil and tillage research*, 83: 173-193.
- Sen, P. N. & Goode, P. A. (1992). Influence of temperature on electrical conductivity on shaly sands. *Geophysics*, 57 (1): 89-96.
- Sørensen, R. (1979). Late Weichselian deglaciation in the Oslofjord area, south Norway. *Boreas*, 8: 241-246.
- Søvik, A. K. & Aagaard, P. (2003). Spatial variability of a solid porous framework with regard to chemical and physical properties. *Geoderma*, 113: 47-76.
- Tuttle, K. J. (1997). *Sedimentological and hydrogeological characterisation of a raised icecontact delta - the Preboreal deltacomplex at Gardermoen, southeastern Norway*. Ph. D. Thesis. Oslo: University of Oslo, Department of Geology, Faculty of Mathematics and Natural Sciences.
- Tuttle, K. J., Østmo, S. R. & Andersen, B. G. (1997). Quantitative study of the distributary braidplain of the Preboreal ice-contact Gardermoen delta complex, southeastern Norway. *Boreas*, 26: 141-156.
- Weideborg, M. (2008). Hvordan bestemme miljøkvaliteten til avsningsvæske og andre kjemikalier. Gjennomføring av miljørisikovurdering som en del av anskaffelsesprosessen for kjemikalier. *Vann*, 43 (4): 361-369.
- Wierenga, P. J. (1977). Solute distribution profiles coupled with steady-state and transient water movement models. *Soil Science Society of America Proceedings*, 41: 1050-1054.
- Winship, P., Binley, A. & Gomez, D. (2006). Flow and transport in the unsaturated Sherwood Sandstone: characterization using cross-borehole geophysical methods. In Barker, R. D. & Tellam, J. H. (eds) vol. 263 *Fluid flow and solute movement in sandstones: the onshore UK Permo-Triassic red bed sequence*, pp. 219-231. London: Geological Society of London.
- Yeh, T. C. J., Liu, S., Glass, R. J., Baker, K., Brainard, J. R., Alumbaugh, D. & Labrecque, D. J. (2002). A geostatistically based inverse model for electrical resistivity survey and its applications to vadose hydrology. *Water Resources Research*, 38 (12): 1278-1291.
- Øvstedal, J. & Weiden, B. (2007, September). *Dispersion of de-icing chemicals to the areas along the runways at Oslo Airport Gardermoen*. 2007 SAE Aircraft and Engine Icing International Conference, Seville, Spain.

## 9. Appendix

**Appendix I:** Table giving the location of the suction cups in the south wall of the lysimeter trench at Moreppen

**Appendix II:** Map showing the Moreppen research station (Langsholt et al. 1996). K-18 and K-20 are the drill core samples analysed by Pedersen (1994) and compared to the ERT inversions. Location of the groundwater well and the climatological station where air temperatures are measured are marked on the map.

**Appendix III:** Figures from south wall where column a) is temperature corrected individual ERT inversions b) estimated saturation and c) is water content

**Appendix IV:** Figures of temperature corrected individual ERT inversion of north wall

## Appendix I

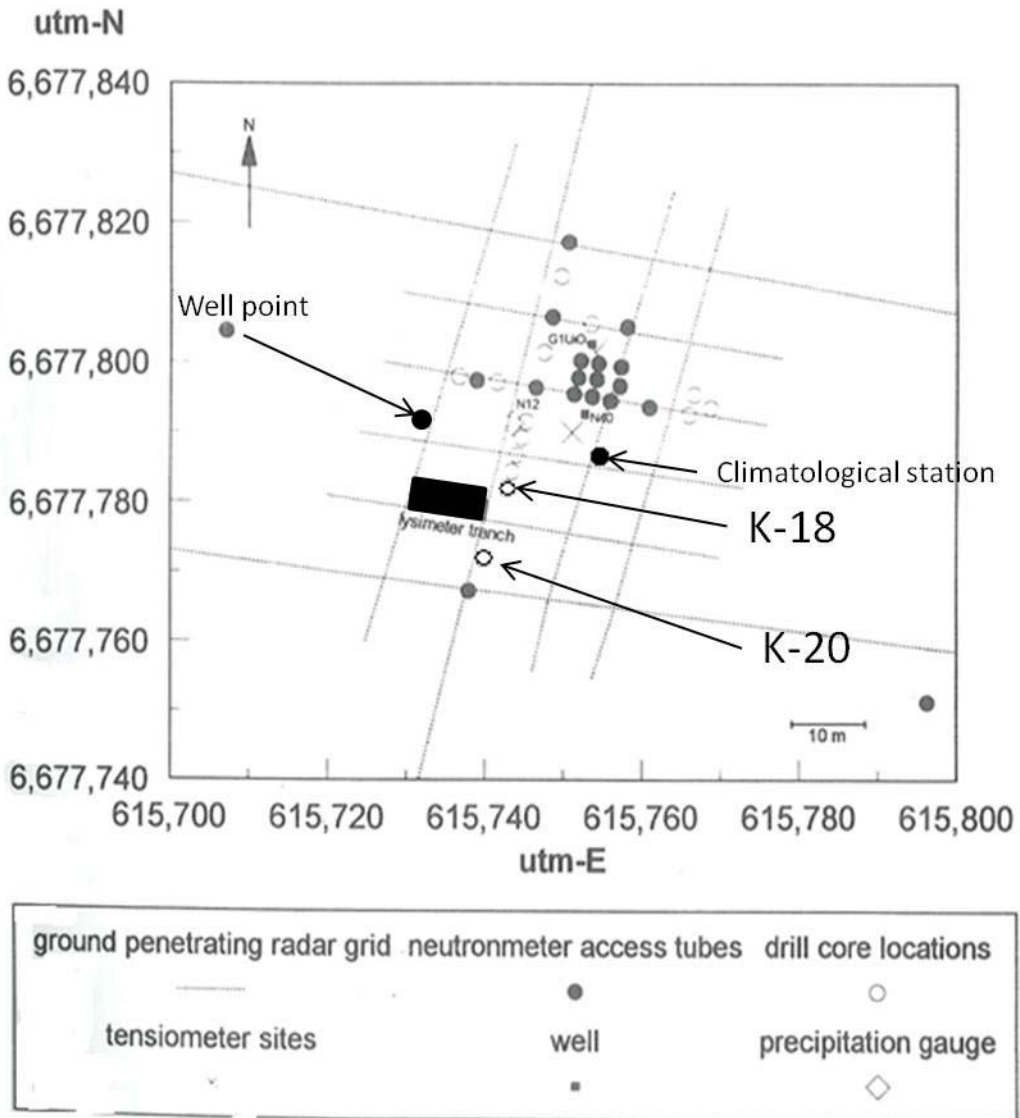
The table gives the coordinates of the suction cups from the lysimeter trench at Moreppen for the south wall. X-coordinates are given as location 0 m being in the centre of the profile.

South wall suction cup location (z and x coordinates):

Suction cup number	Depth (cm)	Location (cm)
1	-40	-49.5
2	-40	-16.5
3	-40	16.5
4	-40	49.5
5	-90	-66
6	-90	-33
7	-90	0
8	-90	33
9	-90	66
10	-140	-82.5
11	-140	-49.5
12	-140	-16.5
13	-140	16.5
14	-140	49.5
15	-140	82.5
16	-190	-99
17	-190	-66
18	-190	-33
19	-190	0
20	-190	33
21	-190	66
22	-190	99
23	-240	-115.5
24	-240	-82.5
25	-240	-49.5
26	-240	-16.5
27	-240	16.5
28	-240	49.5
29	-240	82.5
30	-240	115.5
31	-290	-66
32	-290	0
33	-290	66
34	-310	-99
35	-310	-33
36	-310	33
37	-310	99
38	-450	-66

## Appendix II

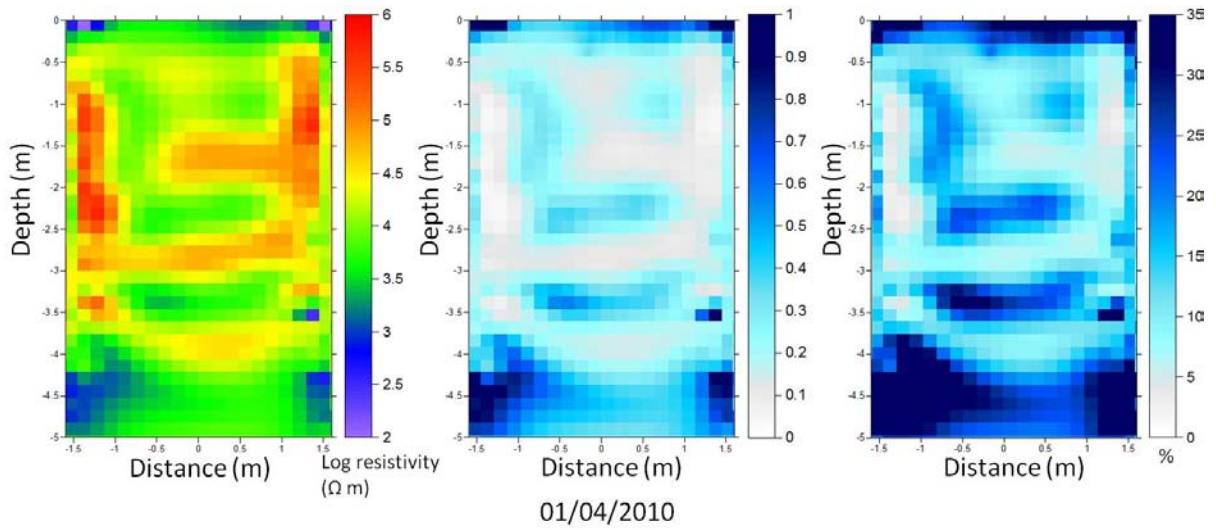
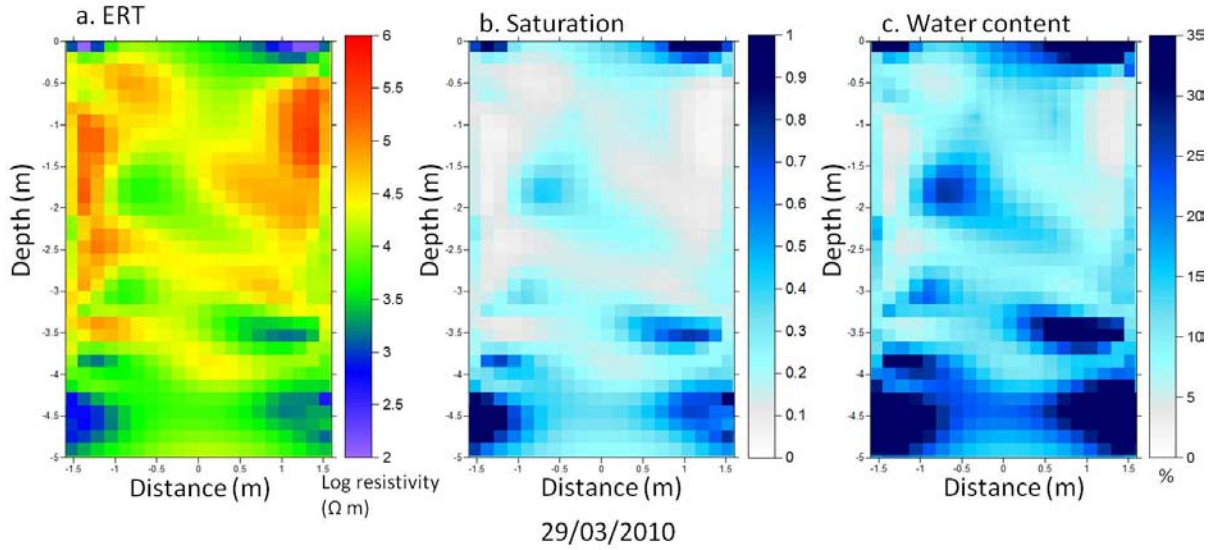
Map showing the Moreppen research station (Langsholt et al. 1996). K-18 and K-20 are the drill core samples analysed by Pedersen (1994) and compared to the ERT inversions. Location of the groundwater well and the climatological station where air temperatures are measured are marked on the map.



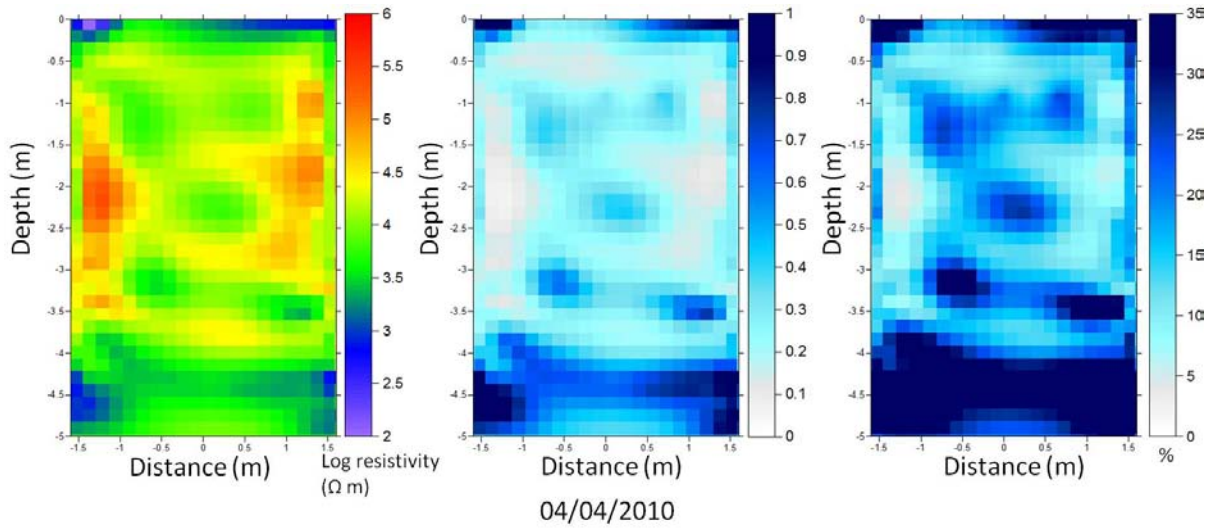
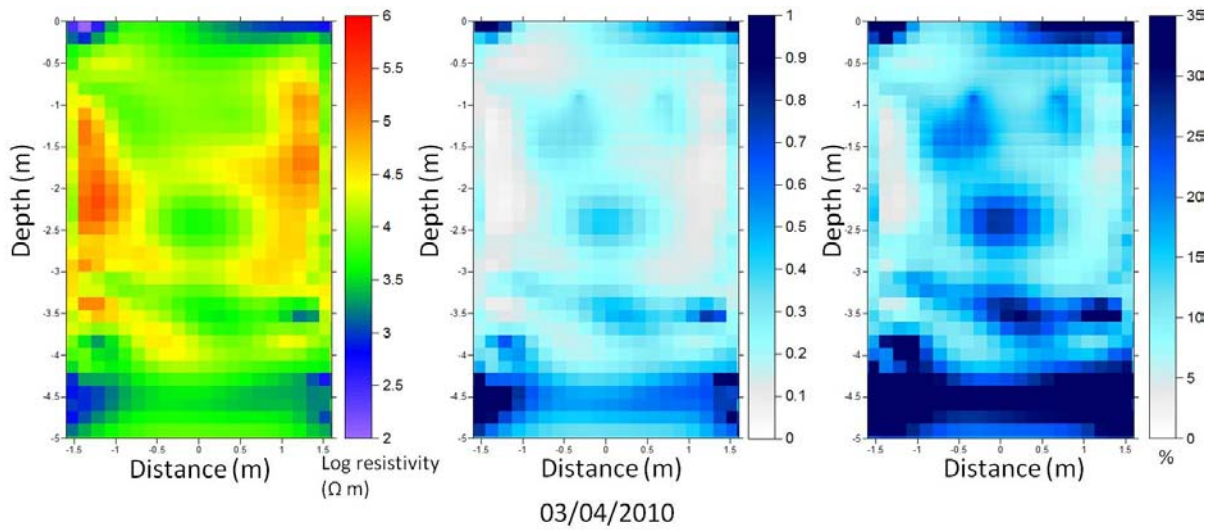
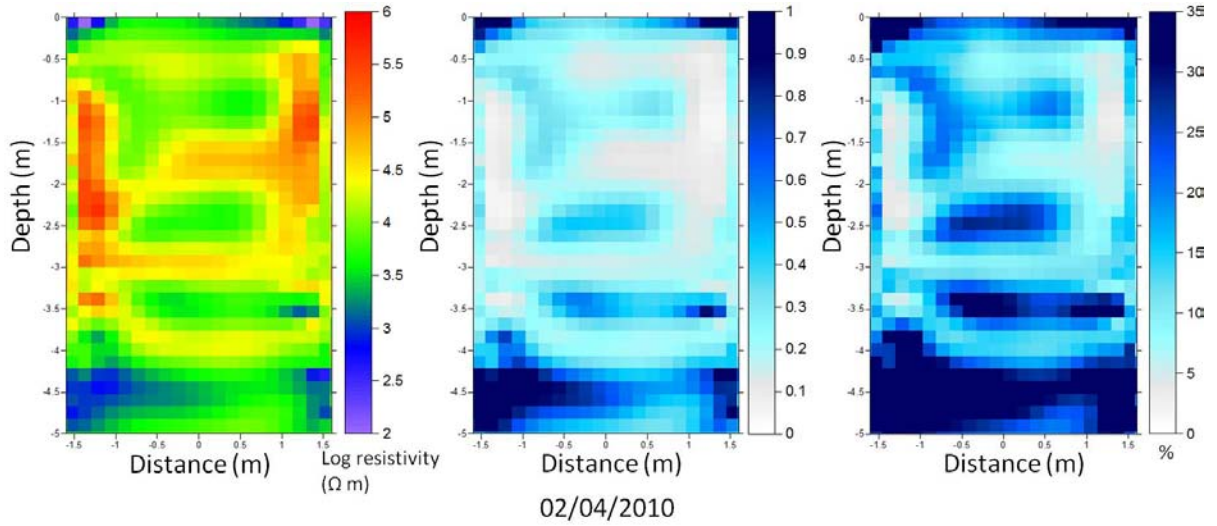


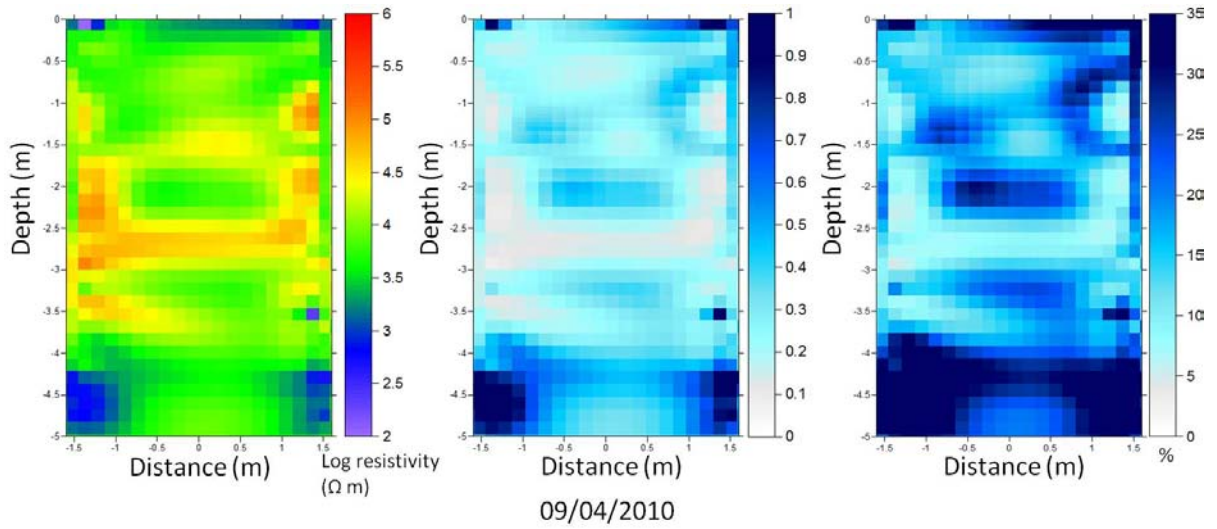
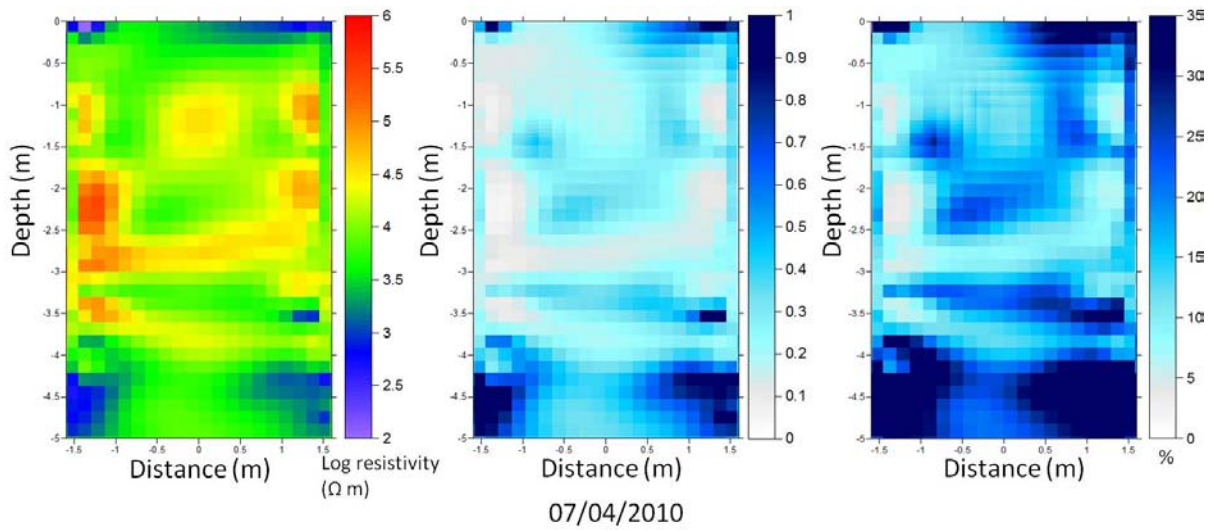
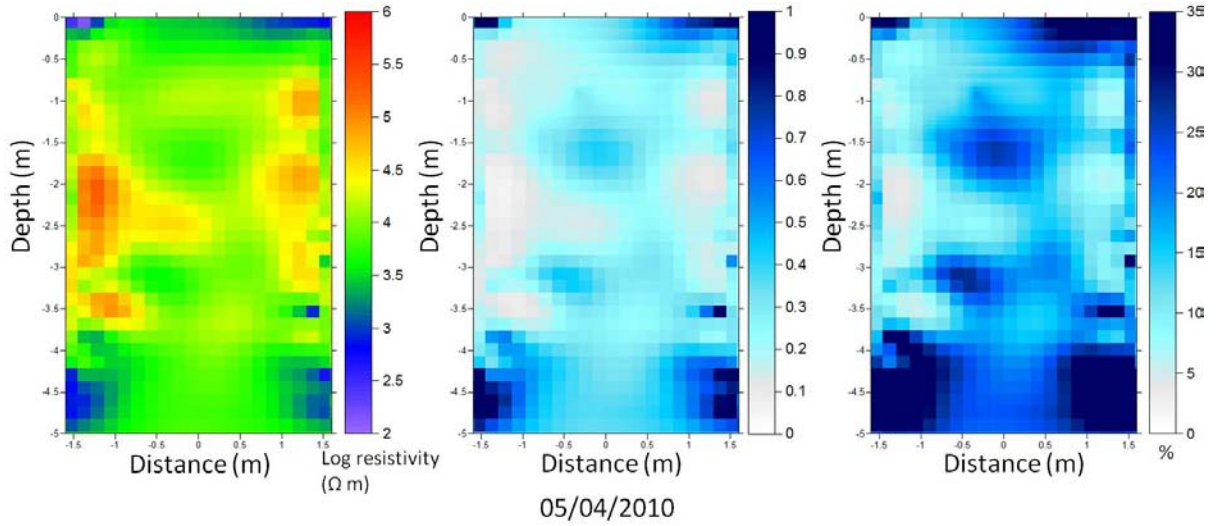
### Appendix III

Figures from south wall where column a) is temperature corrected individual ERT inversions b) estimated saturation and c) is water content

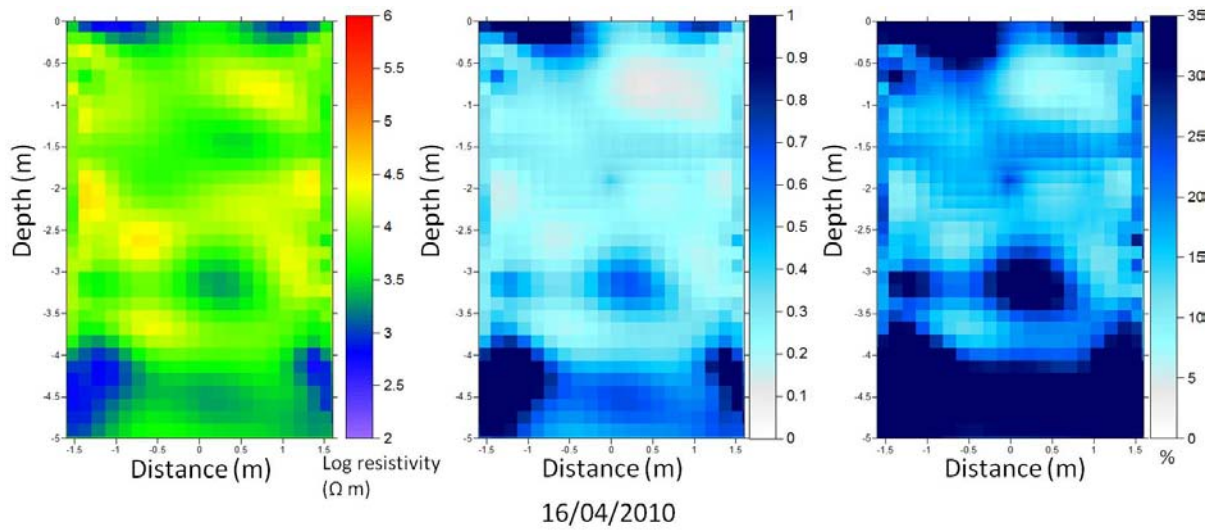
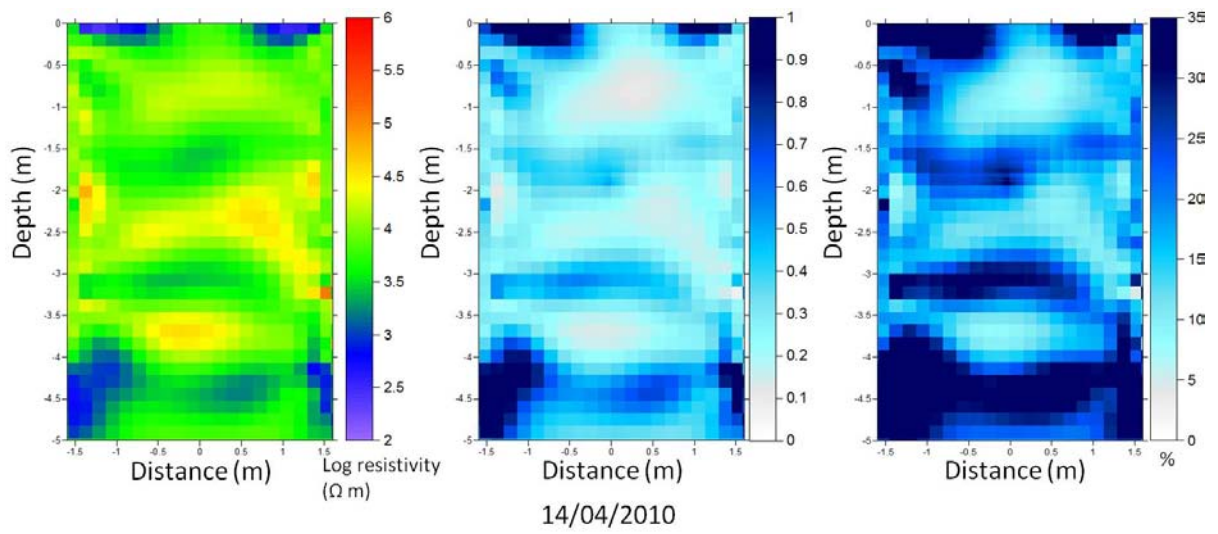
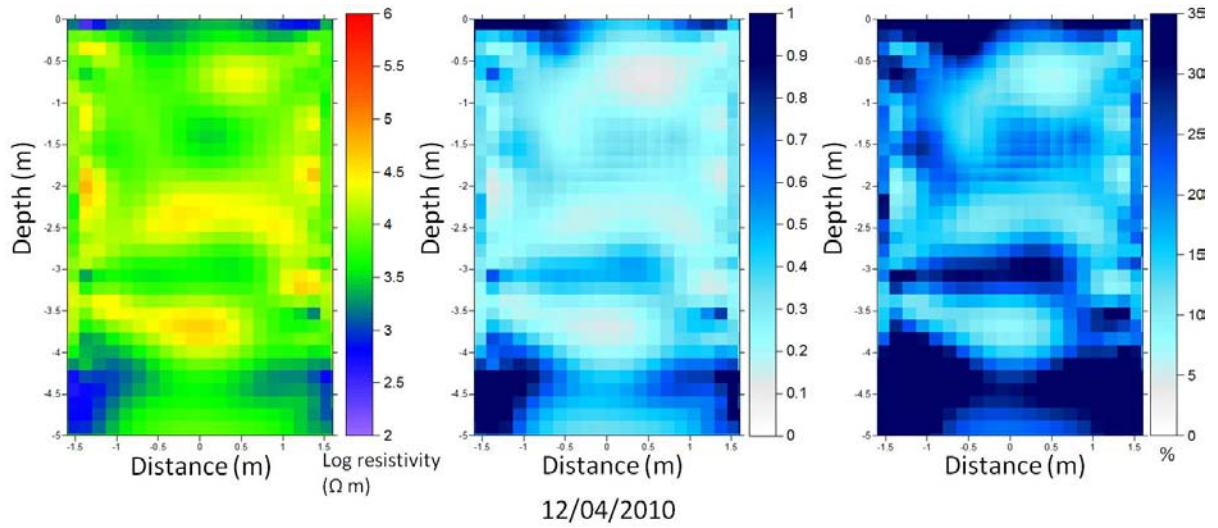


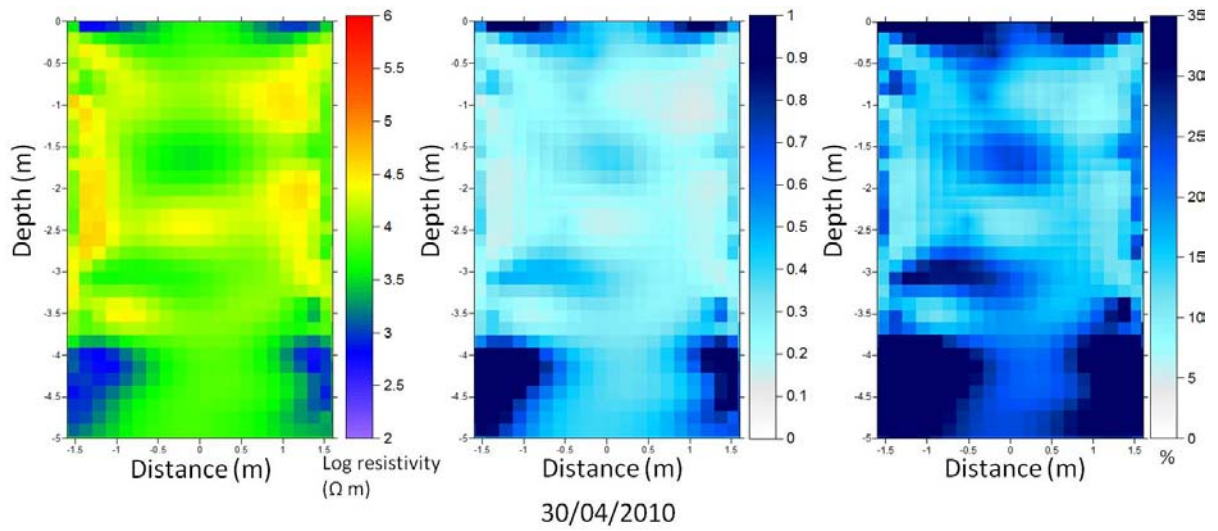
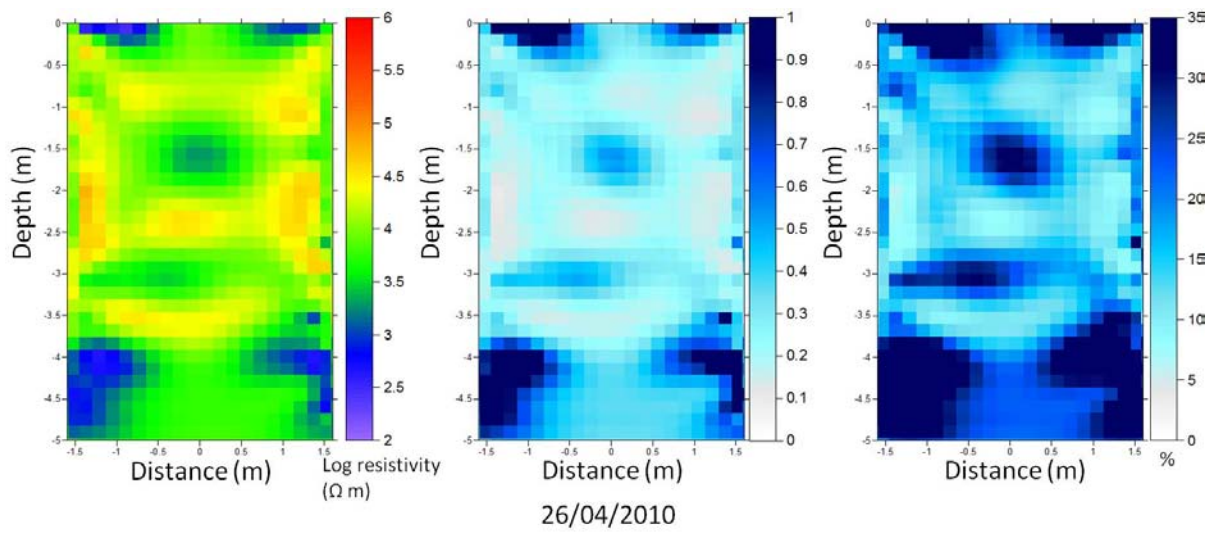
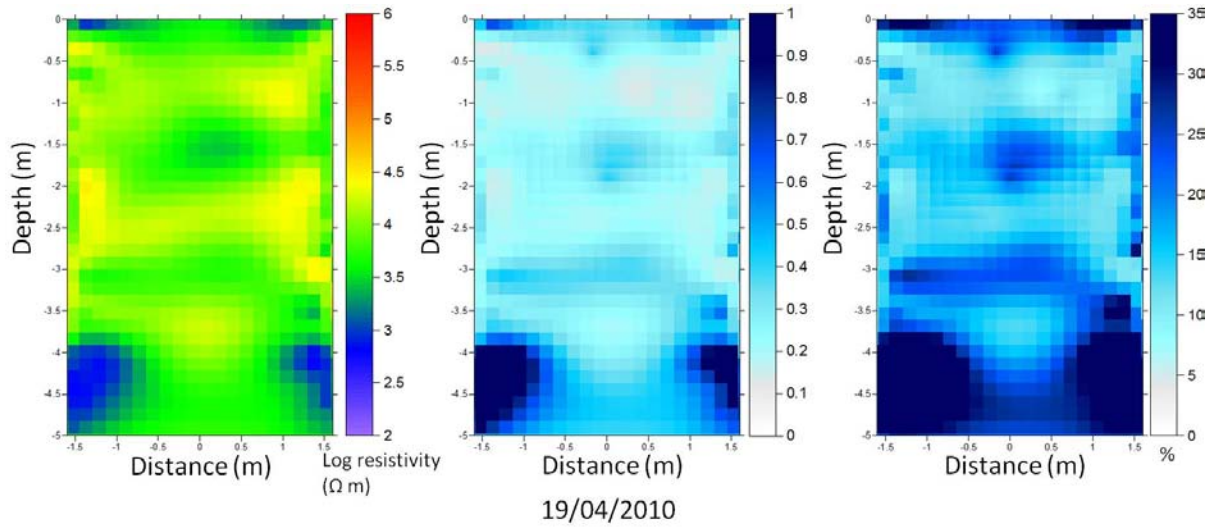




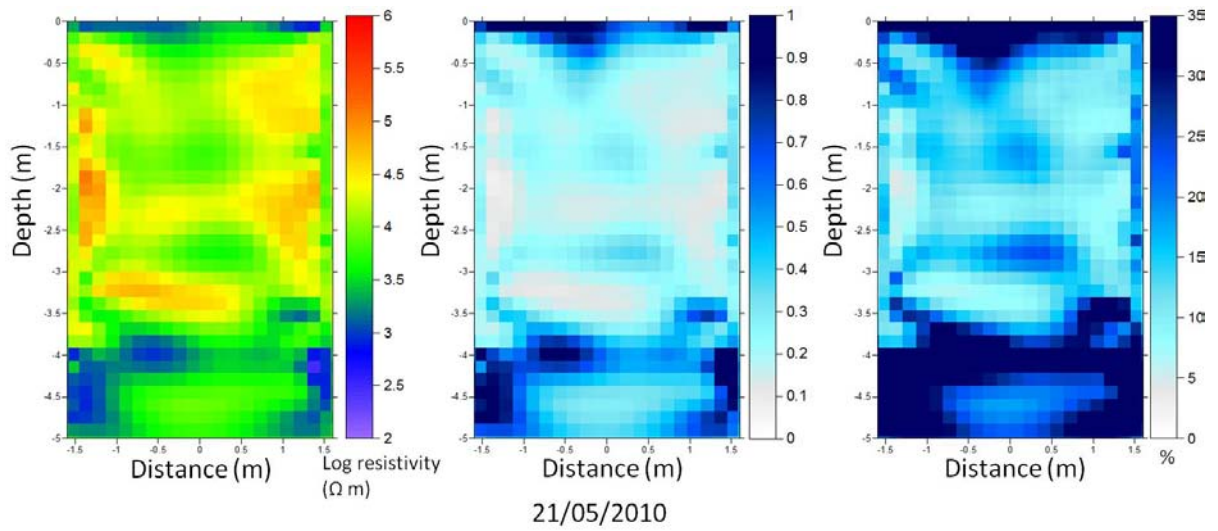
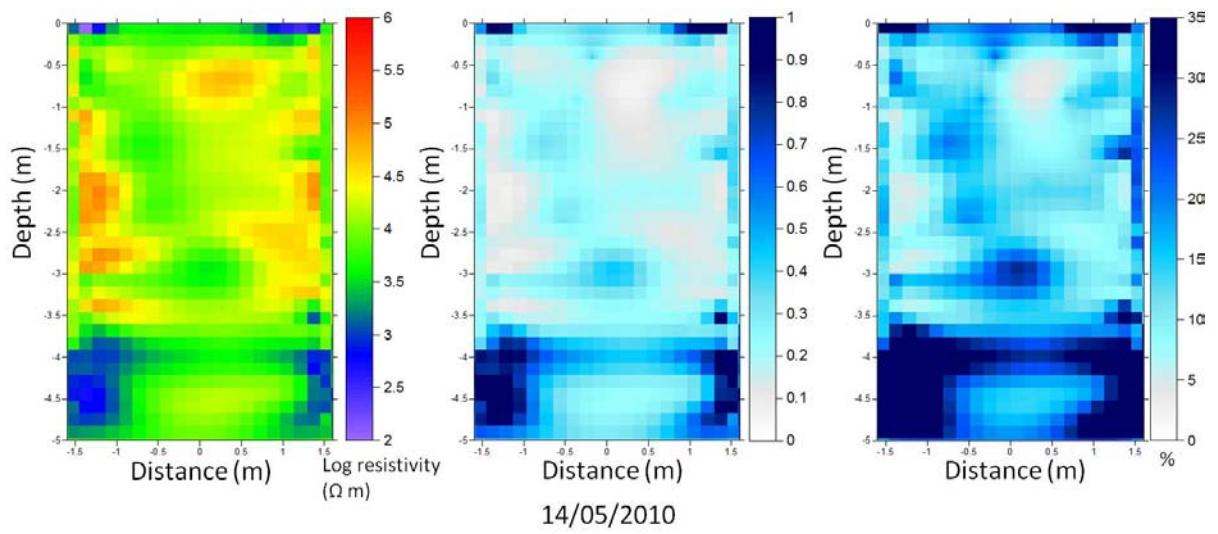
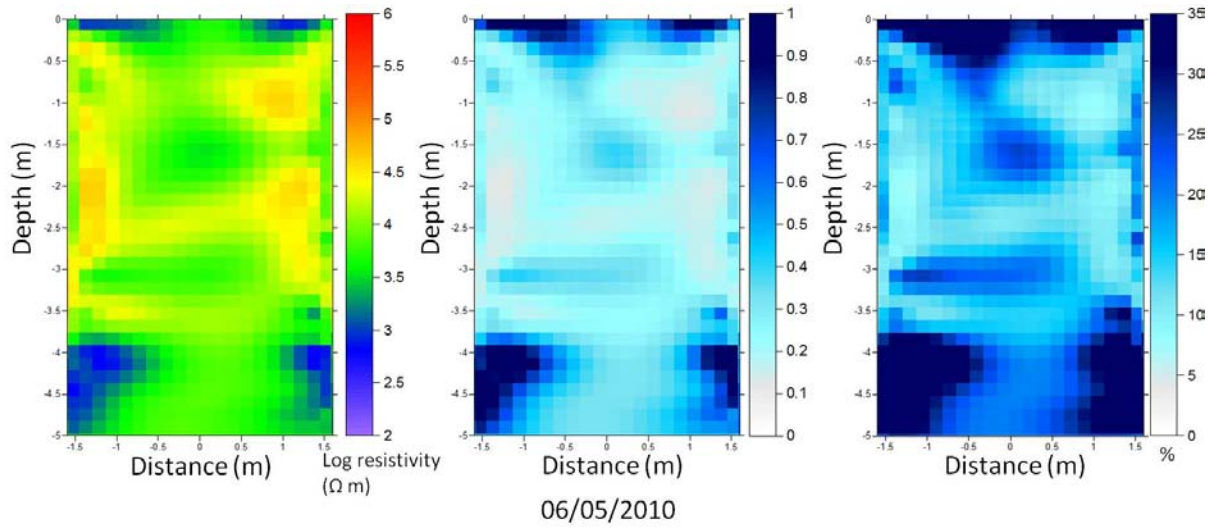












## Appendix IV

Figures of temperature corrected individual ERT inversion of north wall

